DESIGN, MODELING AND NUMERICAL ANALYSIS OF MICROWAVE AND OPTICAL DEVICES: THE MULTI-BAND PATCH ANTENNA, ULTRA WIDEBAND RING FILTER AND PLASMONIC WAVEGUIDE COUPLER

A Dissertation

by

YA-CHI LIU

Submitted to the Office of Graduate and Professional Studies of
Texas A&M University
in partial fulfillment of the requirements for the degree of

DOCTOR OF PHILOSOPHY

Chair of Committee,	Kai Chang
Committee Members,	Chin B. Su
	Laszlo Kish
	M. Suhail Zubairy
Head of Department,	Chanan Singh

December 2013

Major Subject: Electrical Engineering

ABSTRACT

In this dissertation, three devices are studied and devised for the applications in microwave and optical communication: (1) Multiband Patch Antenna, (2) Ultra-Wideband Band Pass Ring Filter and (3) Plasmonic Waveguide Coupler with High Coupling Efficiency.

First, the idea of a simple frequency reconfigurable patch antenna that operates at multiband from 2 GHz to 4.5 GHz is presented; by changing the position of the microstrip connecting elements on the antenna patches, the operating frequency will shift with fixed radiation patterns, which can be utilized in MIMO (Multiple IN Multiple Out) wireless data transmission.

Next, a compact ultra-wideband (UWB) single-ring bandpass filter of 8GHz bandwidth with sideband and harmonics suppression achieved by forced boundary condition and step impedance filter is proposed. This approach provides a simple way for the design of ultra-wideband filters. Based on the transmission spectrum, it is known that the group delay variation in the pass-band is smaller than 0.3 ns, which indicates the proposed structure is very suitable for real applications.

Finally, a short partially corrugated tapered waveguide for silicon-based micro-slab waveguide to plasmonic nano-gap waveguide mode conversion at the optical communication frequency is investigated. The structure is designed to achieve mode matching between the silicon slabs and plasmonic waveguides. High coupling

efficiencies up to 87%~98% are demonstrated numerically. The results show that the corrugated structure will be helpful for realizing full on-chip silicon plasmonic devices.

DEDICATION

This dissertation is dedicated to my family as well as my friends who encouraged and supported me during my Ph. D. program.

ACKNOWLEDGEMENTS

I am in debt to many people who supported and encouraged me during my study in the United States. First of all, I would like to express my gratitude to NSC, Taiwan for the support of my Ph.D. program; without the NSC scholarship, it would never be possible for me to study here. Next, I would like to thank my advisor Professor Kai Chang for providing me extreme freedom to explore the research topics I am interested in. His guiding style makes me a highly independent researcher. I also would like to convey my deepest gratitude to my former advisor, Professor Yinchieh Lai for his constant suggestions and encouragement. Additionally, I have to appreciate the kindness of Prof. Shih, Mr. John Fwu, Mr. Eddie Yu, Mr. Gray and Mr. Thompson for providing me the resource to overcome my research difficulties; I would not have interesting outcomes without their assistance. Finally, I want to thank Professor Su, Professor Kish and Professor Zubairy for serving as my committee members.

TABLE OF CONTENTS

Page

LIST OF FIGURES

Page

LIST OF TABLES

Page

CHAPTER I

INTRODUCTION

Wide band transmission has long been the goal pursued by engineering societies for the growing demand of high speed transmission of high volume of video and music data etc.. Therefore, there are many researches working on this issue to design devices or systems that can operate at a wide frequency range such as wide band antennas, filters for wireless communication or broad band switches for optical communication.

In view of this big picture, in this dissertation, microwave and optical devices for broad band applications are studied. For microwave devices, patch antenna with frequency reconfigurable functionality and ultra wide band ring band pass filters are designed. On the other hand, for optical devices, recent hot topics about plasmonic waveguides that allow guiding waves with the device size much smaller than the signal wavelength are discussed; coupler for plasmonic waveguide feeding is designed with high coupling efficiency. The organization of this dissertation is listed as follows:

Chapter II introduces the fundamental of the patch antenna first and then describes the designed detail, simulation and measurement results for the frequency changeable operation.

Chapter III explains the idea of force boundary condition for the design of ultra wide band single ring band pass filter; the designed filter and measurement results are demonstrated at the end of it.

Chapter IV gives the reviews of FDTD (Finite Difference Time Domain) method and it's algorithm for the simulation of wave propagation in dispersive media.

Chapter V is the photonic part that outlines the background of surface plasmon polaritons and the surface wave propagation at metal-dielectric interface enabling the decrease of device size; in the end, the difficulty of photonic-plasmonic mode coupling is point out and a new coupler is design to improve the coupling efficiency. Finally, some details of current undergoing researches are not included in this dissertation. These works will be depicted in future publications when the final piece is completed.

CHAPTER II

MULTI-BAND FREQUENCY RECONFIGURABLE PATCH ANTENNA*

Introduction

Recently, reconfigurable antenna has gained a lot of attention in the antenna design for multi-function-oriented wireless communication applications such as Software Defined Radio (SDR), Multiple-in-Multiple-out (MIMO) and RFID tag etc.. Frequency reconfigurability is one of the reconfigurable functions (polarization, radiation pattern, and operation band) in the reconfigurable antenna design. At present, some frequency reconfigurable antennas have been discussed in earlier literatures [1]-[3]. In this chapter, the fundamental knowledge of microstrip antennas is introduced and then the design, simulation and measurement of a simple multi-band frequency reconfigurable antenna with microstrip connecting elements is discussed. The designed antenna can operate at multi-band from 2 GHz to 4.5 GHz and the operating frequency can be shifted with fixed radiation patterns when the position of connecting element on antenna gaps is changed.

Microstrip Antenna Fundamentals

Microstrip antennas have received much attention in recent years, despite of some weakness, because of their many unique and attractive properties- low profile, light weight, compact structure, easy fabrication and flexible integration with solid-state devices. For above reasons, we study it for future application needs. There are usually two theoretical models used for the analysis and design of microstrip antennas; one is transmission line model (TLM) and the other is cavity model. Transmission line model is imposed for easy physical impedance analysis based on circuit theory, and cavity model is usually used for model analysis and also to attain the resonant frequency and field pattern. The most efficient way is to apply hybrid TLM-Cavity model for convenient analysis. In this chapter, hybrid TLM-Cavity model will be imposed in the antenna design.

Feed Lines

There are several different types of feed lines for microstrip antennas, namely aperture coupling, proximity coupling, coaxial probe, and microstrip line. Aperture coupling and proximity coupling are derivatives of the microstrip line and used to reduce the presence of high order transverse magnetic (TM) and transverse electric (TE) modes. The primary difference between the couplings is in how the dielectric surrounding the line is treated. The TM and TE modes cause cross polarization, a radiation pattern orthogonal to the intended polarized pattern. The coaxial probe is connected directly to

the antenna, which makes impedance matching more challenging. The microstrip line is etched on the same substrate and easily matched to the antenna. The choice of the feed line is based on the intended application of the antenna. Coaxial probe is adopted for the reconfigurable antenna design discussed in this chapter for simplicity and measurement convenience.

Substrate

Microstrip technology behaves differently based on the substrate dielectric and height [4]. Substrate used in antenna design have a range of dielectric constants between $2.2 <= \varepsilon_r <= 12$ and heights are usually between $0.003\ \lambda_o <= h <= 0.005\ \lambda_o$. Choice of the correct substrate is crucial since the microstrip feed line and antenna are etched on the same substrate. Thick substrates with a low dielectric allow for increased antenna efficiency, bandwidth, physical size, and loosely bound radiated fields. Thin substrates with high dielectrics allow for tight radiated fields reducing unintended radiation and coupling, small bandwidths, reduction in size, and less efficiency. The latter are used primarily with microwave circuitry.

The substrate chosen must minimize field fringing from the microstrip feed line. Field fringing causes the resonant frequency to shift, changing the operational frequency bandwidth. The RT/Durioid 5880 meets this requirement. The substrate chosen has a thickness of 0.317 cm and low dielectric constant of $\varepsilon_r = 2.20 +/- 0.02$. Table 2-1 lists

the parameters for the substrate. The figure of the feed line and antenna, detailing the geometry and dimensions, are shown in Figure 2-1 and Figure 2-2.

Table 2-1. Parameters for patch antenna substrate.

Rogers corporation RT/Duroid 5880
Dielectric 2.2 +/- 0.02
Loss tangent 0.0009
Clad foil thickness (t) 0.034 mm
Thickness (height) 3.175 mm

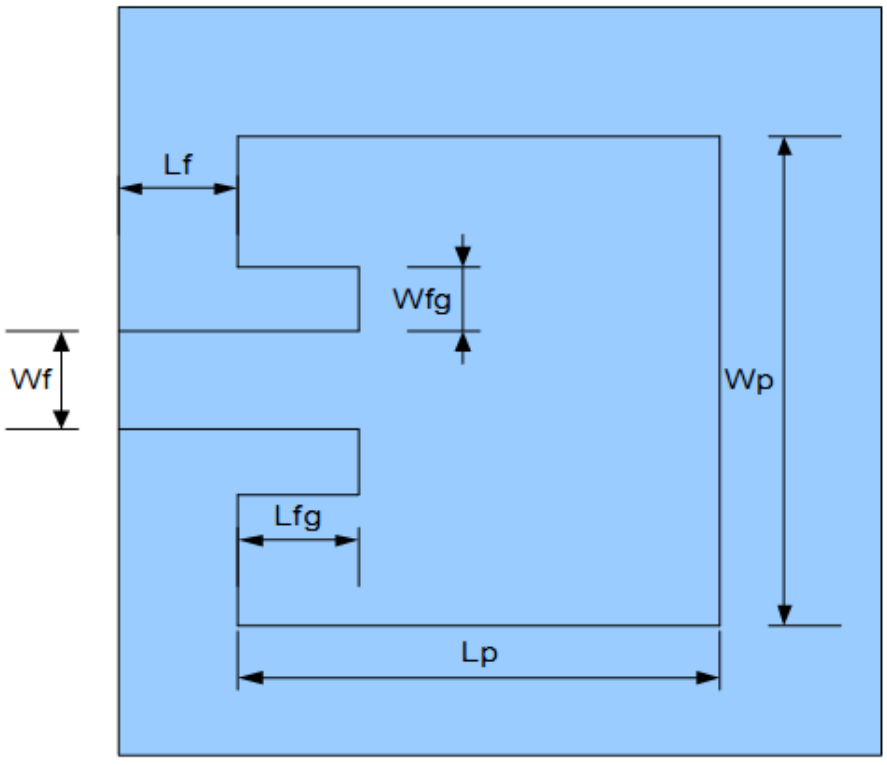

Figure 2-1. Dimensions for the feed line and patch antenna.

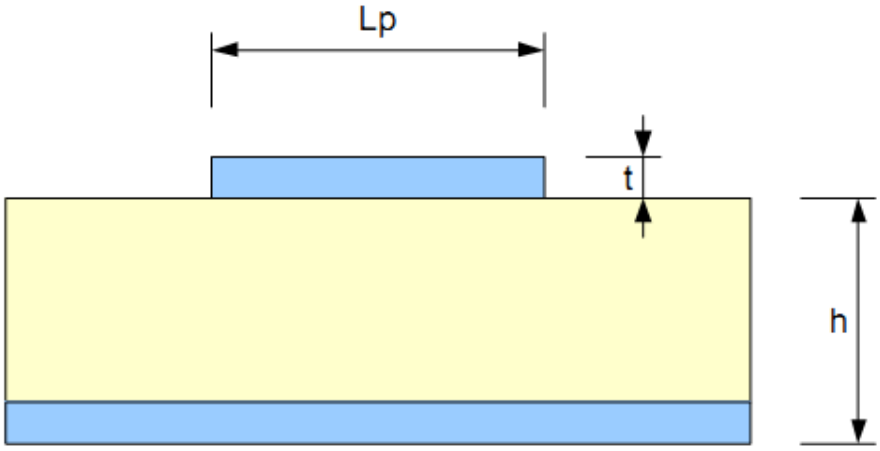

Figure 2-2. Side view of the strip line.

Feed Line Design

Microstrip lines have several favorable qualities: low cost, small size and simple production. The design of a microstrip line is straightforward and the only values computed are width, height, dielectric and characteristic impedance. A microstrip line has deterministic characteristic impedances, a reason it is used in transmission of microwave frequencies where conventional wiring and lumped circuit components are undesirable. The characteristic impedance of the feed line (FL), for this application needs to be 50 ohms to reduce standing waves, the possibility of arcing, and for maximum power transferred to the antenna. The width [5], W_f, of the microstrip line controls the characteristic impedance and is calculated by Equation (2-1).

$$for\ \frac{w_f}{h} < 2$$

$$\frac{w_f}{h} = \frac{8e^A}{e^{2A}}$$

$$for\ \frac{w_f}{h} > 2$$

$$\frac{w_f}{h} = \frac{2}{\pi}\left[B - 1 - ln(2B-1) + \frac{\epsilon_r - 1}{2\epsilon_r}\left[ln(B-1) + 0.39 - \frac{0.61}{\epsilon_r}\right]\right]$$

$$A = \frac{Z_O}{60}\sqrt{\frac{\epsilon_r + 1}{2}} + \frac{\epsilon_r - 1}{\epsilon_r + 1}(0.23 + \frac{0.11}{\epsilon_r})$$

$$B = \frac{377\pi}{2Z_O\sqrt{\epsilon_r}} \quad (2\text{-}1)$$

The estimated width of the feed line was calculated to be 0.978273 cm with a characteristic impedance value of 50.28077 ohms. Equation (2-2) and Equation (2-3), used graphically and analytically [5], determined the width to be 0.986419 cm with a characteristic impedance of 50.00029 ohms as seen in Figure 2-3. This width provides an error accuracy of 10^{-3} ensuring good characteristic impedance. Graphing the impedance tells more about the line than the calculated solution does because in Figure 2-3, as the width of the line increases, the impedance drops exponentially. In this case, the length of the microstrip line was specified to be 4cm. The design parameters for the feed line are gathered in Table 2-2.

$$Z_O = \frac{120\pi}{\sqrt{\epsilon_{eff}}(\frac{w_f}{h} + 1.393 + 0.677ln(1.444 + \frac{w_f}{h}))}\ for\ \frac{w_f}{h} > 1 \quad (2\text{-}2)$$

$$\epsilon_{eff} = \frac{\epsilon_r + 1}{2} + \frac{\epsilon_r - 1}{2}[1 + 12\frac{h}{w_f}]^{-1/2} \quad for\ \frac{w_f}{h} > 1 \quad (2\text{-}3)$$

Table 2-2. Feed line parameters

Height	0.317 cm
Width(W_f)	0.986 cm
Length(L_f)	4.0 cm
Z_o	50 Ohms

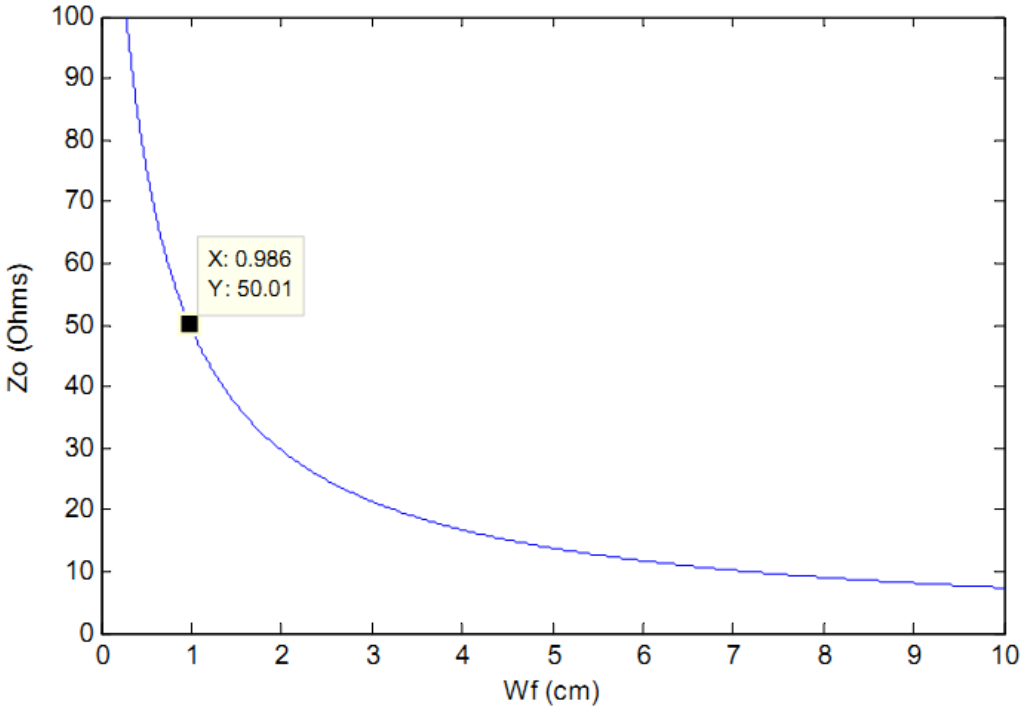

Figure 2-3. Characteristic impedance of the feed line.

Patch Antenna Design

The microstrip antenna can be designed and built to fit many geometric shapes for the intended application. The rectangular or square geometry is very common and has a unique name, "patch". Important variable qualities of a patch include resonant frequency, patch width, patch length, feeding position, substrate height and substrate index.

A rectangular patch antenna resonates at the operating mode influences the resonant frequency. The resonant frequency is located where the imaginary part of the antenna impedance is zero and allows maximum radiated power. The mode with the lowest resonant frequency is called the dominant mode. The dominant mode for the model is the $TM_{mnp}^{z} = TM_{010}^{z}$. This application of a patch antenna is designed between 2-4GHz and with the resonate frequency at 3GHz. The length, L, as shown in Figure 2-4, of the patch controls the resonant frequency. The length of the patch is chosen to be $L \sim= \lambda_{eff}/2$. The design of the patch requires selection of the dielectric constant, resonant frequency, and substrate height. This allows the design to be completed with following steps:

1. Calculate the width by from Equation (2-4) for efficient radiation from the antenna.
2. Determine the effective dielectric constant, ε_{eff}, which accounts for field fringing.
3. Calculate the length extension, ΔL, required to remove the complex impedance of the patch and accounts for the patch being electrically longer due to the field fringing.
4. Calculate the physical length of the patch based on step 1 to step 3.

5. Using transmission line model to get the feeding position y_o to match the 50Ω impedance of feeding probe or strip line.

Figure 2-4 shows the schematic diagram of the patch antenna and Table 2-3 lists the values of the design parameters in our designed case based on following equations.

$$w_p = \frac{1}{2f_r\sqrt{\mu_0\epsilon_0}}\sqrt{\frac{2}{\epsilon_r+1}} \tag{2-4}$$

$$\frac{\Delta L}{h} = 0.412\frac{(\epsilon_{eff}+0.3)(\frac{w_p}{h}+0.264)}{(\epsilon_{eff}-0.258)(\frac{w_p}{h}+0.8)} \tag{2-5}$$

$$L = \frac{1}{2f_r\sqrt{\mu_0\epsilon_0}\sqrt{\epsilon_{eff}}} - 2\Delta L \tag{2-6}$$

$$L_{eff} = L + 2\Delta L \tag{2-7}$$

$$(f_r)_{mnp} = \frac{1}{2\pi\sqrt{\mu\epsilon}}\sqrt{\left(\frac{m_\pi}{h}\right)^2 + \left(\frac{n_\pi}{L_p}\right)^2 + \left(\frac{p_\pi}{w_p}\right)^2} \tag{2-8}$$

$$(f_r)_{010} = \frac{1}{2\pi L_p\sqrt{\mu\epsilon}} \tag{2-9}$$

$$(f_r)_{010} = \frac{1}{2\pi L_{eff}\sqrt{\mu\epsilon}} \tag{2-10}$$

$$G_{11} = \frac{w_p}{120\lambda_o}\left[1 - \frac{1}{24}(k_o h)^2\right] \; for \; \frac{h}{\lambda_o} < \frac{1}{10} \tag{2-11}$$

$$G_{11} = \frac{\int_0^\pi [\frac{sin\frac{k_0 w_p}{2}cos(\theta))}{cos(\theta)}]^2 \, sin(\theta)^3 d\theta}{120\pi^2}$$

$$G_{12} = \frac{\int_0^\pi [\frac{sin\frac{k_0 w_p}{2}cos(\theta))}{cos(\theta)}]^2 \, sin(\theta)^3 J_o(k_o \, L \, sin\theta) d\theta}{120\pi^2} \tag{2-12}$$

$$B_1 = \frac{w_p}{120\lambda_o}[1 - 0.636(k_O h)] \; for \; \frac{h}{\lambda_o} < \frac{1}{10} \tag{2-13}$$

$$Z = \frac{1}{(G11+G12)+jB1} \tag{2-14}$$

Table 2-3. Values of the design parameters.

Patch Width W_p	5 cm
Dielectric index	1
Length extension ΔL	0.2590 cm
Patch Length L	4.4818 cm
Feed position y_o	1.263 cm
Substrate height h	0.373 cm
B_1	0.00801151
G_1	0.004 S

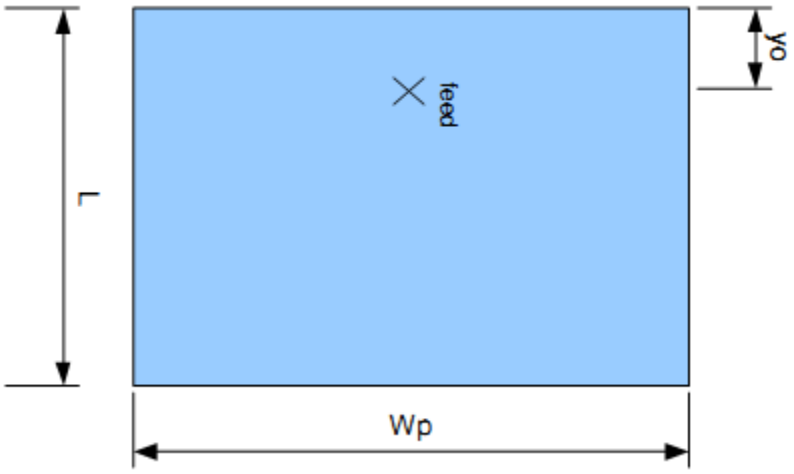

Figure 2-4. The schematic diagram of the patch antenna.

The Transmission Line Model

Transmission line model (TLM) treats rectangular patch antennas as a transmission line and the radiation slots as circuit elements ($G + j\ B$). This model provides us an easy way to decide the input impedance and feeding position of the patch. Figure 2-5 shows the transmission line model of our designed patch antenna. The input impedance is a function of feeding position y_o, as shown in Equation (2-15) and Figure 2-6. From Figure 2-6, it is known that when y_o is 1.263cm, the input impedance matches the 50Ω feed line.

$$R = \frac{1}{2(G11+G12)}(\cos(\pi\ y_0/4.4818))^2 \qquad (2\text{-}15)$$

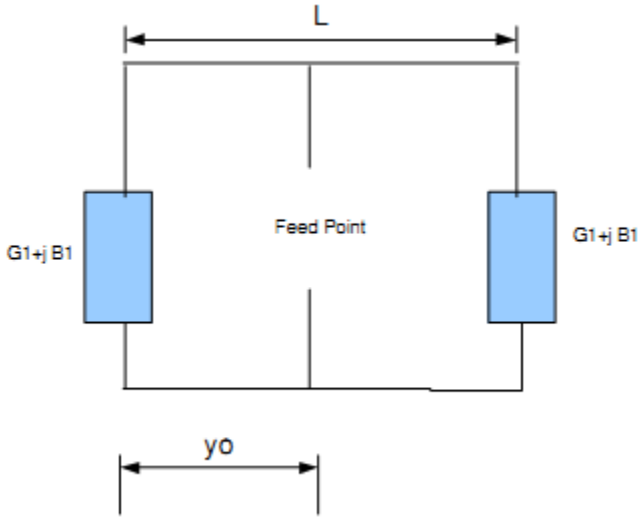

Figure 2-5. Transmission line model of the patch antenna shown in Figure 2-4.

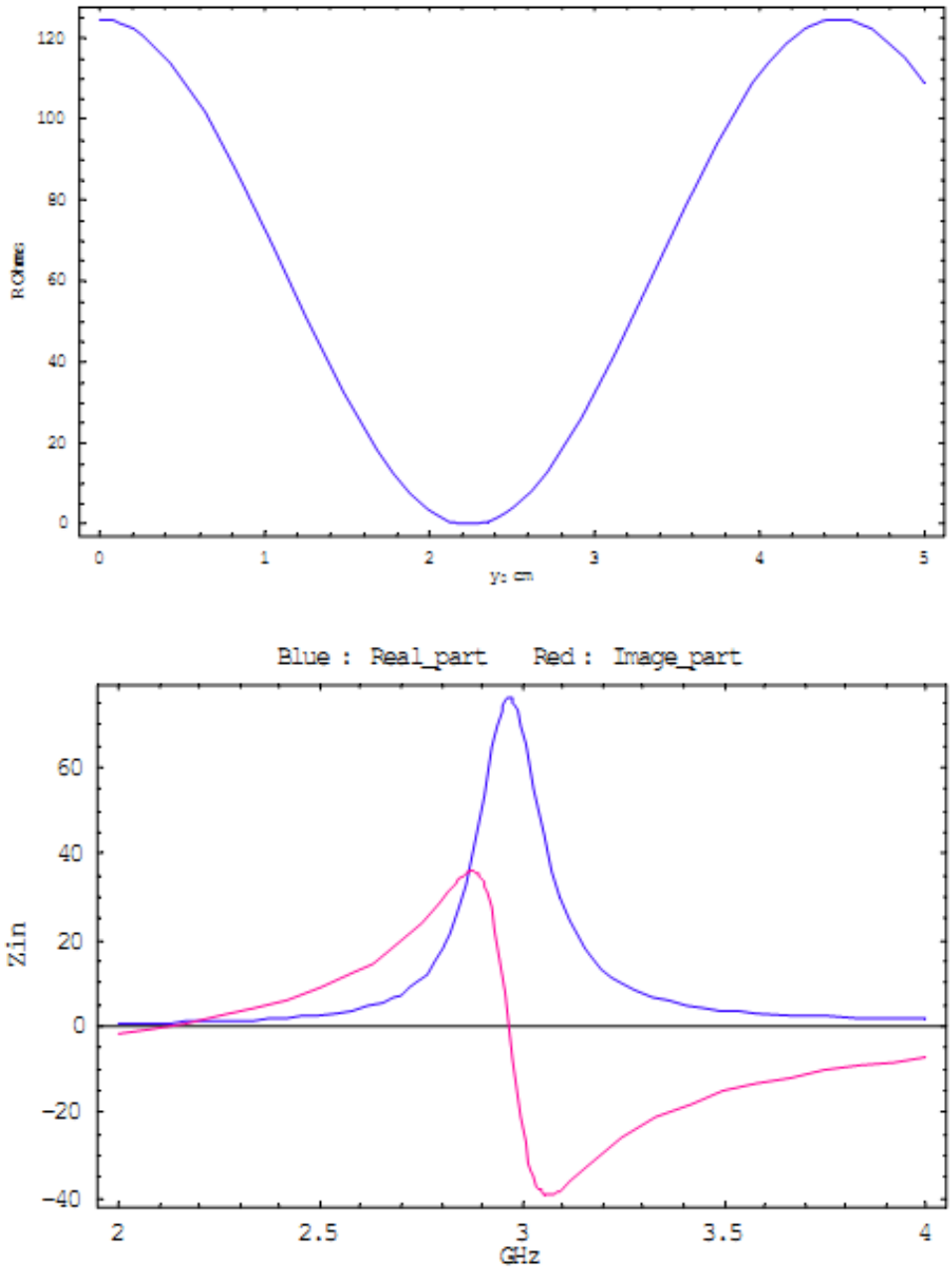

Figure 2-6. Input resistance as a function of y_o and Z_{in} as a function of frequency.

When all of the parameters of the desired patch antenna are fixed and calculated, HFSS was utilized to check the VSWR and radiation pattern (Figure 2-7, 2-8 and 2-10) of our design structure. Finally, the radiation patterns (Figure 2-9 and 2-11) are measured and compared with the simulated results. From figures we can see that the simulated results match the experimental ones well.

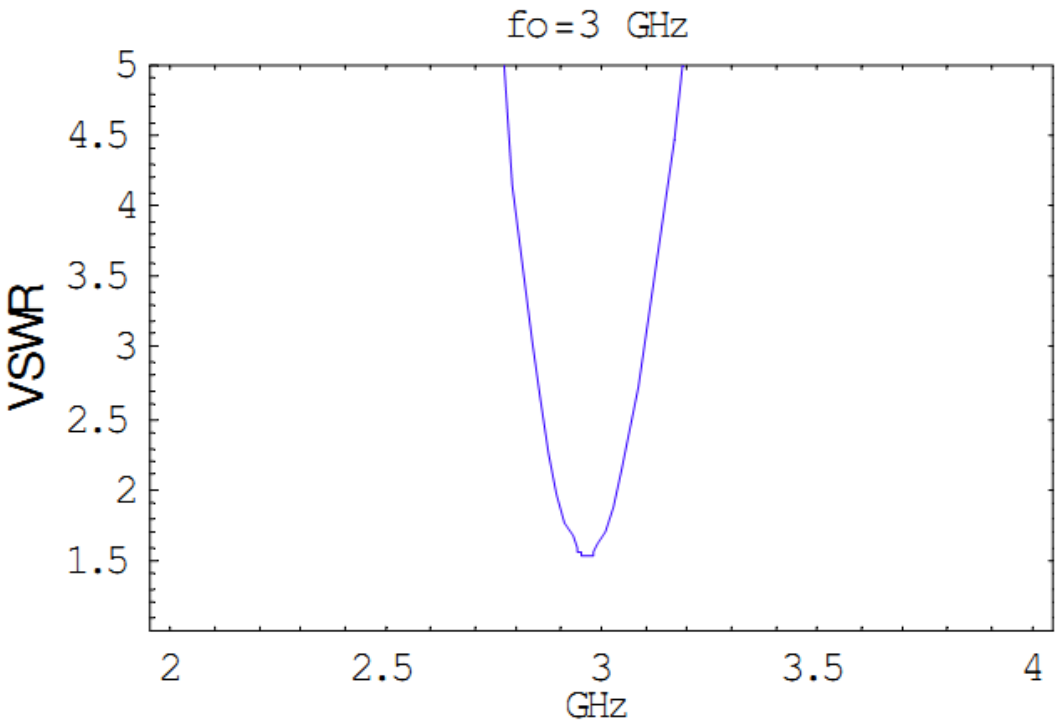

Figure 2-7. VSWR of the designed patch (HFSS).

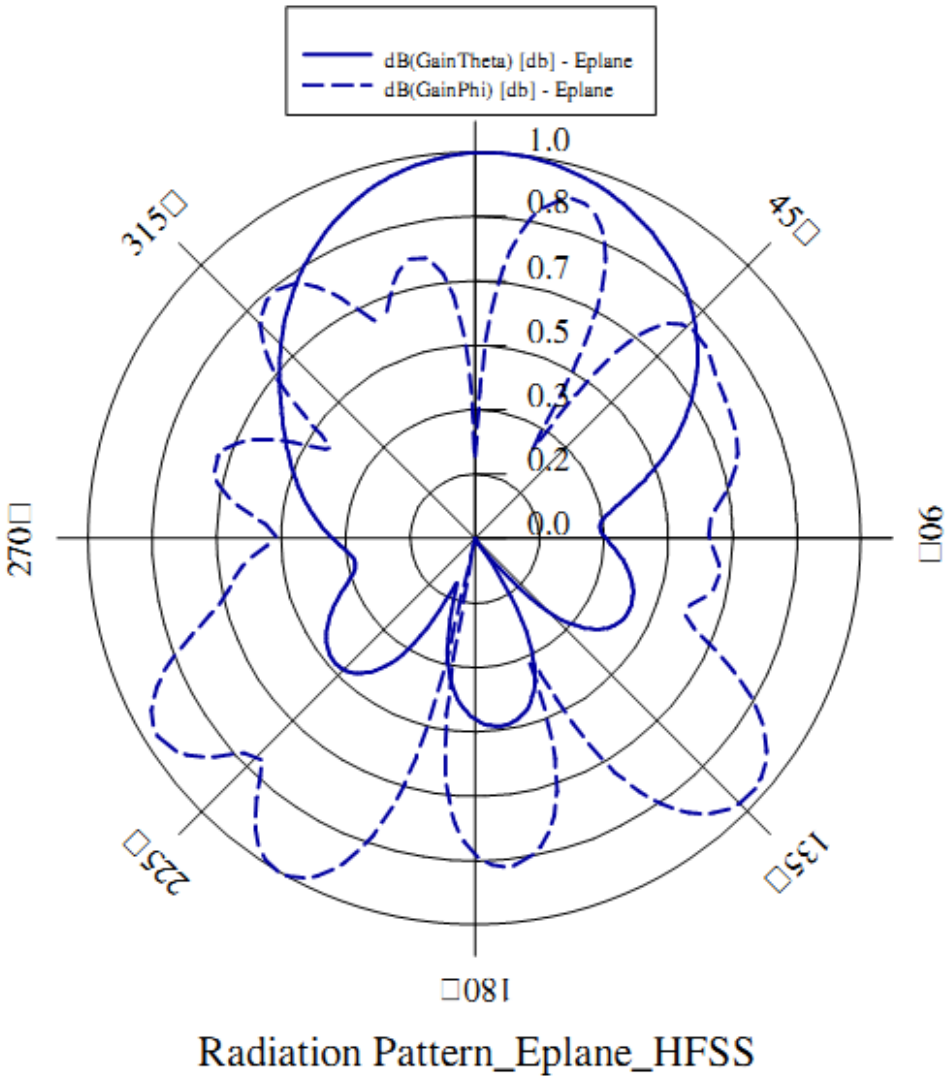

Figure 2-8. Radiation pattern for E plane (simulated).

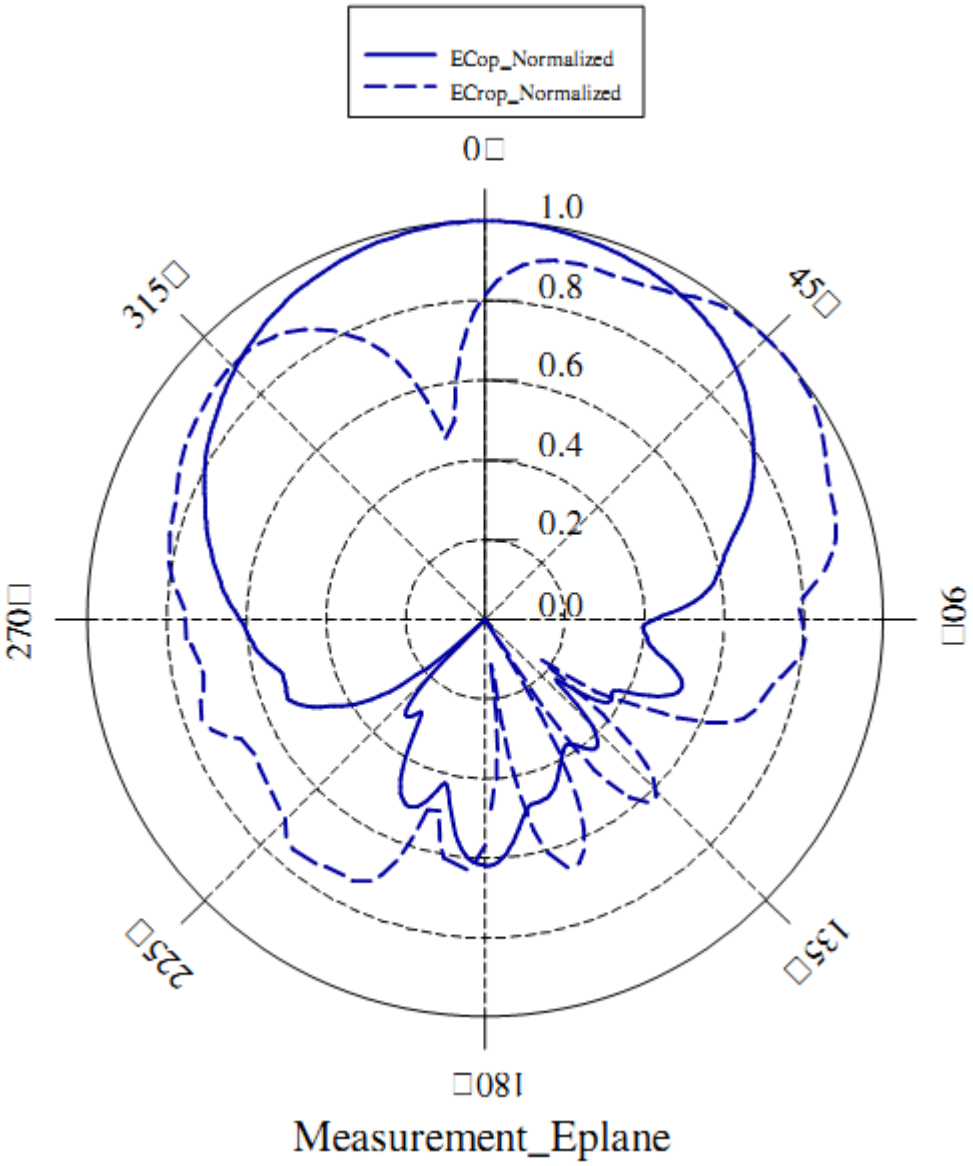

Figure 2-9. Radiation pattern for E plane (measured).

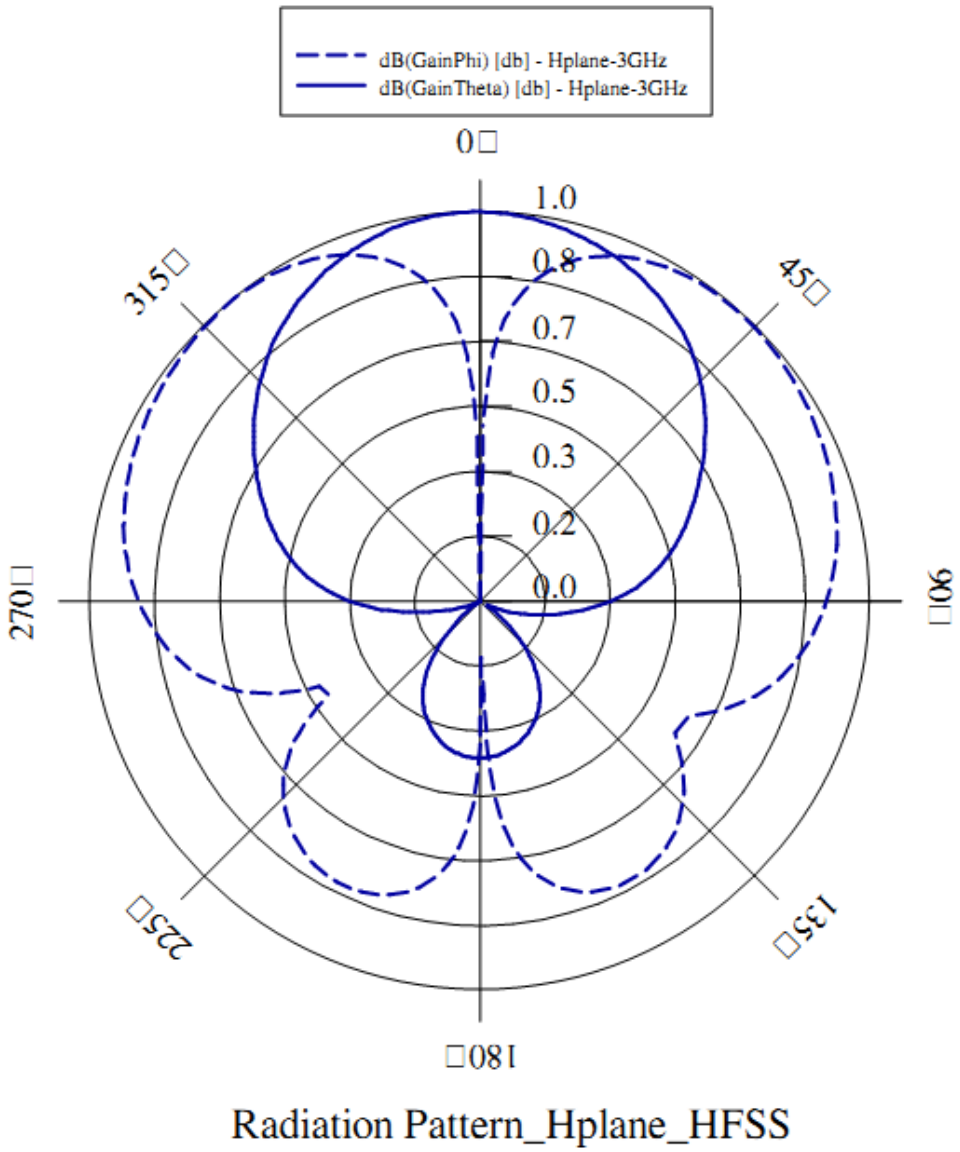

Figure 2-10. Radiation pattern for H plane (simulated).

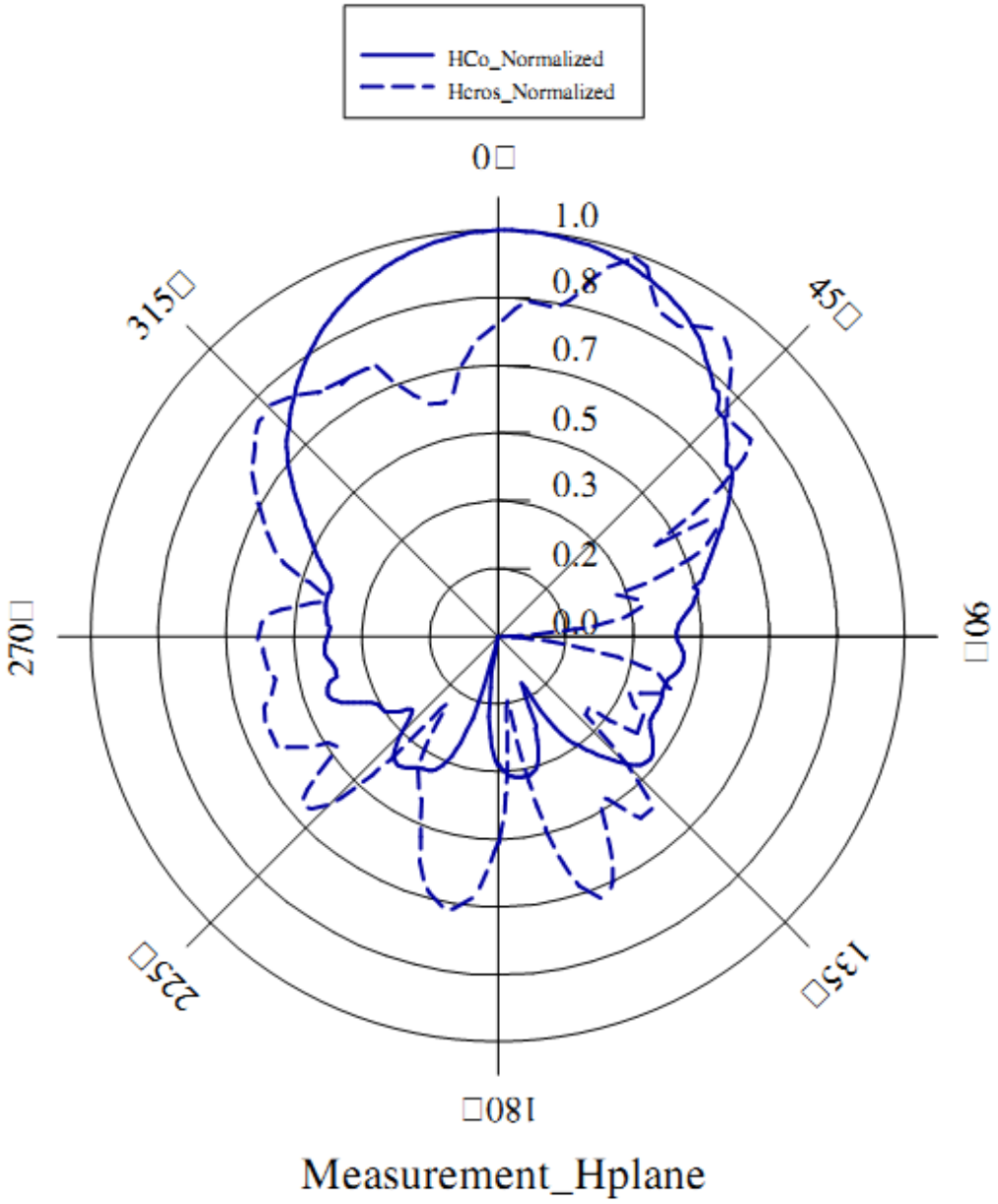

Figure 2-11. Radiation pattern for H plane (measured).

Reconfigurable Antennas

Reconfigurable antennas provide the flexibility to change its resonant frequency or radiation pattern when needed. In this section, the reconfigurable antenna with resonant frequency operating at 3GHz and 3.5GHz is demonstrated for the design idea. PIN diodes are used as switches between 3GHz and 3.5GHz modes. When a PIN diode is used, its equivalent impedance should be imported into the transmission line model for analysis. The structure of this antenna is shown in Figure 2-12. When the switch is on, the antenna operates at 3.5 GHz. On the contrary, the antenna operates at 3 GHz when the switch is off. We make the patch width fixed and the length of the antenna switchable with PIN diodes that vary the resonant frequency. Figure 2-13 shows the transmission line model of our reconfigurable antenna with ideal switches. Table 2-4 lists the parameters of this antenna based on the previously described procedure. To validate the design, HFSS is applied for the simulation. As shown in Figure 2-14, the simulated VSWR tells the resonant frequencies of the designed antenna are located at 3GHz and 3.5GHz, which meets the design requirement with the parameters defined in Table 2-4. On the other hand, the transmission line model (TLM) also validates the design that gives the zero imaginary part of the input impedance around 3.5 GHz depicted in Figure 2-15.

Table 2-4. The design parameters for the frequency reconfigurable antenna I.

Patch Width W_p	5 cm
Dielectric index	1
Substrate height	0.373 cm
L_1 (3.5 GHz)	3.76771 cm
y_{o1}	2.7884 cm
B_1	0.00887018
G_1	0.004688 S
L_2 (3 GHz)	4.4818 cm
y_{o2}	3.218 cm
B_2	0.00801151
G_2	0.004006 S

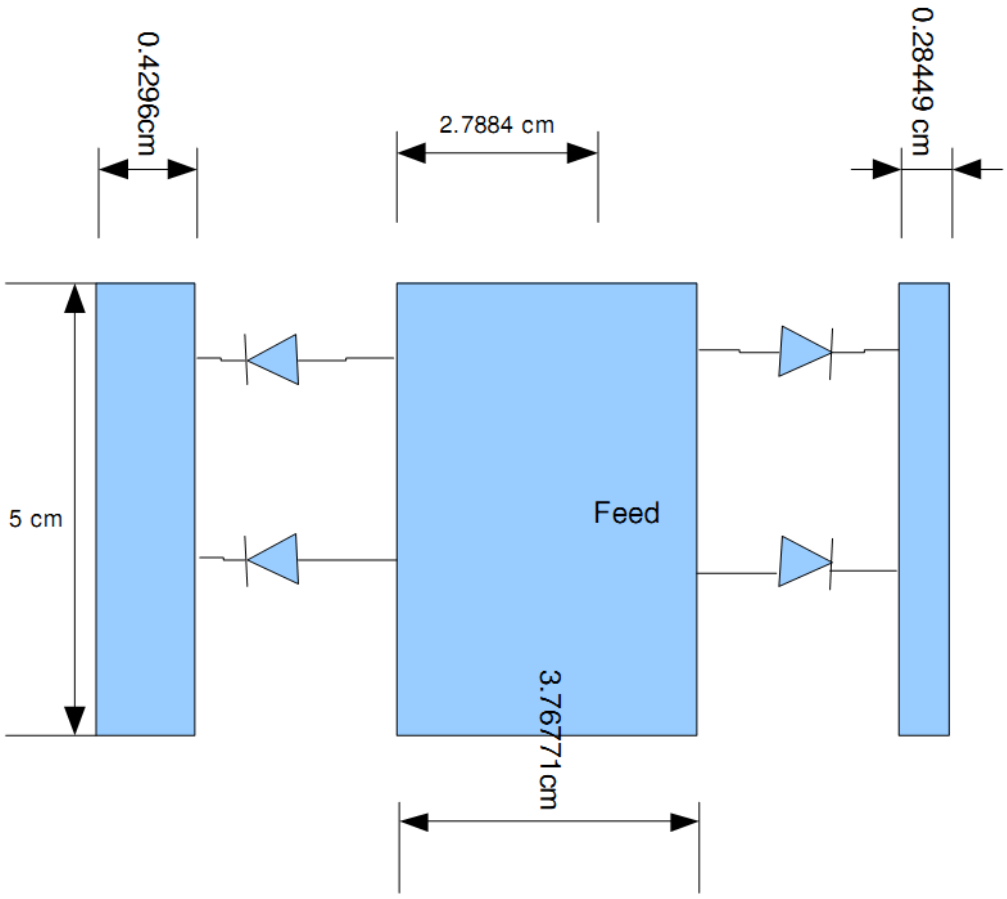

Figure 2-12. Schematic diagram of the frequency reconfigurable antenna.

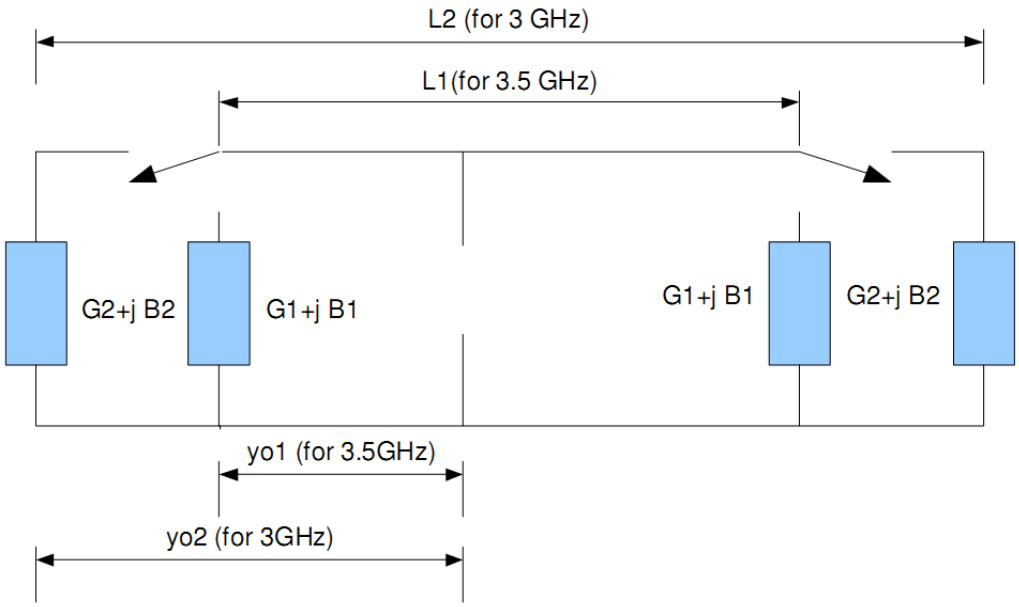

Figure 2-13. Transmission line model of the reconfigurable antenna shown in Figure 2-12.

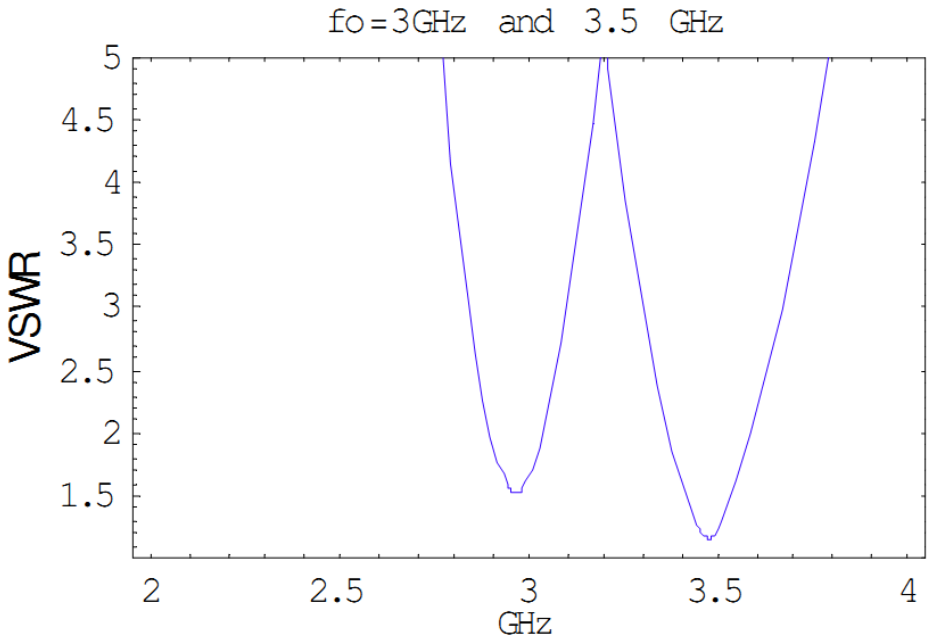

Figure 2-14. VSWR for the frequency reconfigurable antenna with ideal switch. When switch is on, the resonant frequency is 3 GHz; when the switch is off, the resonant frequency is 3.5 GHz.

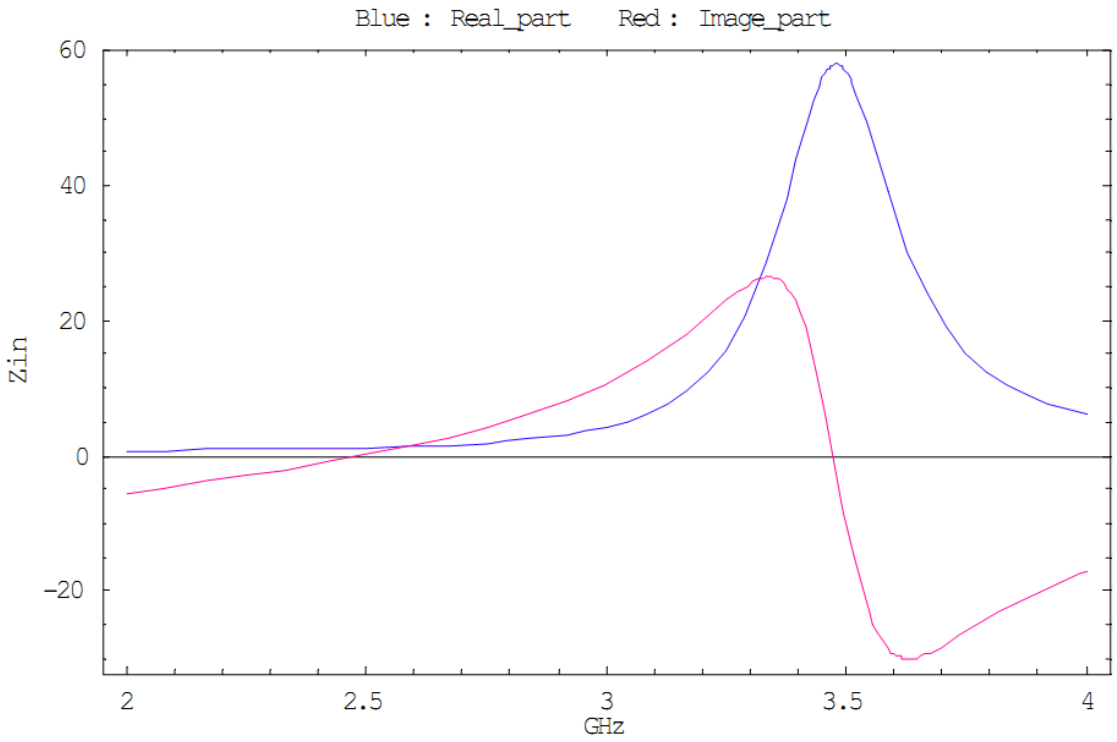

Figure 2-15. Input impedance v.s. frequency when the switch is on.

Multiband Frequency Reconfigurable Antenna

Recently, reconfigurable antenna has gained a lot of attention in the antenna design for multi-function-oriented wireless communication applications such as Software Defined Radio (SDR), Multiple-in-Multiple-out (MIMO) and RFID tag etc.. Frequency reconfigurability is one of the reconfigurable functions (polarization, radiation pattern, and operation band) in the reconfigurable antenna design. There are some frequency reconfigurable antennas have been discussed in earlier literatures [6]-[8] and in previous section, the frequency reconfigurable antenna is introduced. In this section, the design, simulation and measurement of a simple multiband frequency reconfigurable antenna with microstrip connecting elements is discussed. It is found that the antenna can operate at multiband from 2 GHz to 4.5 GHz and the operating frequency can be shifted with fixed radiation patterns when the position of connecting element on antenna gaps is changed.

The antenna structure and dimension parameters are shown in Figure 2-16 and Table 2-5, respectively. Two 0.5 mm gaps are placed between the inner driven element and outer parasitic element; four 0.5 mm x 0.5 mm microstrip connecting elements, which can be regarded as ideal switches, are placed on the gaps. Based on the transmission line model, the patch antenna is designed to operate at 3.5 GHz with patch length L_{pl} and 3 GHz with patch length L_{p2} before the gaps are placed. Rogers RT5880 Duroid ($\varepsilon_r = 2.2$) of 30 mil thickness is used here as the substrate. The four connecting elements are located on the gaps with different positions D for the measurement of S_{11} and radiation patterns.

Table 2-5. The design parameters for the frequency reconfigurable antenna II.

W_P	L_{P1}	L_{P2}	Y_P	G	D
39.52 mm	28.48 mm	31.9 mm	9.18 mm	0.5 mm	Varies

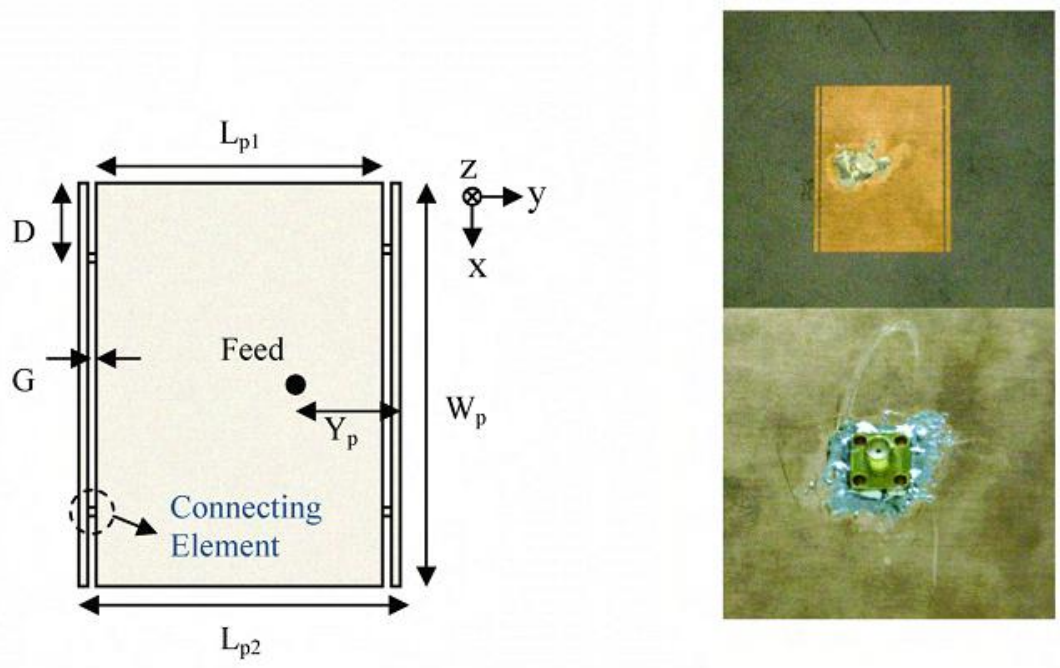

Figure 2-16. Left: The schematic of the antenna. Right: The top view and bottom view of the actual antenna appearance.

The S_{11} and radiation patterns with D = 0 mm and 5 mm are depicted in Figure 2-17 and Figure 2-18, respectively. Figure 2-17 (a) shows the antenna works around 3.3 GHz when there are no connecting elements on the gaps. When the connecting elements are placed, multiple resonant frequencies appear between 2 GHz and 4.5 GHz. In addition, when the position D shifts, the resonant frequencies also shift. According to Figure 2-17, the antenna can operate at frequencies which is lower than 3GHz (2.66 GHz) or higher than 3.5 GHz (4.08 GHz). The position D of the connecting element gives another degree of freedom to reconfigure the operating frequency of antenna other than the originally designed 3 GHz and 3.5 GHz. With this property the antenna can work in a wider frequency range. On the other hand, the radiation patterns of the antenna remain the same as D and the operating frequency are changed, as shown in Figure 2-18.

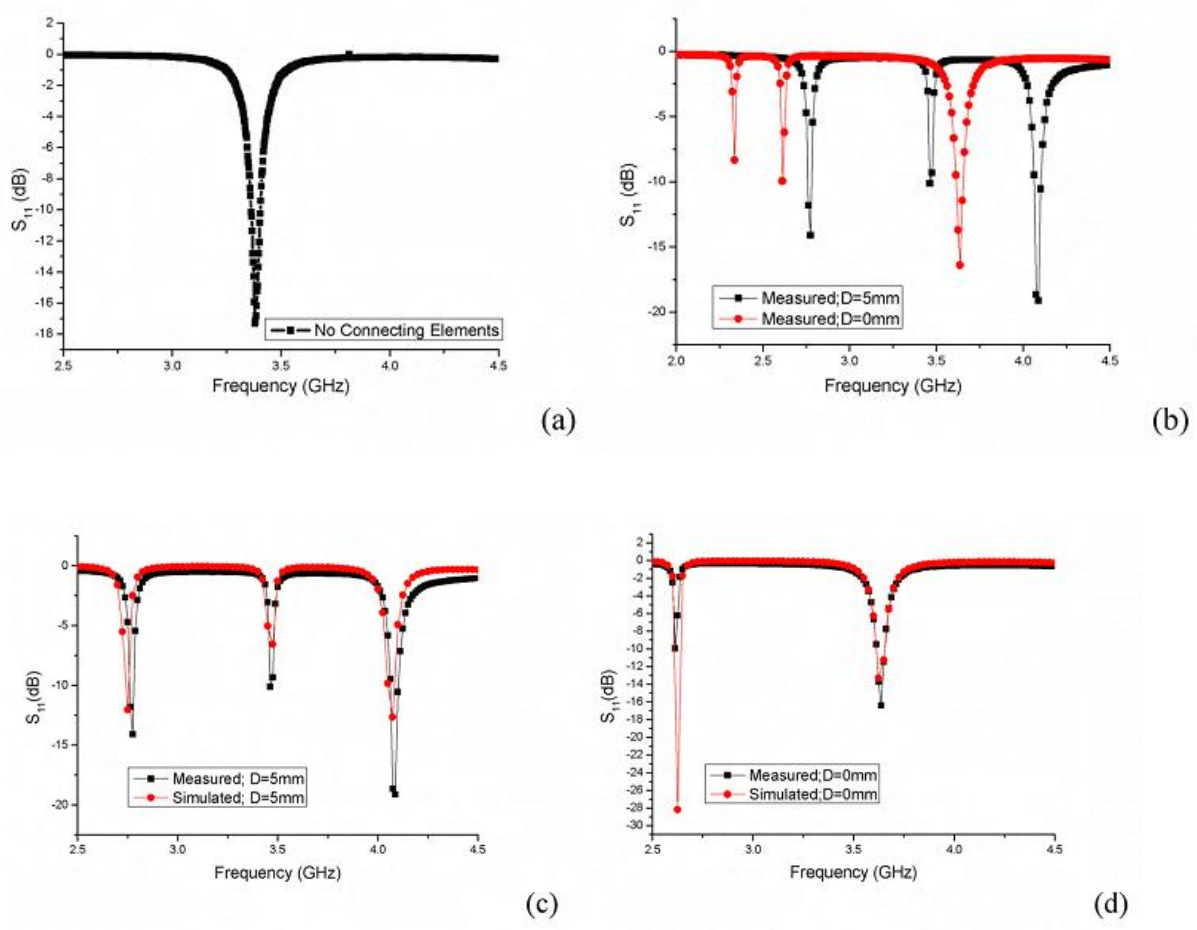

Figure 2-17. (a) The measured S_{11} when there are no connecting elements. (b) S_{11} with D = 5 and 0 mm. Measured and simulated S_{11} when (c) D = 5 mm. (d) D =0mm.

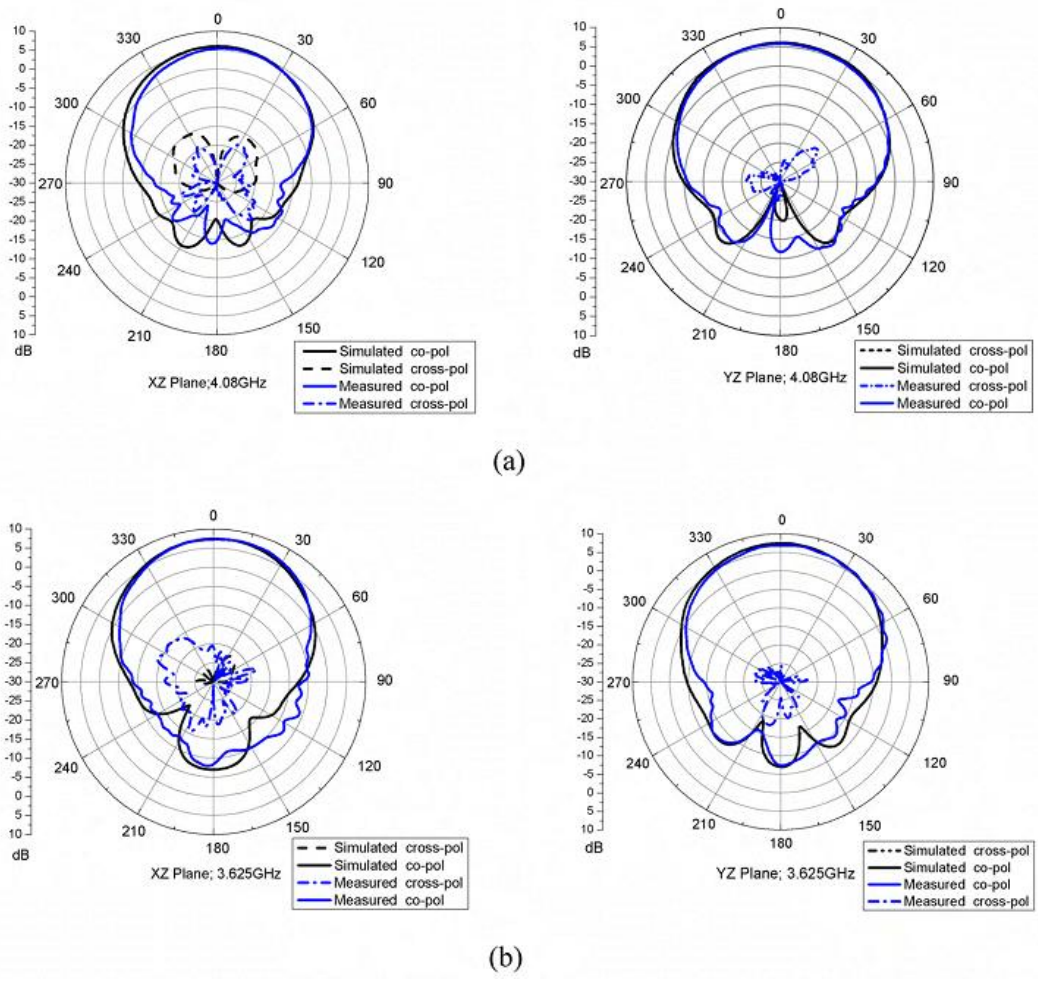

Figure 2-18. Radiation patterns for (a) D = 5 mm. (b) D = 0 mm.

CHAPTER III

COMPACT ULTRA-WIDEBAND RING BANDPASS FILTER*

Introduction

Microstrip ring circuits have many applications in the design of filters, oscillators, mixers, antennas, and couplers [9]-[11]. For filter applications, there are some different kinds of bandpass filters (BPFs): dual-mode ring BPFs [12]-[17], ring slow-wave BPFs [18], ring BPFs with two transmission zeros [19], wideband ring BPFs [20], and others [21]-[24]. Because of the narrow passband feature, additional circuits or microstrip configurations such as microstrip tuning stubs, cascade ring resonators, enhanced coupling stubs, or perturbation stubs are generally used in these structures to create a wider pass band. In this chapter, a compact, wideband ring BPF is proposed by using the harmonic suppression of the even or odd mode resonances with the use of via-hole or slit-gap as the forced boundary condition of a single square ring resonator. It is found that a wide pass band can be created between two allowed half modes (with the side-band suppression greater than 30 dB when the feed-line coupling gaps are voided.

---

* Reprinted with permission from “Simple Wideband Microstrip Ring Bandpass Filter by Utilizing Forced Harmonic Suppression and Direct Feed Line Coupling” by Y. Liu and K. Chang, Microwave and Optical Technology Letter, vol. 54, 8, p.1968, 2012. Copyright 2012 by Wiley.

* Reprinted with permission from "Compact Ultra-Wideband Single Ring Bandpass Filter with Sideband and Harmonic Suppression" by Ya-Chi, Liu and Kai Chang, IEEE AP-S/URSI 2012. Copyright 2012 by IEEE.

Therefore, the design procedure is simplified with no additional circuits and complex microstrip configuration mentioned above. Furthermore, the pass band can be switched to the adjacent band by exchanging the even and odd mode suppression and the bandwidth can be increased by reducing the ring size, which provide flexibility for the ring BPF design.

Fundamental of Microstrip Ring Resonators

The microstrip ring resonator was first proposed in 1969 by P. Troughton for microstrip line phase velocity and dispersion property measurement. The application of ring resonator initially falls on the measurements of the properties of microstrip line discontinuities and then following the antennas, filters, oscillators, mixers, optoelectronic components and couplers etc..

The ring resonator is a simple circuit that is easy to build. This structure only supports waves with wavelength that makes the circumference of the ring its integer multiples. Though the simplicity, many circuits still can be designed based on the ring resonator for different purposes such as integration with solid-state devices or switches. The basic structure of the ring includes feed lines and coupling gaps, as shown in Figure 3-1. When the coupling gap is large, the coupling from the feed line to the ring is regarded as weak coupling. On the contrary, it becomes strong coupling when the coupling gap is small [25].

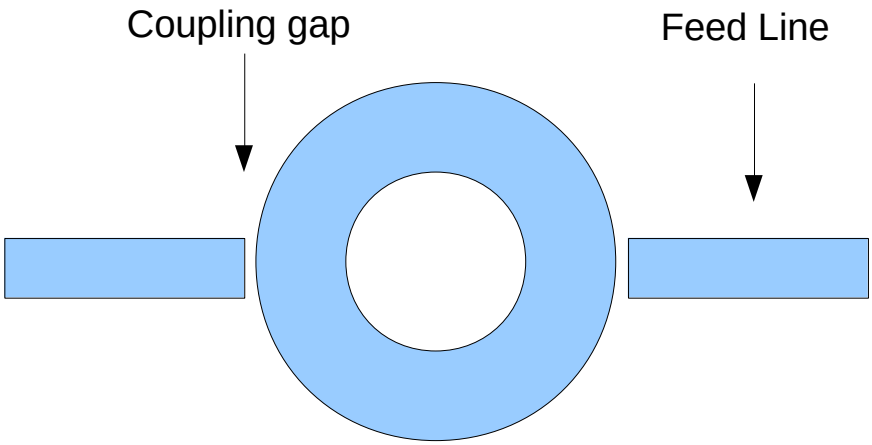

Figure 3-1. Microstrip ring resonator with coupling gaps and feed lines [25].

As mentioned above, when the circumference of the ring is equal to an integer multiples of the signal wavelength then the resonance is constituted. This relation is expressed as:

$$2\pi r = n\,\lambda_g \tag{3-1}$$

where r is the mean radius of the ring, n is the mode number and λ_g is the guided wavelength expressed as:

$$\lambda_g = c\,(\varepsilon_{eff})^{-1/2}/\,f \tag{3-2}$$

where c is the speed of light and ε_{eff} is the effective dielectric constant.

There are mainly two models of the ring resonators used for the analysis of the microstrip ring resonators: magnetic wall model and transmission line model. The

magnetic wall model considered the ring resonator as a ring cavity with PEC (perfect electric conductor; electric wall) on the top and bottom of the ring and with PMC (perfect magnetic conductor; magnetic wall) on inner and outer side walls of it. This model reduces the error caused by the mean radius approximation and considers the ring curvature. The drawback of magnetic wall model is that it did not take the fringing field into account so when the permittivity of the dielectric material is low this model will provide less accuracy [25]. A modification that includes the fringing field effect in the magnetic wall method is required when the original model is inadequate [25].

The magnetic wall model is limited for that it cannot provide the information such as input impedance of the ring resonator. Therefore, transmission line model [30][31] is developed to work out the equivalent circuit of the ring resonator, as shown in Figure 3-2, so that the input impedance and resonant frequency can be determined easily for the circuit design. As depicted in Figure 3-2, the feed lines, coupling gaps and the resonator are modeled as a section of a transmission line respectively and are combined together for the whole circuit.

Here, in Figure 3-2

$$Z_a = j\, Z_o \tan(\beta l / 2) \tag{3-3}$$

$$Z_b = j\, Z_o \csc(\beta l) \tag{3-4}$$

$$C_1 = 1/2\ C_{even} \tag{3-5}$$

$$C_2 = 1/2\ (C_{odd} - 1/2\ C_{even}) \tag{3-6}$$

$$C_{odd} = w\,(s/w)^{mo}\, e^{ko} \tag{3-7}$$

$$C_{even} = 12\, w\,(s/w)^{me}\, e^{ke} \tag{3-8}$$

Where *s* is the coupling gap and *w* is the microstrip width.

For $0.1 <= (s/w) <= 0.3$

$m_e = 0.8675$

$k_e = 2.043(w/h)^{0.12}$

Here, h is the substrate thickness.

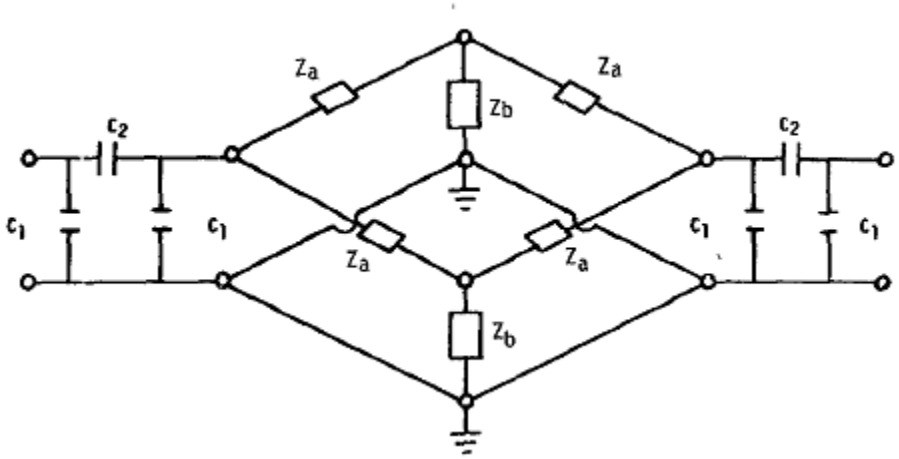

Figure 3-2. Equivalent circuit of the ring resonator shown in Figure 3-1 [25].

Based on equation (3-3) to (3-8), the circuit for the ring resonator can be analyzed more precisely for the estimation of the input impedance, which is important for the microwave filter design.

For the derivation of magnetic wall model and the transmission line model, further information can be found in [31][29][25]. In this chapter, the focus will mainly

put on the utilization of different resonant modes of the ring resonator for the filter design.

Regular Resonant Modes and Forced Resonant Modes

The regular resonant mode of a ring resonator means the circumference of the ring is the integer multiples of the resonance wavelength. As shown in Figure 3-3, the first four resonant modes and the transmission spectrum of a ring resonator are demonstrated. Based on the figure, it is known that the transmission bandwidth of a regular ring resonator is narrow, which is limited for the design of wide band filter. Besides regular resonant modes, there is another kind of modes called forced resonant modes, which are excited by forced boundary conditions on the microstrip ring [25]. The boundary condition can be short or open circuit that are achieved by placing via holes or cutting open slits at the desired location of the ring. To understand more clearly, Figure 3-4 demonstrates a ring with a via hole (short circuit) placed $\lambda_g/4$ away from the feed line. Therefore, E field is zero at the via hole. Based on this forced boundary condition, the resonant modes that can survive in the ring are odd harmonics and their half modes: 0.5 fo, fo, 1.5 fo, 2.5 fo, 3 fo, 3.5 fo...etc.. On the contrary, when the via hole is replaced by an open slit at the same place of the ring, as shown in Figure 3-5, E field is maximum at the slit. Hence, the allowed resonant modes are even harmonics and their half modes: 1.5 fo, 2 fo, 2.5 fo, 3.5 fo, 4 fo, 4.5 fo...etc.. With the presence of the forced boundary

condition, the transmission bandwidth of the ring resonator becomes wider. This property basically can be utilized for the design of wide band filter [27].

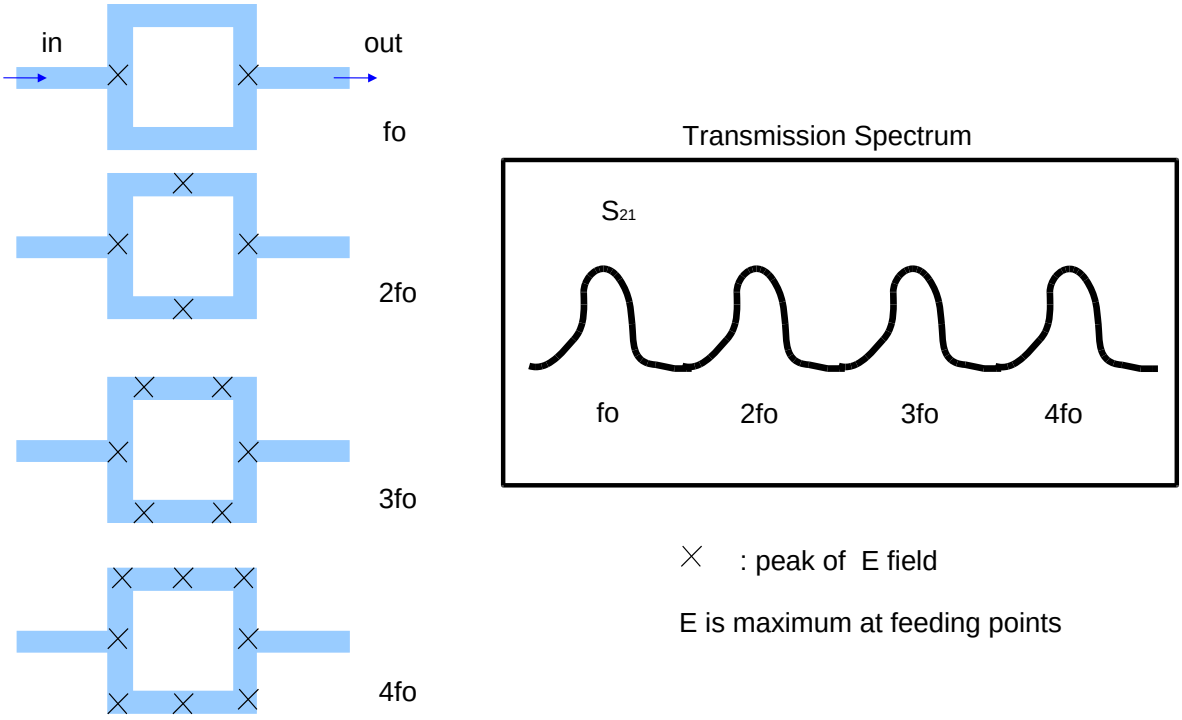

Figure 3-3. The first four modes of a ring resonator.

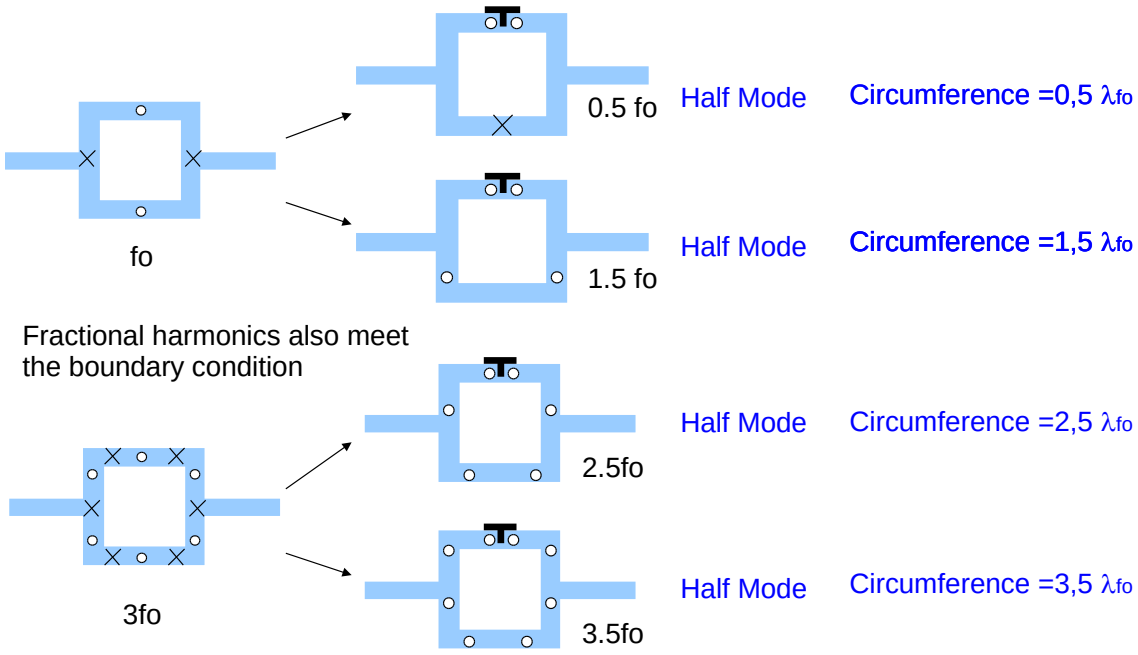

Figure 3-4. A ring with a via hole (short circuit) placed $\lambda_g/4$ away from the feed line.

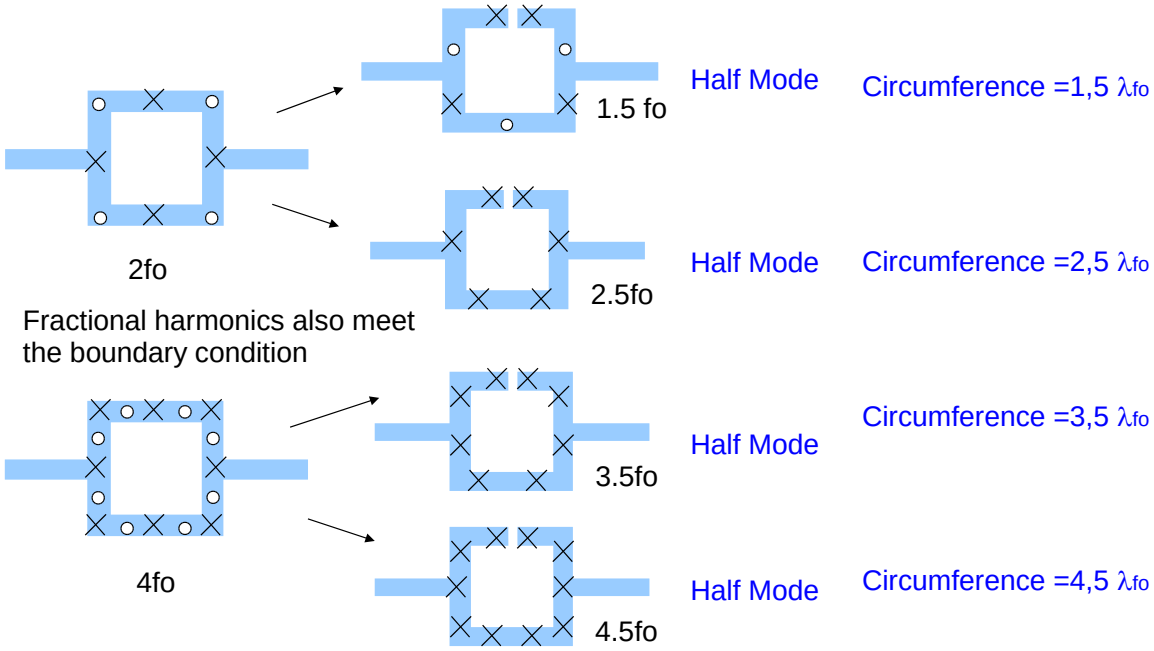

Figure 3-5. A ring with a slit (open circuit) placed $\lambda_g/4$ away from the feed line.

Feed Line Coupling Gap

The flatness of the pass band is one of the important issues for the design of band pass filters. For a ring resonator, the gap of the feed line controls the strength of the coupling to the ring. Figure 3-6 shows the simulation of the transmission spectrum of a ring with short circuit forced boundary condition. For the case with the feed line coupling gap, the three resonant modes are clearly seen on the spectrum. However, this pass band with ripple is not ideal to serve as a filter. To solve this problem, the coupling gap is removed. As shown in Figure 3-7, when the coupling gap is removed, the transmission band is flattened and can be utilized for the filter design, which will be discussed in the next section.

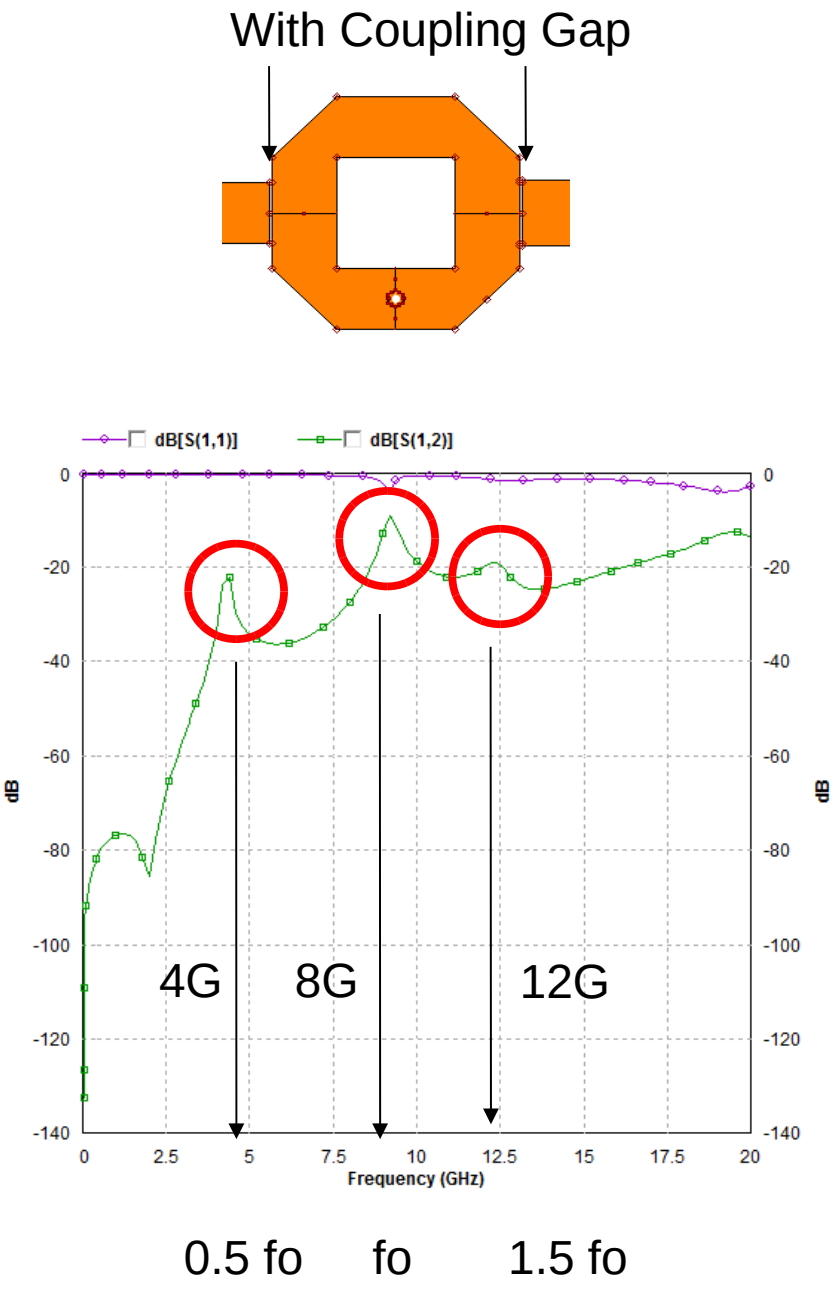

Figure 3-6. The spectrum of a ring with coupling gaps.

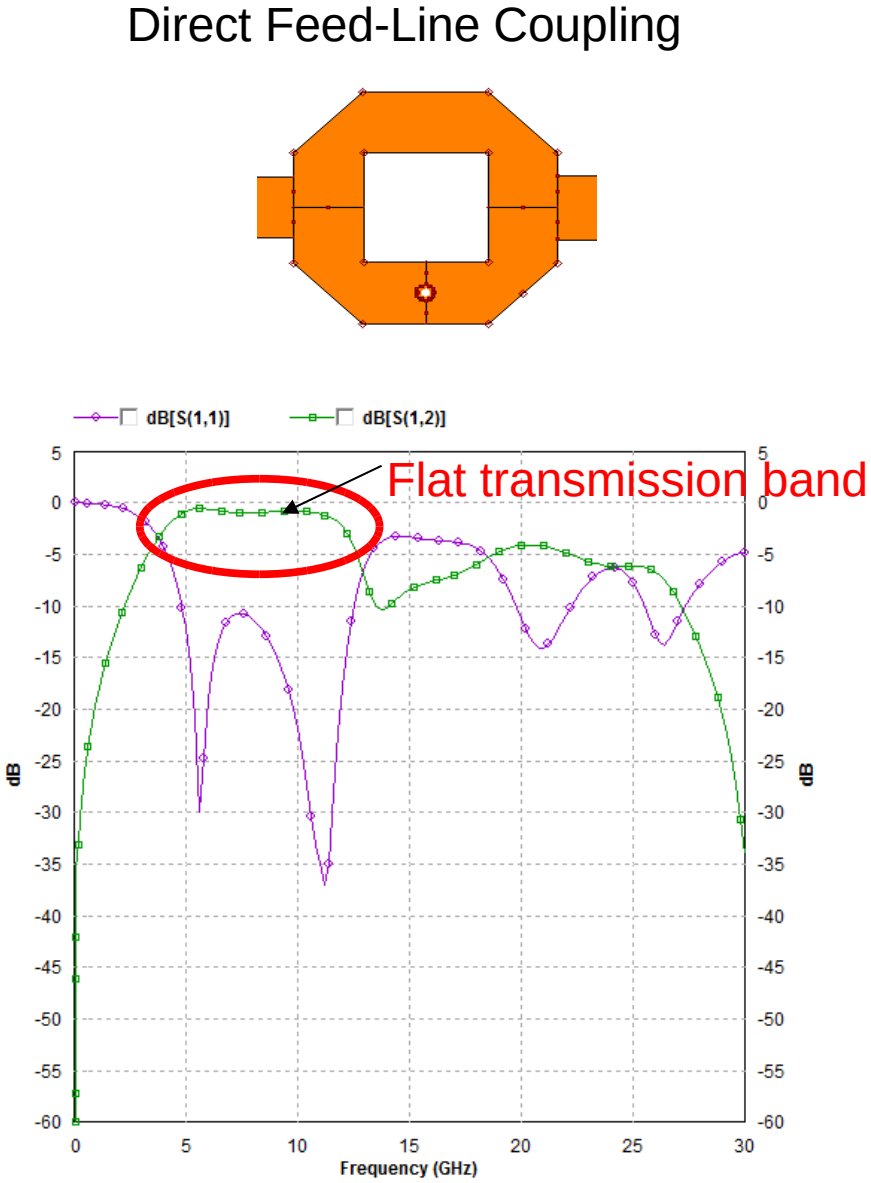

Figure 3-7. The spectrum of a ring without coupling gaps.

Filter Structure and Analysis

Figure 3-8 shows two square ring resonators with a slit-gap and a via-hole at position $\lambda_g/4$ away from the feed line, respectively, where λ_g is the guided-wavelength of the fundamental resonance. The slit-gap and the via-hole are used to force the boundary condition of the ring resonator to be open and short, respectively. At the gap region (open circuit), the current distribution is minimum and hence the electric field is maximum. On the contrary, the current distribution is maximum and the electric field is minimum at the via-hole (short circuit). In the previous section, it is known that, in addition to regular modes, a ring resonator with coupling gaps can also support half modes when there is a perturbation at position $\lambda_g/4$ away from the feed line [25], that is, the circumference of the ring resonator can be odd integer multiples of the resonant mode's half wavelength. To have the qualified pass band, the feed line coupling gaps are voided to reduce the coupling loss and the transmission loss between two allowed half modes. As demonstrated in the previous section, without the presence of coupling gaps, a wide pass band will appear on the spectrum between the allowed half modes of a perturbed single ring resonator of which the structure is simpler than other proposed ring-based BPFs [12], [20], [17], [19], [23].

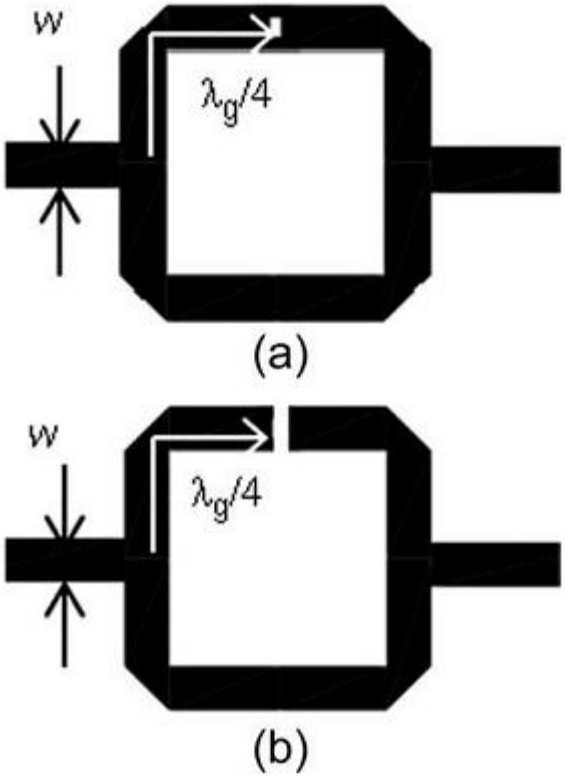

Figure 3-8. Layout of the harmonic-suppression ring resonators: (a) Short circuit with a via hole (hole diameter ~ 0.3 mm). (b) Open circuit with a slit gap (gap width ~ 0.6 mm)

Experiment and Measurement Results

The schematic diagram and designed parameters of the ring BPF are shown in Figure 3-8 and Table 3-1, respectively. Here, Rogers RT5880 Duroid substrate ($\varepsilon_r = 2.2$) with 30 mil thickness is used in the circuit fabrication and the characteristic impedance of all microstrip sections are designed to be 50Ω. For data comparison, two square ring resonators are designed with fundamental resonant frequencies (f_0) at 2 and 4 GHz individually.

The measured and simulated results are shown in Figures 3-9 and Figure 3-10. According to S_{21}, for resonators with slit-gaps (open circuit), the odd resonant modes are suppressed, as depicted in Figure 3-9(a) and Figure 3-10(a). On the contrary, the even resonant modes are suppressed for resonators with via-holes (short circuit), as depicted in Figure 3-9(b) and Figure 3-10(b). The feed line coupling gaps are voided and the feed line position is slightly adjusted to reduce the reflection (S_{11}) of the ring resonator so that the window between two aforementioned allow half modes can serve as the pass band of the BPFs.

Additionally, from Figures 3-9 and Figure 3-10, it can be recognized that the pass bands of the odd-mode-suppressed BPF and the even-mode-suppressed BPF are complementary, which indicates the operating pass band can be adjusted to work at the adjacent band without changing the size of the ring resonator but swapping the via-hole and the slit-gap. Furthermore, owing to the bandwidth between two adjacent resonant modes is wider for a smaller ring, it is understandable that why the 3 dB bandwidth of the pass band is about 2 GHz for the for the resonator with $f_0 = 2$ GHz and about 4 GHz

for the resonator with f_0 = 4 GHz. Based on the measurement data, the return loss in the pass band is greater than 10 *dB* and the sideband suppression is around 30 *dB* or more. Finally, EM simulations with IE3D [26] are in good agreement with the measurement results.

Table 3-1. Design parameters.

f_0	λ_g	w	slit gap/via hole size
2 GHz	10.93 cm	2.41 mm	0.6 mm (slit gap width) 0.3 mm (via hole diameter)
4 GHz	5.46 cm	2.41 mm	0.6 mm (slit gap width) 0.3 mm (via hole diameter)

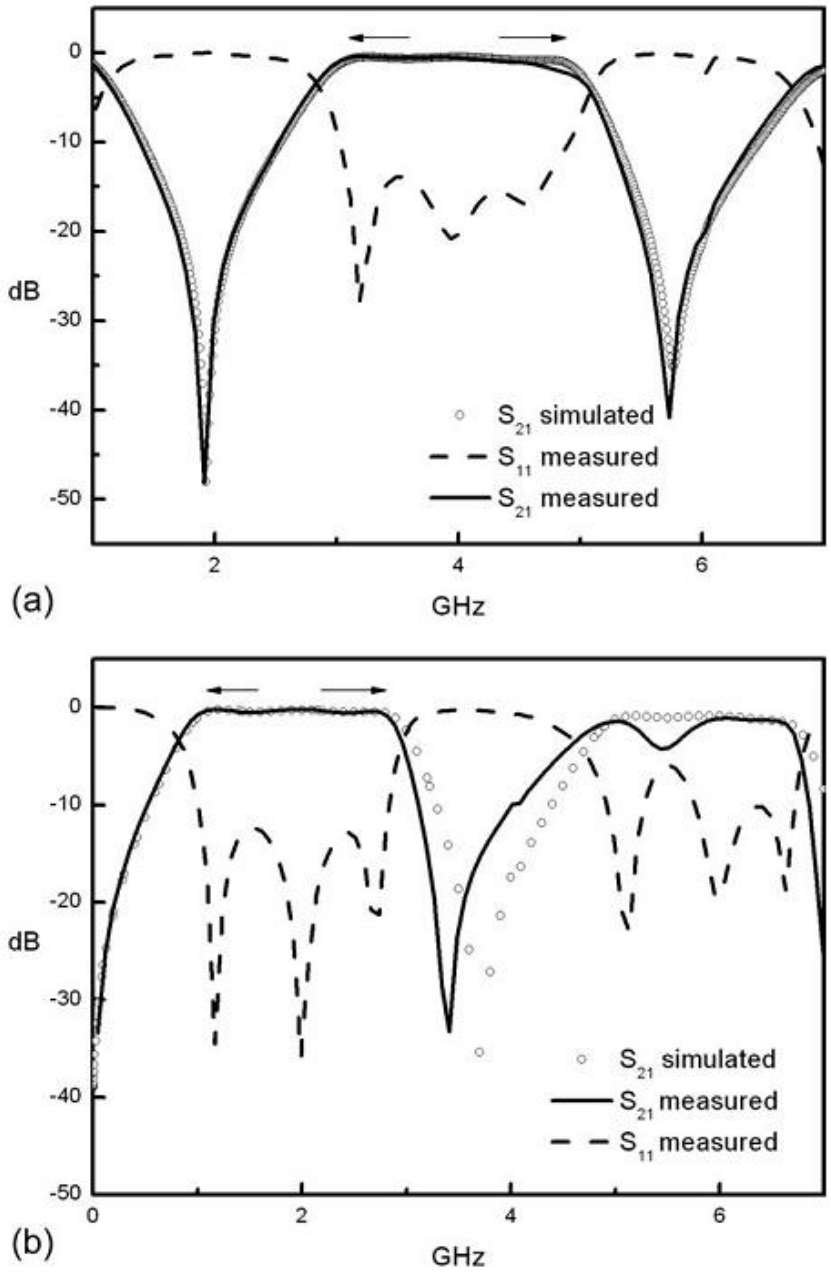

Figure 3-9. Measurement and simulation results for the resonator with f_0 at 2 GHz: (a) Odd mode suppression (open circuit).The two allowed half modes are at f =1.5 f_0 and f = 2.5 f_0. (b) Even mode suppression (short circuit). The two allowed half modes are at f = 0.5 f_0 and f =1.5 f_0. Arrows are used to indicate the pass band.

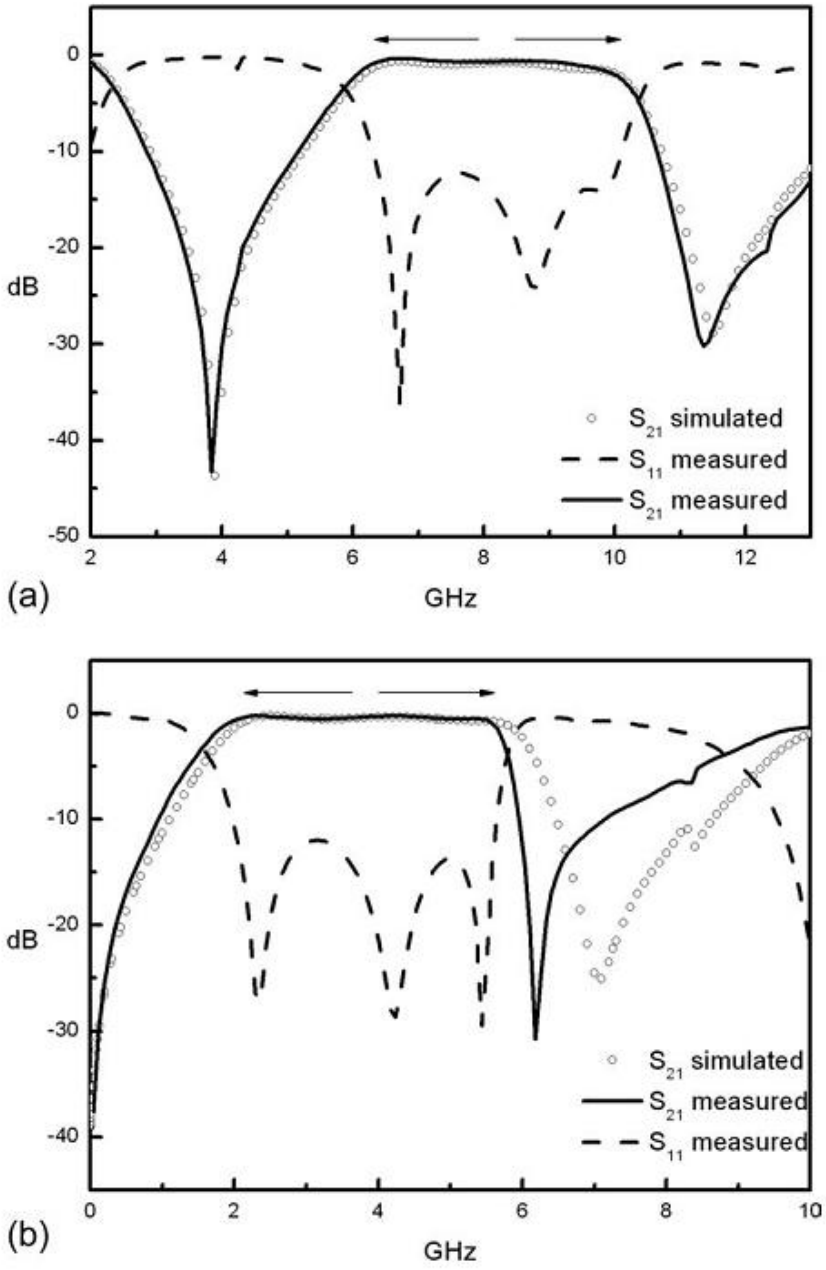

Figure 3-10. Measurement and simulation results for the resonator with f_0 at 4 GHz: (a) Odd mode suppression (open circuit).The two allowed half modes are at f =1.5 f_0 and f = 2.5 f_0. (b) Even mode suppression (short circuit). The two allowed half modes are at f = 0.5 f_0 and f =1.5 f_0. Arrows are used to indicate the pass band.

Side Band Suppression with Low Pass Filter

In the previous section, the utilization of half modes of a ring resonator for the filter design is introduced. However, the unwanted side band sill has to be eliminated to validate the filter design. Therefore, additional circuits are needed to perform the side band suppression. In this section, a simple and compact ultra wide band bandpass filter from 4GHz to 12GHz designed by imposing a single microstrip ring resonator and stepped-impedance filter to achieve sideband suppression is studied. Both simulation and measurement data are in good agreement and the group delay variation in the pass-band is less than 0.3 ns [28].

As shown in Figure 3-7, the sideband over 12 GHz still has to be suppressed to prevent the desired pass-band signal being interfered. To achieve the side band suppression, the ring and a 10th order maximum flat stepped-impedance low pass filter are cascaded together, as shown in Figure 3-11 with the structure parameters listed in Table 3-2. Figure 3-12 and Figure 3-13 are the simulation and measurement data of the transmission spectrum as well as group delay of the filter respectively. Rogers RT5880 Duriod substrate (εr=2.2) with 30 mil thickness is used in the circuit fabrication and the characteristic impedance of different strip widths used in the design are 30Ω, 50 Ω and 135 Ω respectively. According to measurement data, within the pass band, the return loss is greater than 10dB between 4GHz and 12GHz and the transmission zeros aside are greater than 20dB; the group delay variation is less than 0.3ns. Both simulation and measurement data are in good agreement.

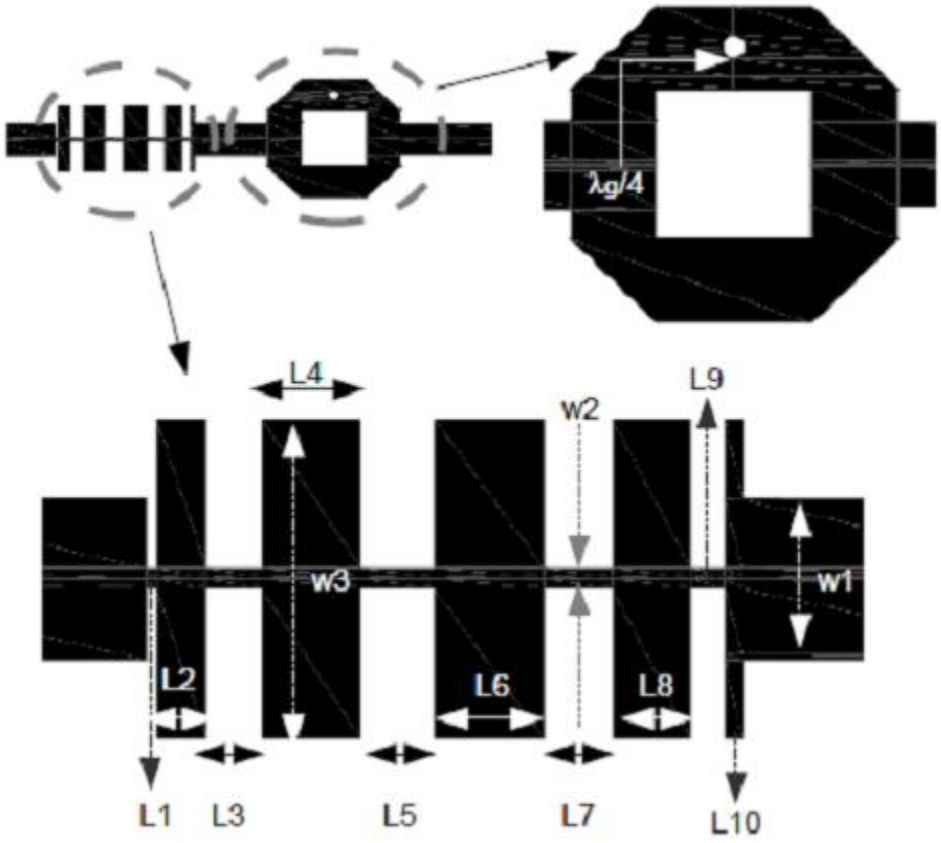

Figure 3-11. Layout of the UWB filter.

Table 3-1. Structure parameters for the UWB filter depicted in Figure 3-11.

f_o	λ_g	w1	w2	w3	L1	L2	L3
8 GHz	2.73 mm	2.56 mm	0.33 mm	5.13 mm	0.19 mm	0.82 mm	0.86 mm
L4	**L5**	**L6**	**L7**	**L8**	**L9**	**L10**	
1.61 mm	1.20 mm	1.79 mm	1.08 mm	1.28 mm	0.55 mm	0.28 mm	

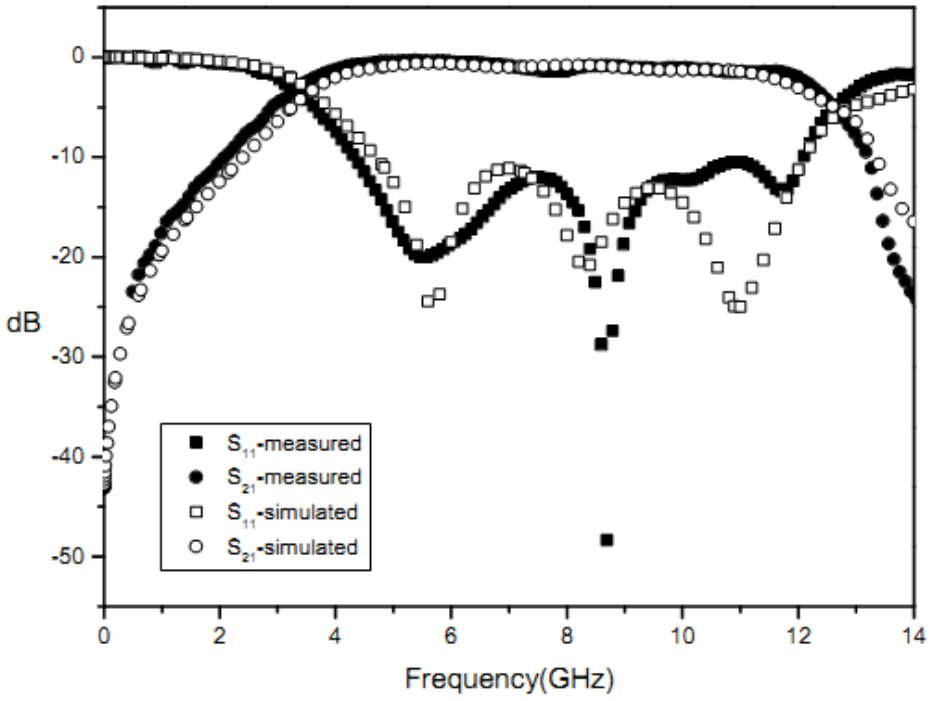

Figure 3-12. Reflection and transmission spectrum of the designed UWB filter.

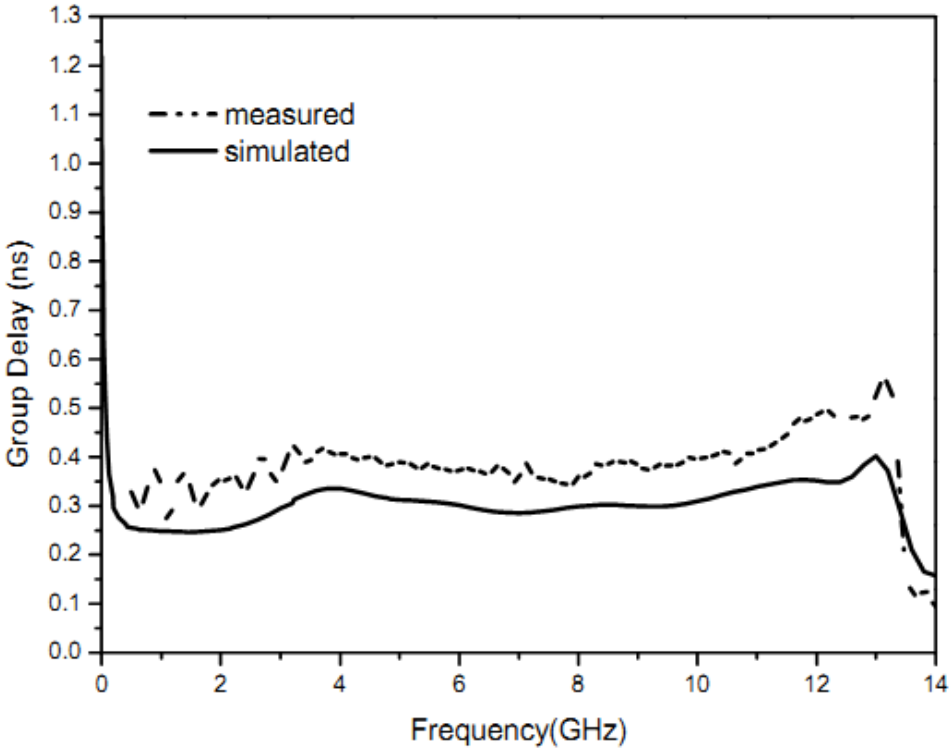

Figure 3-13. Measured and simulated group delay of the designed UWB filter.

Conclusion

The design of a compact single-ring BPF with a broad pass band is discussed and demonstrated in this article. The via-hole and slit-gap are used as the forced boundary condition to introduce the even/odd mode harmonic suppression. Without the feed line coupling gaps, the transmission loss between two allowed half modes will be reduced and hence the pass band of the BPF is created. The proposed structure differs from the narrow-pass band nature of a single-ring resonator and thus provides an alternative approach for the design of ring based BPFs.

CHAPTER IV

FDTD-FINITE DIFFERENCE TIME DOMAIN METHOD

Introduction

The Finite Difference Time Domain (FDTD) Method is greatly used in the study of microwave or optical structures for its simple algorithm. Compared with other numerical methods, FDTD offers a straight-forward way for programmers to do the simulation of wave propagation in time domain. One only needs to rewrite Maxwell's Equations into finite difference equations and apply field iteration. In addition to its simple algorithm, FDTD is efficient for dealing with wide band simulations since it is time domain iteration. The broad band field information can be obtained by one single run with a short pulse excitation in time domain.

The basic FDTD numerical techniques for solving EM waves directly in the time domain on a space grid was described by Yee in 1966 [32]. Yee proposed to sample the spatial vector components of the electric and magnetic fields in a staggered manner, as shown in Figure 4-1, which enables the differential or integral forms of Maxwell's equations in a robust manner. In Yee's paper, the FDTD is second-order accurate in both time and space domains with the use of central difference for Maxwell's differential equations. Due to the finite difference form of the differential equations, numerical dispersion and numerical stability are the main issues need to be considered in FDTD, which are determined by the cell size in space and time. To maintain the numerical stability, generally the cell size has to be sufficiently small in comparison to the

wavelength (generally 1/20 to 1/30 of the wavelength). This will be discussed further in later sections of this chapter.

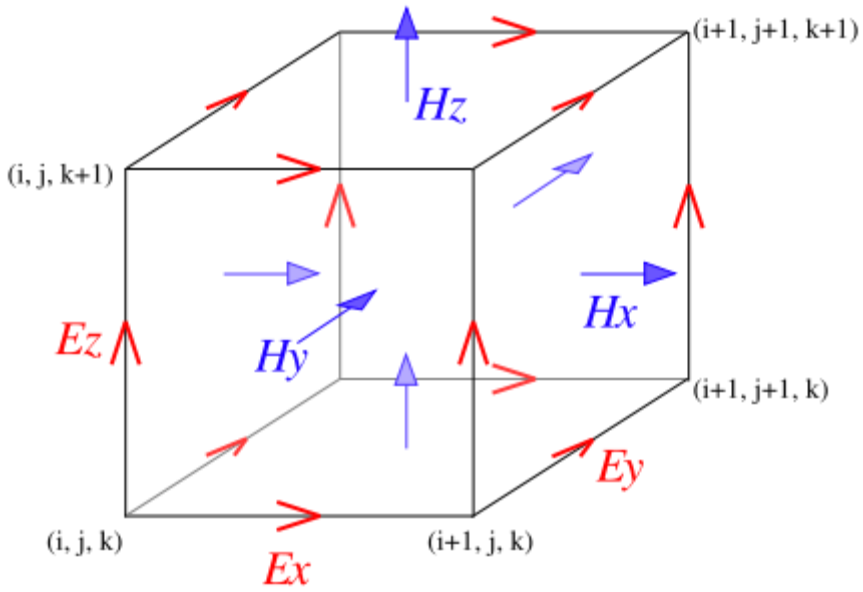

Figure 4-1. Yee's Lattice [33].

Yee's Algorithm and Maxwell Equations

Consider a space having no electric or magnetic current sources but lossy electric or magnetic materials. The time-dependent Maxwell's Equations with differential form are given as:

$$\nabla \times \vec{E} = -\vec{M} - \frac{\partial \vec{B}}{\partial t} \textit{ (Faraday's Law)} \quad (4\text{-}1)$$

$$\nabla \times \vec{H} = \vec{J} + \frac{\partial \vec{D}}{\partial t} \textit{ (Ampere's Law)} \quad (4\text{-}2)$$

$$\nabla \cdot \vec{D} = \rho_e \textit{ (Gauss's Law for electric field)} \quad (4\text{-}3)$$

$$\nabla \cdot \vec{E} = \rho_m \textit{ (Gauss's Law for magnetic field)} \quad (4\text{-}4)$$

where,

$\vec{E}$: Electrical field intensity (V/m)

$\vec{H}$: Magnetic field intensity (A/m)

$\vec{D}$: Electric flux density (C/m^2)

$\vec{B}$: Magnetic flux density (Wb/m^2)

$\vec{J}$: Electric current density (A/m^2)

$\vec{M}$: Magnetic current density (V/m^2)

ρ_e: Electric charge density (C/m^2)

ρ_m: Magnetic charge density (Wb/m^2)

For linear, isotropic and non-dispersive materials, D and B are presented as follows:

$$\vec{D} = \varepsilon_r \varepsilon_0 \vec{E} = \varepsilon \vec{E}$$

$$\vec{B} = \mu_r \mu_0 \vec{H} = \mu \vec{H} \quad (4\text{-}5)$$

Substituting (4-5) into (4-1) and (4-2), the vector form Maxwell's curl equations for linear, isotropic, non-dispersive and source free with zero magnetic losses media become:

$$\nabla \times \vec{H} = \sigma \vec{E} + \varepsilon \frac{\partial \vec{E}}{\partial t} \tag{4-6}$$

$$\nabla \times \vec{E} = -\mu \frac{\partial \vec{H}}{\partial t} \tag{4-7}$$

The scalar form of (4-6) and (4-7) yields six coupled equations for Cartesian coordinate:

$$\frac{\partial H_x}{\partial t} = -\frac{1}{\mu}\left(\frac{\partial E_z}{\partial y} - \frac{\partial E_y}{\partial z}\right) \tag{4-8}$$

$$\frac{\partial H_y}{\partial t} = -\frac{1}{\mu}\left(\frac{\partial E_x}{\partial z} - \frac{\partial E_z}{\partial x}\right) \tag{4-9}$$

$$\frac{\partial H_z}{\partial t} = -\frac{1}{\mu}\left(\frac{\partial E_x}{\partial y} - \frac{\partial E_y}{\partial x}\right) \tag{4-10}$$

$$\frac{\partial E_x}{\partial t} = -\frac{1}{\varepsilon}\left(\frac{\partial H_z}{\partial y} - \frac{\partial H_y}{\partial z} - \sigma E_x\right) \tag{4-11}$$

$$\frac{\partial E_y}{\partial t} = -\frac{1}{\varepsilon}\left(\frac{\partial H_x}{\partial z} - \frac{\partial H_z}{\partial x} - \sigma E_y\right) \tag{4-12}$$

$$\frac{\partial E_z}{\partial t} = -\frac{1}{\varepsilon}\left(\frac{\partial H_x}{\partial y} - \frac{\partial H_y}{\partial x} - \sigma E_z\right) \tag{4-13}$$

The above six partial differential equations are the government FDTD equations for the simulation of electromagnetic wave interacting with arbitrary 3D objects. Based on Yee's idea, the first order differentiation of Equations (4-8) to (4-13) with respect to space and time are approximated by central differences. Then all field components are worked out via the leapfrog iteration scheme.

Based on Yee's mesh in space shown in Figure 1, Equation (4-8) to (4-13) can be expressed as follows:

$$H^{n+\frac{1}{2}}_{x(i,j+\frac{1}{2},k+\frac{1}{2})} = H^{n-\frac{1}{2}}_{x(i,j+\frac{1}{2},k+\frac{1}{2})} - \frac{\Delta t}{\mu}\left[\frac{1}{\Delta y}\left(E^{n}_{z\left(i,j+1,k+\frac{1}{2}\right)} - E^{n}_{z\left(i,j,k+\frac{1}{2}\right)}\right) - \frac{1}{\Delta z}\left(E^{n}_{y\left(i,j+\frac{1}{2},k+1\right)} - E^{n}_{y\left(i,j+\frac{1}{2},k\right)}\right)\right] \quad (4\text{-}14)$$

$$H^{n+\frac{1}{2}}_{y(i+\frac{1}{2},j,k+\frac{1}{2})} = H^{n-\frac{1}{2}}_{y(i+\frac{1}{2},j,k+\frac{1}{2})} - \frac{\Delta t}{\mu}\left[\frac{1}{\Delta z}\left(E^{n}_{x\left(i+\frac{1}{2},j,k+1\right)} - E^{n}_{x\left(i+\frac{1}{2},j,k\right)}\right) - \frac{1}{\Delta x}\left(E^{n}_{z(i+1,j,k)} - E^{n}_{z\left(i,j,k+\frac{1}{2}\right)}\right)\right] \quad (4\text{-}15)$$

$$H^{n+\frac{1}{2}}_{z(i+\frac{1}{2},j+\frac{1}{2},k)} = H^{n-\frac{1}{2}}_{z(i+\frac{1}{2},j+\frac{1}{2},k)} - \frac{\Delta t}{\mu}\left[\frac{1}{\Delta x}\left(E^{n}_{y\left(i,j+\frac{1}{2},k+1\right)} - E^{n}_{y\left(i,j+\frac{1}{2},k\right)}\right) - \frac{1}{\Delta y}\left(E^{n}_{x\left(i,j+\frac{1}{2},k+1\right)} - E^{n}_{x\left(i+\frac{1}{2},j,k\right)}\right)\right] \quad (4\text{-}16)$$

$$E^{n+\frac{1}{2}}_{x(i+\frac{1}{2},j,k)} = \left(\frac{1-\frac{\sigma\Delta t}{2\varepsilon}}{1+\frac{\sigma\Delta t}{2\varepsilon}}\right)E^{n-\frac{1}{2}}_{x\left(i+\frac{1}{2},j,k\right)} - \frac{\frac{\sigma\Delta t}{2\varepsilon}}{1+\frac{\sigma\Delta t}{2\varepsilon}}\left[\frac{1}{\Delta y}\left(H^{n+\frac{1}{2}}_{z\left(i+\frac{1}{2},j,k+\frac{1}{2}\right)} - H^{n+\frac{1}{2}}_{z\left(i+\frac{1}{2},j-\frac{1}{2},k\right)}\right) - \frac{1}{\Delta z}\left(H^{n+\frac{1}{2}}_{y\left(i+\frac{1}{2},j,k+\frac{1}{2}\right)} - H^{n+\frac{1}{2}}_{y\left(i+\frac{1}{2},j,k-\frac{1}{2}\right)}\right)\right] \quad (4\text{-}17)$$

$$E^{n+\frac{1}{2}}_{y(i,j+\frac{1}{2},k)} = \left(\frac{1-\frac{\sigma\Delta t}{2\varepsilon}}{1+\frac{\sigma\Delta t}{2\varepsilon}}\right)E^{n-\frac{1}{2}}_{y\left(i,j+\frac{1}{2},k\right)} - \frac{\frac{\sigma\Delta t}{2\varepsilon}}{1+\frac{\sigma\Delta t}{2\varepsilon}}\left[\frac{1}{\Delta z}\left(H^{n+\frac{1}{2}}_{x\left(i,j+\frac{1}{2},k+\frac{1}{2}\right)} - H^{n+\frac{1}{2}}_{x\left(i,j+\frac{1}{2},k-\frac{1}{2}\right)}\right) - \frac{1}{\Delta x}\left(H^{n+\frac{1}{2}}_{z\left(i+\frac{1}{2},j+\frac{1}{2},k\right)} - H^{n+\frac{1}{2}}_{z\left(i-\frac{1}{2},j+\frac{1}{2},k\right)}\right)\right] \quad (4\text{-}18)$$

$$E^{n+\frac{1}{2}}_{z(i,j,k+\frac{1}{2})} = \left(\frac{1-\frac{\sigma\Delta t}{2\varepsilon}}{1+\frac{\sigma\Delta t}{2\varepsilon}}\right)E^{n-\frac{1}{2}}_{z\left(i,j,k+\frac{1}{2}\right)} - \frac{\frac{\sigma\Delta t}{2\varepsilon}}{1+\frac{\sigma\Delta t}{2\varepsilon}}\left[\frac{1}{\Delta x}\left(H^{n+\frac{1}{2}}_{y\left(i+\frac{1}{2},j,k+\frac{1}{2}\right)} - H^{n+\frac{1}{2}}_{y\left(i+\frac{1}{2},j,k+\frac{1}{2}\right)}\right) - \frac{1}{\Delta y}\left(H^{n+\frac{1}{2}}_{x\left(i,j+\frac{1}{2},k+\frac{1}{2}\right)} - H^{n+\frac{1}{2}}_{x\left(i,j-\frac{1}{2},k+\frac{1}{2}\right)}\right)\right] \quad (4\text{-}19)$$

Equation (4-14) to (4-19) then can be rearranged as the following update equations:

$$H^{n+\frac{1}{2}}_{x(i,j,k)} = H^{n-\frac{1}{2}}_{x(i,j,k)} - \frac{\Delta t}{\mu}\left[\frac{1}{\Delta y}\left(E^{n}_{z(i,j+1,k)} - E^{n}_{z(i,j+1,k)}\right) - \frac{1}{\Delta z}\left(E^{n}_{y(i,j,k+1)} - E^{n}_{y(i,j,k)}\right)\right] \quad (4\text{-}20)$$

$$H_{y(i,j,k)}^{n+\frac{1}{2}} = H_{y(i,j,k)}^{n-\frac{1}{2}} - \frac{\Delta t}{\mu}\left[\frac{1}{\Delta z}\left(E_{x(i,j,k+1)}^{n} - E_{x(i,j,k)}^{n}\right) - \frac{1}{\Delta x}\left(E_{z(i+1,j,k)}^{n} - E_{z(i,j,k)}^{n}\right)\right] \quad (4\text{-}21)$$

$$H_{z(i,j,k)}^{n+\frac{1}{2}} = H_{z(i,j,k)}^{n-\frac{1}{2}} - \frac{\Delta t}{\mu}\left[\frac{1}{\Delta x}\left(E_{y(i,j,k+1)}^{n} - E_{y(i,j,k)}^{n}\right) - \frac{1}{\Delta y}\left(E_{x(i,j,k+1)}^{n} - E_{x(i,j,k)}^{n}\right)\right] \quad (4\text{-}22)$$

$$E_{x(i,j,k)}^{n+\frac{1}{2}} = \left(\frac{1-\frac{\sigma\Delta t}{2\varepsilon}}{1+\frac{\sigma\Delta t}{2\varepsilon}}\right) E_{x(i,j,k)}^{n-\frac{1}{2}} - \frac{\frac{\sigma\Delta t}{2\varepsilon}}{1+\frac{\sigma\Delta t}{2\varepsilon}}\left[\frac{1}{\Delta y}\left(H_{z(i,j,k)}^{n+\frac{1}{2}} - H_{z(i,j-1,k)}^{n+\frac{1}{2}}\right) - \frac{1}{\Delta z}\left(H_{y(i,j,k)}^{n+\frac{1}{2}} - H_{y(i,j,k-1)}^{n+\frac{1}{2}}\right)\right] \quad (4\text{-}23)$$

$$E_{y(i,j,k)}^{n+\frac{1}{2}} = \left(\frac{1-\frac{\sigma\Delta t}{2\varepsilon}}{1+\frac{\sigma\Delta t}{2\varepsilon}}\right) E_{y(i,j,k)}^{n-\frac{1}{2}} - \frac{\frac{\sigma\Delta t}{2\varepsilon}}{1+\frac{\sigma\Delta t}{2\varepsilon}}\left[\frac{1}{\Delta z}\left(H_{x(i,j,k)}^{n+\frac{1}{2}} - H_{x(i,j,k-1)}^{n+\frac{1}{2}}\right) - \frac{1}{\Delta x}\left(H_{z(i,j,k)}^{n+\frac{1}{2}} - H_{z(i-1,j,k)}^{n+\frac{1}{2}}\right)\right] \quad (4\text{-}24)$$

$$E_{z(i,j,k)}^{n+\frac{1}{2}} = \left(\frac{1-\frac{\sigma\Delta t}{2\varepsilon}}{1+\frac{\sigma\Delta t}{2\varepsilon}}\right) E_{z(i,j,k)}^{n-\frac{1}{2}} - \frac{\frac{\sigma\Delta t}{2\varepsilon}}{1+\frac{\sigma\Delta t}{2\varepsilon}}\left[\frac{1}{\Delta x}\left(H_{y(i,j,k)}^{n+\frac{1}{2}} - H_{y(i-1,j,k)}^{n+\frac{1}{2}}\right) - \frac{1}{\Delta y}\left(H_{x(i,j,k)}^{n+\frac{1}{2}} - H_{x(i,j-1,k)}^{n+\frac{1}{2}}\right)\right] \quad (4\text{-}25)$$

The above update equations then are solved by leapfrog scheme, as shown in Figure 4-2, which implies that electric and magnetic field are not updated at the same time but alternatively in real time scale since the time grids for E and H field are staggered with 0.5 Δt time spacing for numerical stability. The above updating equations denote that the newly updated H depends on current E and previously updated H. By the same way, the newly update E depends on current H and previous updated E. This updating process (or called iteration) is repeated until the last time step is reached.

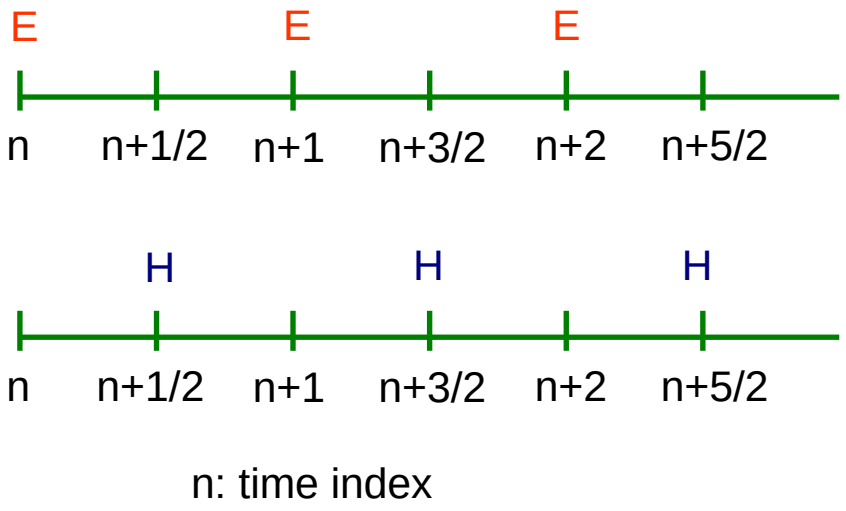

Figure 4-2. Leapfrog scheme.

Numerical Dispersion and Numerical Stability

The central difference approximation of the differential form Maxwell Equations causes nonphysical dispersion of the simulated waves in a free-space computational lattice [34]. That is, the phase velocity of numerical wave modes can differ from *c* by an amount varying with the wavelength, direction of propagation in the grid, and grid demonetization. This phenomenon is called numerical dispersion, which must be taken into account in FDTD for accuracy consideration.

For further understanding about numerical dispersion, now Maxwell Equation for TM_z wave in 2-D is considered.

$$\frac{\partial H_x}{\partial t} = -\frac{1}{\mu}\frac{\partial E_z}{\partial y} \tag{4-26}$$

$$\frac{\partial H_y}{\partial t} = \frac{1}{\mu}\frac{\partial E_z}{\partial x} \tag{4-27}$$

$$\frac{\partial E_z}{\partial t} = \frac{1}{\varepsilon}\left(\frac{\partial H_y}{\partial x} - \frac{\partial H_x}{\partial y}\right) \tag{4-28}$$

The finite difference equations of (4-26) to (4-28) with central difference approximation are:

$$\frac{H_{x_{i,j+1/2}}^{n+1/2} - H_{x_{i,j+1/2}}^{n-1/2}}{\Delta t} = -\frac{1}{\mu}\frac{E_{z_{i,j+1}}^{n} - E_{z_{i,j}}^{n}}{\Delta y} \tag{4-29}$$

$$\frac{H_{y_{i+1/2,j}}^{n+1/2} - H_{y_{i+1/2,j}}^{n-1/2}}{\Delta t} = \frac{1}{\mu}\frac{E_{z_{i+1,j}}^{n} - E_{z_{i,j}}^{n}}{\Delta x} \tag{4-30}$$

$$\frac{E_{z_{i,j}}^{n+1} - E_{z_{i,j}}^{n}}{\Delta t} = \frac{1}{\varepsilon}\frac{H_{y_{i+1/2,j}}^{n+1/2} - H_{y_{i-1/2,j}}^{n+1/2}}{\Delta x} - \frac{1}{\varepsilon}\frac{H_{x_{i,j+1/2}}^{n+1/2} - H_{x_{i,j-1/2}}^{n+1/2}}{\Delta y} \tag{4-31}$$

Because E and H are harmonic functions, the numerical E_n and H_n field can be expressed as complex exponential:

$$E_{z_{I,J}}^{n} = E_{z_0} e^{j(\omega n\Delta t - \tilde{k}_x I\Delta x - \tilde{k}_y J\Delta y)} \tag{4-32}$$

$$H_{x_{I,J}}^{n} = H_{x_0} e^{j(\omega n\Delta t - \tilde{k}_x I\Delta x - \tilde{k}_y J\Delta y)} \tag{4-33}$$

$$H_{y_{I,J}}^{n} = H_{y_0} e^{j(\omega n\Delta t - \tilde{k}_x I\Delta x - \tilde{k}_y J\Delta y)} \tag{4-34}$$

Where k_x, k_y are numerical wave vector and E_z, H_{xo}, H_{yo} are mode amplitude

Substitute (4-29) to (4-31) into (4-32) to (4-34) yields the mode amplitudes

$$H_{x_0} = \frac{\Delta t E_{z_0}}{\mu\Delta y}\frac{\sin(\tilde{k}_y\Delta y/2)}{\sin(\omega\Delta t/2)} \tag{4-35}$$

$$H_{y_0} = -\frac{\Delta t E_{z_0}}{\mu \Delta x} \frac{\sin(\tilde{k}_x \Delta x / 2)}{\sin(\omega \Delta t / 2)} \tag{4-36}$$

$$E_{z_0} \sin\frac{\omega \Delta t}{2} = \frac{\Delta t}{\varepsilon}\left(\frac{H_{x_0}}{\Delta y} \sin\frac{\tilde{k}_y \Delta y}{2} - \frac{H_{y_0}}{\Delta x} \sin\frac{\tilde{k}_x \Delta x}{2} \right) \tag{4-37}$$

Substitute H_{xo} and H_{yo} in (4-37) with (4-35) (4-36) and then yields the following numerical dispersion relation:

$$\left(\frac{1}{c\Delta t} \sin\frac{\omega \Delta t}{2} \right)^2 = \left(\frac{1}{\Delta x} \sin\frac{\tilde{k}_x \Delta x}{2} \right)^2 + \left(\frac{1}{\Delta y} \sin\frac{\tilde{k}_y \Delta y}{2} \right)^2 \tag{4-38}$$

When Δt, Δx and Δy are 0, the above numerical dispersion relation is equal to the dispersion relation in real space and time. However, for real situation, the increment of space and time cannot be 0; therefore the error between numerical dispersion and real dispersion exists. The comparison between numerical dispersion with different cell size and real dispersion is shown in Figure 4-3, where

S= c Δt/Δ

N_λ= c Δt/Δ

From Figure 4-3, to maintain accurate phase velocity, the space cell size should be no more than 1/10 λ_0.

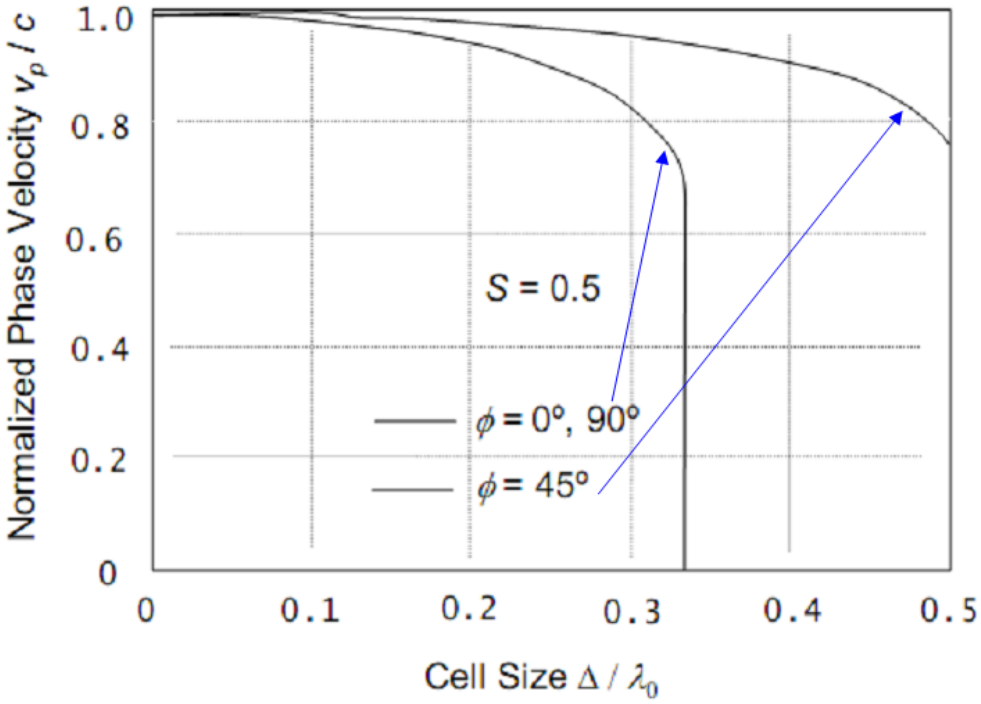

Figure 4-3. Phase velocity v.s. cell size [34].

Numerical Stability

Yee's algorithm for Maxwell's curl equations requires that Δt must be bounded relative to space increments to avoid numerical instability. The complete derivation of the stability condition can be found in Yee's paper [32]. In this paper, for the FDTD analysis based on central differencing, to maintain the numerical stability, the following inequity must be met:

$$\Delta t \leq c\sqrt{\frac{1}{(\Delta x)^2}+\frac{1}{(\Delta y)^2}+\frac{1}{(\Delta z)^2}} \tag{4-39}$$

Where c is the velocity of light in free space. This equation is known as Courant-Freidrichs-Levy (CFL) Stability Criterion. For unstable condition, the computed E and H fields will increase boundlessly as time progresses.

FDTD for Dispersive Materials

In previous section, FDTD for non-dispersive material is introduced for the understanding of its basic algorithm. In this session, FDTD for dispersive material will be described for the simulation of plasmonic devices, which is a kind of metamaterials with extra-ordinary physics properties such as negative refractive index and phase velocity.

Metamaterials are characterized in terms of their effective material parameters like electric permittivity and magnetic permeability. The value of these parameters can

be either positive or negative. Figure 4-4 show the classification of materials, materials fall in the first quadrant are DPS (Double Positive) materials, materials fall in the second quadrant are ENG (Epsilon Negative) materials, materials fall in the third quadrant are DNG (Double Negative) materials (or Left-Handed Materials) and materials fall in the fourth quadrant are MNG (Mu Negative) materials. Except for DPS materials, ENG, DNG and MNG are usually regarded as metamaterials. In this dissertation, ENG materials are studied since metals for plasmonic devices are regarded as ENG materials.

There are several schemes have been proposed to include frequency dispersion into FDTD methods: the auxiliary differential equations (ADE) [35], the recursive convolution method (RC) [36], and the z-transform (ZT) method [37]. For simplicity, ADE method is adopted in this dissertation for the simulation of plasmonic devices.

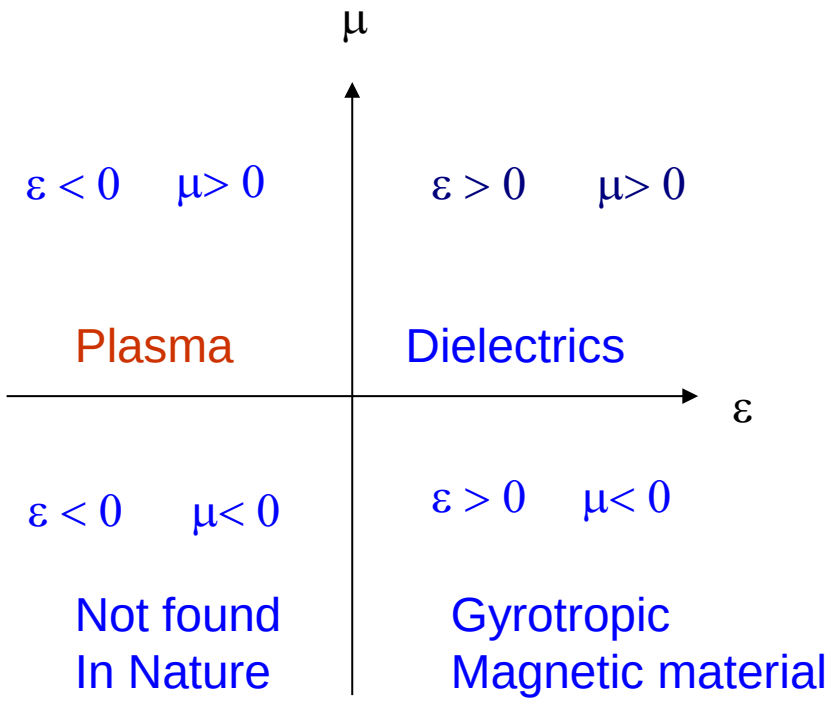

Figure 4-4. Classification of materials.

For dispersive media, the permittivity or permeability is a function of frequency and therefore the electric or magnetic flux density is a function of frequency as well. This relation constitutes the government equations of ADE method.

Now, consider the interaction between TE incident wave (E_z, H_x and H_y) and left-handed media; the involved equations for 2D FDTD formulation with material dispersion are:

$$\frac{\partial D_z}{\partial t} = \frac{\partial H_y}{\partial x} - \frac{\partial H_x}{\partial y} \tag{4-40}$$

$$D_z = \varepsilon_0(1 - \frac{\omega_{ep}^2}{\omega^2 - j\omega\tau_e})E_z \tag{4-41}$$

$$\frac{\partial B_x}{\partial t} = -\frac{\partial E_z}{\partial y} \tag{4-42}$$

$$B_x = \mu_0(1 - \frac{\omega_{em}^2}{\omega^2 - j\omega\tau m})H_x \tag{4-43}$$

$$\frac{\partial B_y}{\partial t} = \frac{\partial E_z}{\partial x} \tag{4-44}$$

$$B_y = \mu_0(1 - \frac{\omega_{em}^2}{\omega^2 - j\omega\tau m})H_y \tag{4-45}$$

The representation of symbols shown in above equations are listed in Table 4-1. In frequency domain, the multiplication of $j\omega$ stands for time derivation in time domain.

Therefore, (4-41) (4-43) and (4-45) in time domain are:

$$\frac{\partial^2 D_z}{\partial t^2} + \tau_e \frac{\partial D_z}{\partial t} = \varepsilon_0 \frac{\partial^2 E_z}{\partial t^2} + \varepsilon_0 \tau_e \frac{\partial E_z}{\partial t} + \varepsilon_0 \omega_{ep}^2 E_z \tag{4-46}$$

$$\frac{\partial^2 B_x}{\partial t^2} + \tau_m \frac{\partial B_x}{\partial t} = \mu_0 \frac{\partial^2 H_x}{\partial t^2} + \mu_0 \tau_m \frac{\partial H_x}{\partial t} + \varepsilon_0 \omega_{ep}^2 H_x \tag{4-47}$$

$$\frac{\partial^2 B_y}{\partial t^2} + \tau_m \frac{\partial B_y}{\partial t} = \mu_0 \frac{\partial^2 H_y}{\partial t^2} + \mu_0 \tau_m \frac{\partial H_y}{\partial t} + \varepsilon_0 \omega_{mp}^2 H_y \tag{4-48}$$

By applying central difference (4-40), (4-42) and (4-44) are discretized into

$$D_z^{n+1}(i + 1/2, j + 1/2) = D_z^n(i + 1/2, j + 1/2) + \Delta t[\frac{H_y^{n+1/2}(i+1,j+1/2) - H_y^{n+1/2}(i,j+1/2)}{\Delta x} - \frac{H_x^{n+1/2}(i+1,j+1/2) - H_x^{n+1/2}(i,j+1/2)}{\Delta y}] \tag{4-49}$$

$$B_x^{n+3/2}(i+1/2,j+1) = B_x^{n+1/2}(i+1/2,j+1) - \Delta t[\frac{E_z^{n+1}(i+1/2,j+3/2) - E_z^{n+1}(i+1/2,j+1/2)}{\Delta y}] \quad (4\text{-}50)$$

$$B_y^{n+3/2}(i+1,j+1/2) = B_y^{n+1/2}(i+1,j+1/2) - \Delta t[\frac{E_z^{n+1}(i+3/2,j+1/2) - E_z^{n+1}(i+1/2,j+1/2)}{\Delta x} \quad (4\text{-}51)$$

The first and second order derivation with respect to time in Equation (4-46) to (4-48) can be approximated by second-order accurate central difference shown as follows:

$$\frac{\partial F^n}{\partial t^2} = \frac{F^{n+1} - 2F^n + F^{n-1}}{dt^2} \quad (4\text{-}52)$$

$$F^n = \frac{F^{n+1} - + F^{n-1}}{2\,dt} \quad (4\text{-}53)$$

The fields located at time point t=n Δt are approximated by a semi-implicit scheme:

$$F^n = \frac{F^{n+1} + 2F^n + F^{n-1}}{4} \quad (4\text{-}54)$$

By applying (4-52) to (4-54) into (4-46) to (4-48), the explicit update equations are written as follow:

$$E_z^{n+1}(i+1/2,j+1/2) = \sum_{i=-1}^{1} a_i D_z^{n+i}(i+1/2,j+1/2) - \sum_{i=-1}^{0} b_i E_z^{n+i}(i+1/2,j+1/2) \quad (4\text{-}55)$$

Where M=2 and

$$a_1 = \frac{4+2\tau_e\Delta t}{A_1} \quad a_0 = \frac{-8}{A_1} \quad a_{-1} = \frac{4-2\tau_e\Delta t}{A_1};$$

$$b_0 = \frac{-8\varepsilon_0 + 2\varepsilon_0\Delta t^2\omega_{ep}^2}{A_1} \quad b_{-1} = \frac{4\varepsilon_0 - 2\varepsilon_0\tau_e\Delta t + \varepsilon_0\Delta t^2\omega_{ep}^2}{A_1}$$

$$A_1 = 4\varepsilon_0 + 2\varepsilon_0\tau_e\Delta t + \varepsilon_0\Delta t^2\omega_{ep}^2$$

$$H_x^{n+3/2}(i+1/2,j+1) = \sum_{i=-1}^{1} c_i B_x^{n+i+1/2}(i+1/2,j+1) - \sum_{i=-1}^{0} d_i B_x^{n+i+1/2}(i+1/2,j+1) \quad (4\text{-}56)$$

$$H_y^{n+3/2}(i+1,j+1/2) = \sum_{i=-1}^{1} c_i B_y^{n+i+1/2}(i+1,j+1/2) - \sum_{i=-1}^{0} d_i B_y^{n+i+1/2}(i+1,j+1/2) \quad (4\text{-}57)$$

Where M=2 and

$$c_1 = \frac{4+2\tau_m\Delta t}{A_2} \quad a_0 = \frac{-8}{A_2} \quad a_{-1} = \frac{4-2\tau_m\Delta t}{A_2} \quad d_0 = \frac{-8\mu_0+2\mu_0\Delta t^2\omega_{mp}^2}{A_2}$$

$$d_{-1} = \frac{4\mu_0-2\mu_0\tau_m\Delta t+\mu_0\Delta t^2\omega_{mp}^2}{A_2}$$

$$A_2 = 4\mu_0 + 2\mu_0\tau_m\Delta t + \mu_0\Delta t^2\omega_{mp}^2$$

To implement this FDTD iteration for dispersive media, the procedure shown in Figure 4-5 has to be followed. Based on Figure 4-5, D is updated from H first and then D is converted to E at the same time step; finally H is updated from E and then B is converted to H. This cycle keeps running until the time iteration loop is ended [34].

Get updated D from $\frac{\partial D}{\partial t} = \nabla \times H$

Get updated E from $\frac{\partial^2 D}{\partial t^2} + \gamma \cdot \frac{\partial D}{\partial t} = (\frac{\partial^2 E}{\partial t^2} + \gamma \cdot \frac{\partial E}{\partial t} + \omega_p{}^2) \cdot \varepsilon_o \cdot E$

Get updated H from $\frac{\partial H}{\partial t} = -\frac{1}{\mu} \nabla \times E$

Figure 4-5. FDTD field iteration procedure for dispersive media.

CHAPTER V

SURFACE PLASMON POLARITONS AND PLASMONIC WAVEGUIDES*

Introduction

With the advances of nano fabrication technologies, plasmonic waveguide devices have attracted intensive research interest in recent years mainly due to their strong optical confinement property at the scale that is much smaller than the free space optical wavelength [60]-[68]. Such field confinement property provides a promising platform for the implementation of nano metallic devices for optical communication applications. Based on this perspective, in this chapter, the properties surface plasmon polaritons and plasmonic devices will be studied for possible applications.

Plasmons, Surface Plasmons and Surface Plasmon Polaritons

In physics, plasmons are the quantization of free electron density wave oscillations embedded in immobile positive irons of metals [69]-[71]. Therefore, as one can expect, surface plasmons (SPs) are those oscillations confined at the the material interface. To be more specific, the interface between two materials with opposite sign of

---

of the dielectric index across the interface (e.g. metal sheet in air).

When a SPs couple with photons, the resulting quasiparticles are called surface plasmon polaritons (SPPs). From the point of view of classical electromagnetic wave, SPP can be regarded as a kind of surface waves with exponential decayed fields, as shown in Figure 5-1, around the confining surface and can propagate along the metal-dielectric surface until energy is lost either via absorption in the metal or radiation into free-space. This surface-wave like property has attained a great attention among optics societies in recent years for its capability to shrink the size of optical devices. Therefore, in this dissertation, we will mainly focus on the surface wave property of SPPs for its application in the study.

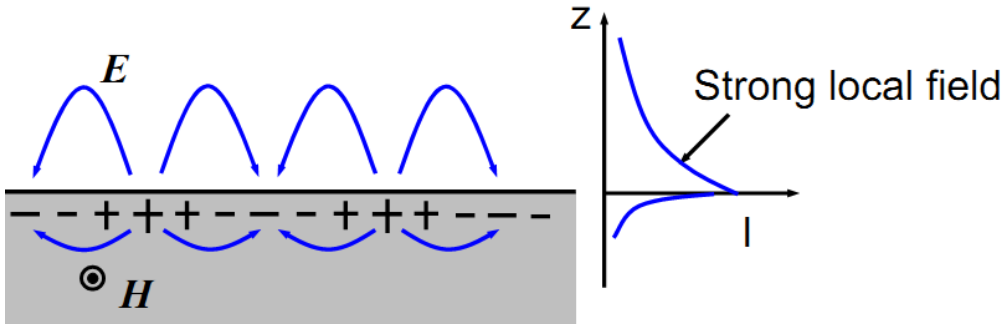

Figure 5-1. Field distribution of SPPs at metal-dielectric interface.

Lorenz Model -Light-Matter Interaction

The interaction of the electromagnetic wave and the electrons in materials can be modeled by Lorenz model [72]. This model describes the electron motion in terms of a driven, damped and harmonic oscillator, as shown in Figure 5-2. As one can see in Figure 5-2, an electron and a nucleus are attached to a spring. Therefore, the incident electric field induces displacement to the electron that is under the influence of a spring-like restoring force due to the nucleus.

The motion of the electron can be express by the following equation:

$$\frac{d^2x(t)}{dt^2} + \gamma\frac{dx(t)}{dt} + \omega_0{}^2 x = \frac{-e}{m}E(t) \tag{5-1}$$

Where x is the electron displacement, γ is the damping constant, ω_o is the resonant frequency, m is the mass of the electron and e is the electron charge.

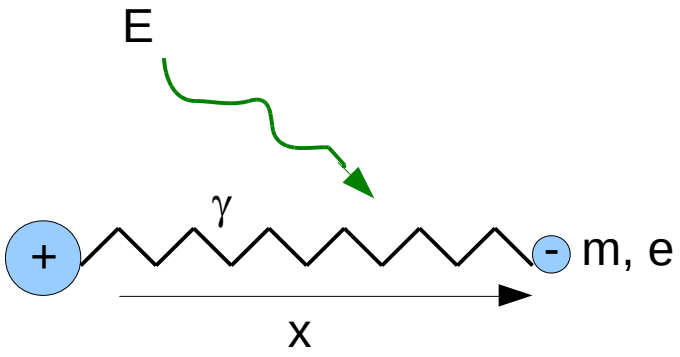

Figure 5-2. Lorenz model.

In equation (5-1), the first left term corresponds to the acceleration of the charges, the second term corresponds to the damping mechanisms of the system, the third term corresponds to the restoring force and the last term corresponds to the driven force form the external electric field.

Since equation (5-1) is a typical linear differential equation and *E(t)* as well as the solution x*(t)* are of the form:

$$E(t)=E\, e^{(i\omega t)} \tag{5-2}$$

$$x(t)=A\, e^{(i\omega t)} \tag{5-3}$$

By taking Fourier transform at both sides of equation (5-1), the following equation for frequency domain can be obtained:

$$-\omega^2 x(\omega)+i\gamma\omega x(\omega)+\omega_0{}^2 x(\omega)=-\frac{e}{m}E(\omega) \tag{5-4}$$

Rewrite the above equation, the electron displacement is expressed as

$$x(\omega)=\frac{\frac{e}{m}E(\omega)}{\omega^2-i\gamma\omega-\omega_0{}^2} \tag{5-5}$$

The dipole moment for the electron displacement is

$$\mathbf{p}(\omega)=-e\cdot\mathbf{x}(\omega) \tag{5-6}$$

For materials with N dipoles in a volume, the whole induced dipole moment is

$$P(\omega)=\frac{Ne^2}{m}\cdot\frac{E(\omega)}{\omega_0{}^2+i\gamma\omega-\omega^2} \tag{5-7}$$

And

$$\mathbf{P} = \varepsilon_0 \chi \mathbf{E}$$
$$\chi = \varepsilon_r - 1 = n^2 - 1 \tag{5-8}$$

Where χ is the dielectric susceptibility. Therefore,

$$\varepsilon_r(\omega) - 1 = \frac{Ne^2}{m\varepsilon_0} \cdot \frac{1}{\omega_0^2 - \omega^2 + i\gamma\omega} \tag{5-9}$$

Here, $Ne^2/m\varepsilon_o$ stands for the plasma frequency, ω_p.

Equation (5-9) is Lorenz model for the dielectric susceptibility, which is essential for the analysis of surface plasmon polaritons. When the acceleration term is small, that is, $\omega^2 \rightarrow 0$, and Lorenz model can be reduced to Debye model; when the restoring force is negligible, $\omega_o^2 \rightarrow 0$, Lorenz model can be reduced to Drude model.

Figure 5-3 and Figure 5-4 shows the real part and imaginary part of permittivity of gold respectively based on Drude model. For gold (Au), the plasma frequency is $13.72*10^{15}$ (rad/s) and the damping frequency is $4.05*10^{13}$ (rad/s). According to Figure 5-3 and Figure 5-4, for wavelength 1550nm (f =1.935 * 10^5), the permittivity of gold is ε_r= -126+4.2i of which the real part is negative. Therefore, gold can be considered as a metamaterial (ENG) under this circumstance.

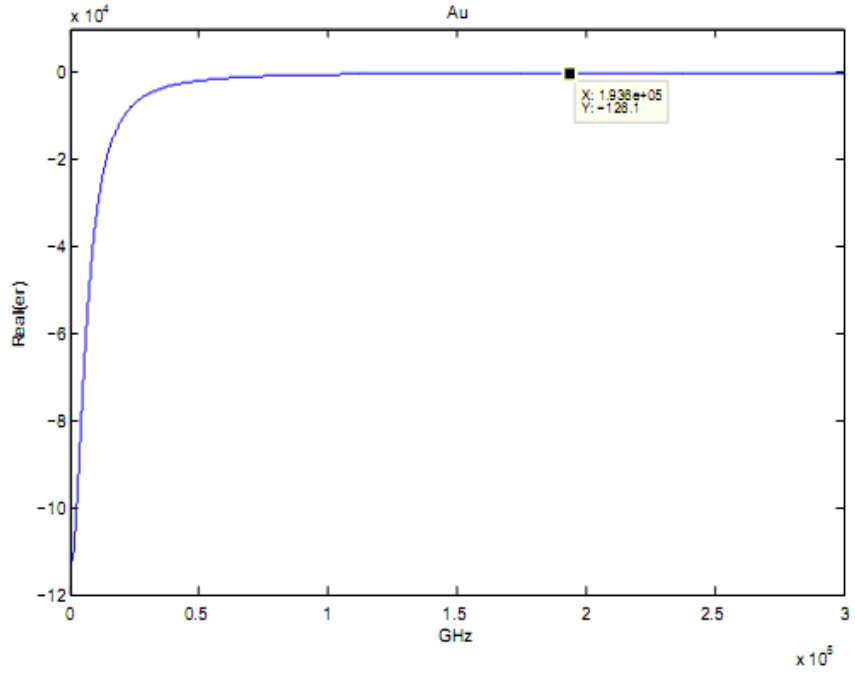

Figure 5-3. Real part of permittivity of gold.

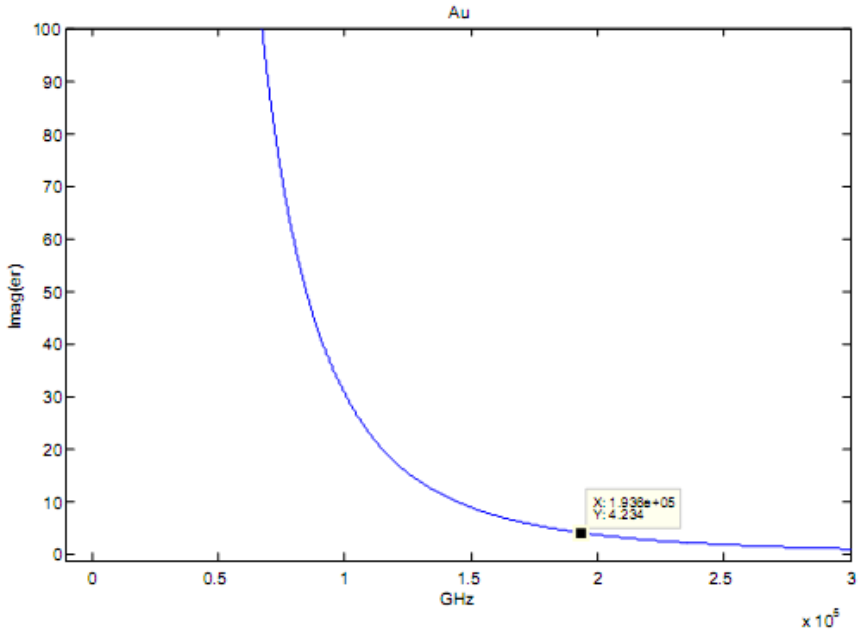

Figure 5-4. Imaginary part of permittivity of gold.

Surface Plasmon-Polariton at Single Surface

Here we study the dispersion relation of surface plasmon polaritons with the TM polarized incident wave at a single flat metal-dielectric interface, as shown in Figure 5-5.

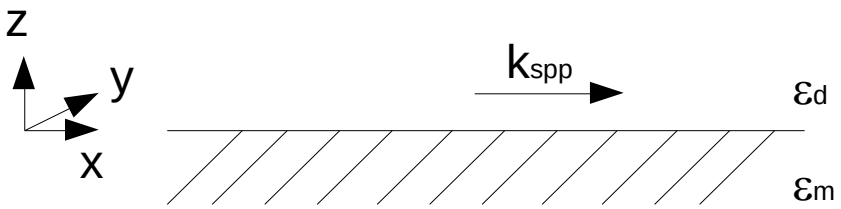

Figure 5-5. TM incident wave hits the single metal-dielectric interface.

Consider an incident TM polarized filed from dielectric with field component H_y, E_x and E_y. At steady state, which means the state that the TM polarized field couples to the surface plasmon polaritons (SPPs), the field components of SPP in the dielectric region are expressed as:

$$\begin{aligned} H^d(x;t) &= (0, A, 0)\exp(ik_{spp}x - k_z^d z - i\omega t) \\ E^d(x;t) &= -A\frac{c}{i\omega\varepsilon_d}(k_z^d, 0, ik_{spp})\exp(ik_{spp}x - k_z^d z - i\omega t) \end{aligned} \quad (5\text{-}10)$$

Where (0, A,0) stands for the field amplitude in x, y and z direction respectively, A is the incident field amplitude, k_{spp} is the propagation constant of the surface plasmon polariton, k_z is the SPP wave vector in z direction, ε_d is the dielectric constant and ω is the wave angular frequency. Similarly, the field components in the metal region are expressed as:

$$H^m(x;t) = (0,B,0)\exp(ik_{spp}x - k_z^m z - i\omega t)$$
$$E^m(x;t) = -B\frac{c}{i\omega\epsilon(\omega)}(-k_z^m, 0, ik_{spp})\exp(ik_{spp}x - k_z^m z - i\omega t) \quad (5\text{-}11)$$

Based on the boundary condition, at the interface, the normal electric flux density D, tangential H and tangential E field should be continuous [73]. Therefore, the following relations can be obtained:

$$(k_z^d)^2 = k_{spp}^2 - \varepsilon_d(\frac{\omega}{c})^2$$
$$(k_z^m)^2 = k_{spp}^2 - \varepsilon(\omega)(\frac{\omega}{c})^2$$

$$\frac{k_z^m}{k_z^d} = -\frac{\varepsilon(\omega)}{\varepsilon_d} \quad (5\text{-}12)$$

According to the above three equations, k_{spp} is solved and expressed as:

$$k_{spp} = \frac{\omega}{c}\left[\frac{\varepsilon_d\varepsilon(\omega)}{\varepsilon_d+\varepsilon(\omega)}\right]^{1/2} \quad (5\text{-}13)$$

Figure 5-6 (a) and Figure 5-6 (b) shows the H field distribution and the SPP dispersion curve of at a single gold-air interface based on Equation (5-13). From the dispersion curve for SPP, it is known that k_{spp} is larger than light line, which means the wave vector in z direction is imaginary. Therefore, fields of SPPs decay exponentially away from the material interface that enables the sub-wavelength confinement.

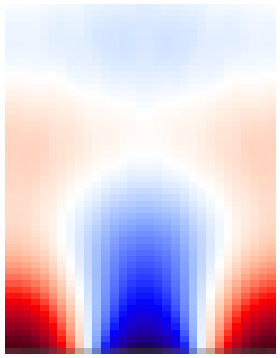

Au

Figure 5-6 (a). H_z field of SPPs at gold-air interface (FDTD).

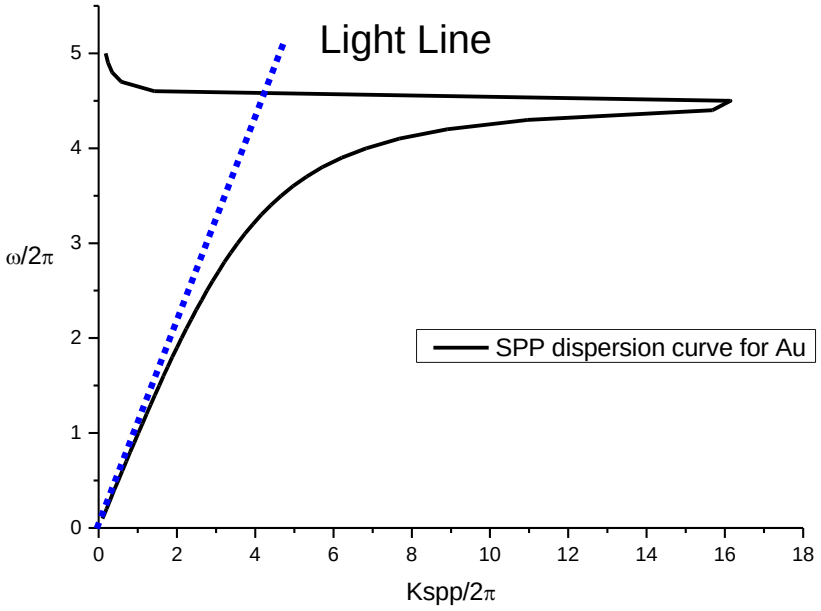

Figure 5-6 (b). SPP dispersion curve for gold.

Surface Plasmon-Polariton in Metal-Dielectric-Metal Structure

Now we study the wave guidance property of the metal-dielectric-metal structure shown in Figure 5-7. As what has been derived in last section, it is known that the fields of SPPs decay exponentially at the metal-dielectric interface. This is also true for the metal-dielectric-metal case. Therefore, the procedure to obtain the field solution for SPPs in this structure is basically the same as that for single metal-dielectric surface [74], [72], [75].

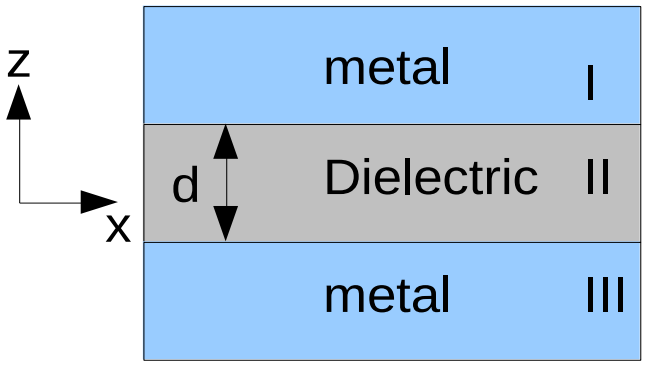

Figure 5-7. The metal-dielectric-metal structure.

The format of TM mode field distribution for SPPs in the structure shown in Figure 5-7 for region I, region II and region III are defined as followed:

For region I, z>d/2:

$$H_{y1} = H_d\, e^{\kappa 1 (z - d/2)}\, e^{-jk_x x} \tag{5-14}$$

$$E_{x1} = -\kappa_1 / j\omega\varepsilon_1\, H_d\, e^{\kappa 1 (z - d/2)}\, e^{-jk_x x} \tag{5-15}$$

$$E_{z1}=-k_x/j\omega\varepsilon_1 \, H_d \, e^{\kappa 1 (z - d/2)} \, e^{-jk_x x} \quad (5\text{-}16)$$

For region II, d/2>z>0:

$$H_{y2}= H_m \cosh(\kappa_2 z) \, e^{-jk_x x} \quad (5\text{-}17)$$

$$E_{x2}= -\kappa_2/j\omega\varepsilon_2 \, H_d \sinh(\kappa_2 z) \, e^{-jk_x x} \quad (5\text{-}18)$$

$$E_{z2}=-k_x/j\omega\varepsilon_2 \, H_d \cosh(\kappa_2 z) \, e^{-jk_x x} \quad (5\text{-}19)$$

For region III, z<-d/2:

$$H_{y3}= H_d \, e^{\kappa 1 (z + d/2)} \, e^{-jk_x x} \quad (5\text{-}20)$$

$$E_{x3}= -\kappa_1/j\omega\varepsilon_1 \, H_d \, e^{\kappa 1 (z + d/2)} \, e^{-jk_x x} \quad (5\text{-}21)$$

$$E_{z3}=-k_x/j\omega\varepsilon_1 \, H_d \, e^{\kappa 1 (z + d/2)} \, e^{-jk_x x} \quad (5\text{-}22)$$

Where H_m is the field amplitude, ε_2 is the permittivity of the metal, ε_1 is the permittivity of the dielectric, $\kappa_1= (k^2_x - \omega^2 \mu \, \varepsilon_1)^{1/2}$ and $\kappa_2= (k^2_x - \omega^2 \mu \, \varepsilon_2)^{1/2}$.

Based on the boundary condition, the tangential E, H fields and normal electric flux density are continuous at the interface and the following relations can be obtained:

$$H_d = H_m \cosh(\kappa_2 d/2) \quad (5\text{-}23)$$

$$-\kappa_1 H_d/\varepsilon_1= \kappa_2/\varepsilon_2 \, H_m \sinh(\kappa_2 d/2) \quad (5\text{-}24)$$

Hence the dispersion relation is:

$$\tanh(\kappa_2 d/2)= - \kappa_1\varepsilon_2/\kappa_2\varepsilon_1 \quad (5\text{-}25)$$

Based on the above transcendental equation, the mode of SPPs can be solved. Figure 5-8 shows the effective index of plasmonic TM_o mode (fundamental mode) v.s. the thickness of the dielectric slab. One can see that as the slab thickness becomes smaller, the effective index becomes larger, which means the fields at the interface decay rapidly

with smaller slab thickness. This is why the plasmonic waveguide can guide waves in nano scale that is much smaller than the signal wavelength. Also, according to the transcendental equation, there is no cut-off frequency for plasmonc TM_o mode operating below surface plasmon frequency, as shown in Figure 5-7. Therefore, plasmonic waveguide can also provide wide band operation.

Plasmonic Waveguide Coupler

Among all the required new technologies, efficient light coupling is one of the important issues for the design of plasmonic gap waveguides. Since the effective index of TM_0 plasmonic mode is higher than the material indices of the waveguiding structure, the efficient coupling from waveguide mode to plasmonic mode becomes more difficult, especially when the effective mode index difference between the conventional waveguide mode and the plasmonic mode is large (i.e. mode mismatch).

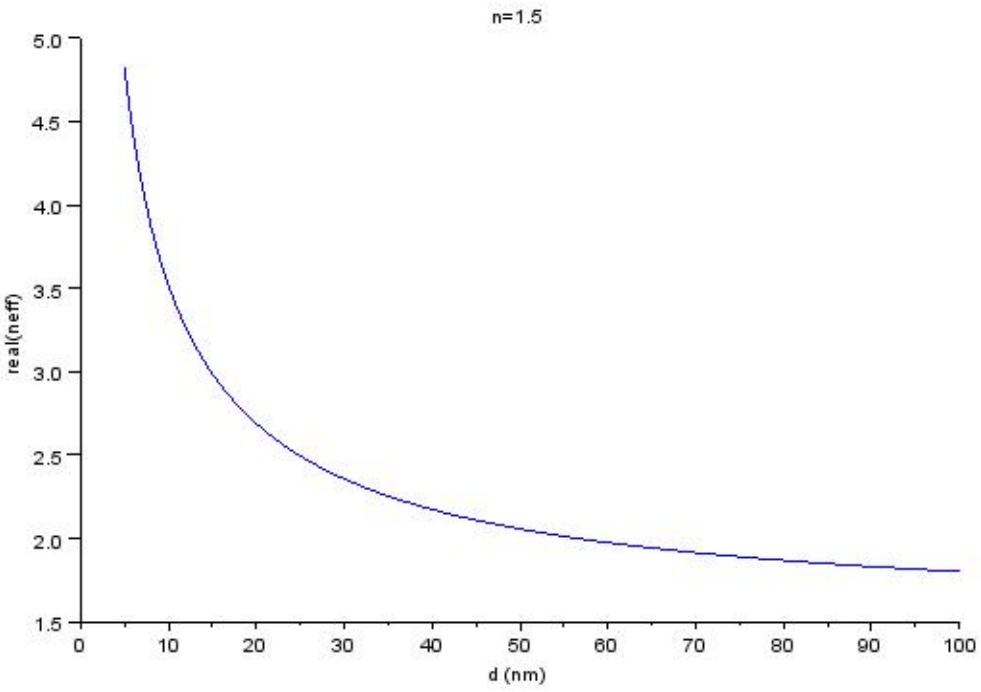

Figure 5-8. The effective index of plasmonic TMo mode v.s. the thickness of the dielectric slab.

So far, there are a couple literatures discussing the excitation of the non-silicon filled plasmonic gap waveguide mode by using a plasmonic gap taper [38], a nano-antenna [39], a multi-section coupler [40] and a silicon slot waveguide [41]. However, none of these structures are aimed at the mode coupling of silicon filled plasmonic gap waveguides.

To distinguish the complexity between silicon- based and silica-based plasmonic gap waveguide coupling via a slab waveguide, the effective mode index n_{eff} versus the waveguide width of the slab fundamental TM mode, the plasmonic TM_0 mode and the plasmonic TM_2 mode are plotted in Figure 5-9(a) and (b) for the silicon-based case and the silica-based case respectively.

According to [38], due to the structure symmetry of the considered problem, the symmetry nature of the modes plays an important role here for mode coupling. Since the excitation mode (the slab fundamental TM mode) is an even TM mode, only its nearby even plasmonic TM modes, plasmonic TM_0 and TM_2, will be excited. Therefore, we just need to consider the mode coupling between the slab fundamental TM mode and plasmonic TM_2 modes. This symmetry property can also be verified from H_z field profiles along y axis shown in Figure 5-9(c) and (d).

As shown in Figure 5-9(a) and (c), one can see that most power of the fundamental TM mode of the silicon micro-slab will be coupled into the plasmonic TM_2 mode rather than the plasmonic TM_0 mode because of the presence of the closer plasmonic TM_2 mode and the larger effective index difference between the slab fundamental TM mode and plasmonic TM_0 mode. On the contrary, from Figure 5-9(b)

and (d), one can observe that the fundamental TM mode of the silica micro-slab is easier to be coupled into the plasmonic TM_0 mode than the plasmonic TM_2 mode as the effective index of the slab fundamental is closer to that of plasmonic TM_0 mode. This is why the high efficiency conversion between the fundamental TM mode of a micron/sub-micron silicon slab and the plasmonic TM_0 mode of a plasmonic gap waveguide is challenging in order to directly integrate the slab waveguide with the light source from an optical fiber or an on-chip laser for efficient light coupling.

In the microwave regime, corrugated metal structures have long been proposed and utilized as waveguide mode converters between conventional guided modes [42], surface wave assisted structures [43], slow-wave structures [44] or filters [45]. In recent years, they draw attentions again in the emergent researches on slow-light and THz applications [46], for similar purposes such as dispersion controlling [47] and the so called spoof or designer surface plasmon assisted structures operating at low THz frequencies [48], [49], [50], which are actually surface waves existing on inductive corrugated surfaces formed by perfect electrical conductors (PEC) described in Electromagnetics books [43], [44].

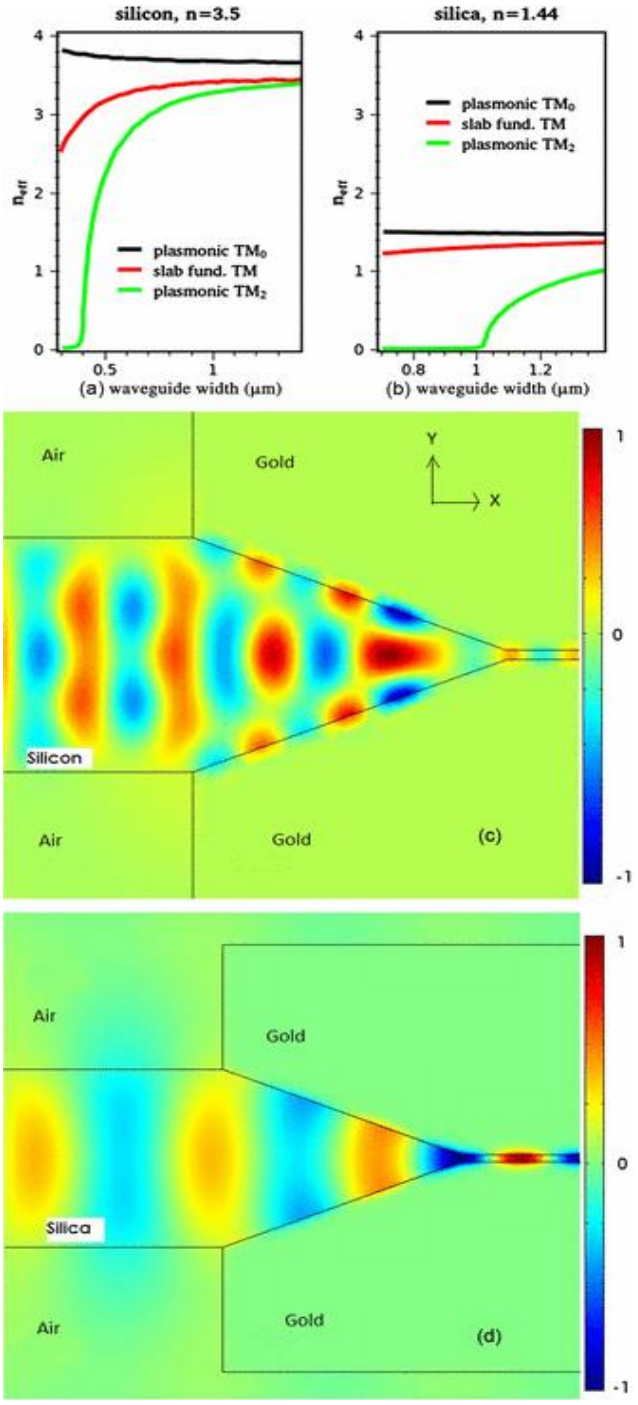

Figure 5-9. Effective mode indices of plasmonic TMo(black), slab fundamental TM (red) and plasmonic TM_2 (green) modes for (a) silicon and (b) silica based slab waveguides and plasmonic gap waveguides. The Hz field coupling from a 1.25 μm slab waveguide to 50 nm plasmonic gap waveguide with a 1.5 μm taper for: (c) silicon based waveguides and (d) silica based waveguides.

Recently, grooved metal sidewalls [54] (or another name, corrugated horn structure [55]) with 6.2 μm input opening for metal-silicon-metal plasmonic gap waveguide coupling is reported with maximum 72% coupling efficiency. The coupling is achieved by exciting SPPs (Surface Plasmon Polaritons) at metal surfaces [55] with TM polarized light thus the groove number will affect the transmission efficiency dramatically (Figure 2 in [54]). In addition, the structure requires that (1) SPPs generated by adjacent grooves are in phase and (2) the incident lights falling on each groove are in phase for higher coupling efficiency. Therefore the corrugated metal surfaces have to be tapered at a specific angle (58^o in [54], [55]) and the groove distance has to be kept at $2\lambda_{spp}$ once the metal material is decided. These restrictions may somehow constrain the coupler design freedom by that approach.

Unlike open corrugated structures [48], [49], [50], [52], the waveguide dispersion of a corrugate waveguide (a closed structure), as shown in Figure 5-10(a), can extend across the light line [42], [44], [47], [51], [53]. This in principle can be utilized in the coupler design to transform the waveguide guided mode ($\beta<k$) across the light line to match the plasmonic mode with $\beta>k$. Here k is the wave number for the dielectric sandwiched between the grooved metal plates. As mentioned above, a corrugated metallic waveguide is known to be able to serve as a mode converter [42] between conventional guided modes due to its dispersion engineerable structure and low attenuation characteristics [51] at the microwave frequency. However, there is still no literature discussing the use of corrugated waveguide for optical guided mode to plasmonic mode coupling. In addition, at the optical frequency, metal is no longer a

perfect conductor and the signal propagation loss is considerable especially when the corrugated metal structure is incorporated in the design. Therefore, whether a metallic corrugated coupler with high coupling efficiency is feasible for conventional guided mode to plasmonic mode conversion at the optical regime still requires further investigation, which is the main objective of the present work.

In this section, a short (~1.5μm) gold partially corrugated tapered waveguide for mode coupling enhancement at the 1550 nm optical communication wavelength between a 1.25 μm silicon micro-slab and a plasmonic nano-gap waveguide is designed and analyzed for the first time. The coupling efficiency is examined to be able to reach 86% ~ 98% with the plasmonic waveguide gap size ranging from 20 nm to 300 nm, which is comparable to or even higher than that of the previously referred non-silicon and silicon based cases. Finally, for comparison, we also use silver as the metal material in the design for different-size plasmonic gap waveguide coupling. The simulation results show that around 90% coupling efficiency on average can be achieved by using the corrugated tapered waveguide without the need to set the groove distance to be $2\lambda_{spp}$, which directly proves that the coupling mechanism of the corrugated waveguide studied here is different from that of the grooved metal sidewalls [54] or the corrugated horn structure [55]. Figure 5-10 shows a PEC periodic corrugated metallic parallel plate waveguide and its dispersion diagrams [42]. The period of the corrugation, the depth of the tooth, the width of the dielectric tooth, and the vertical distance between metal teeth are represented by p, h, t and g respectively, as depicted in the inset figure. One can see the corrugated waveguide can have modes across the light line [42], [44], [51], [53].

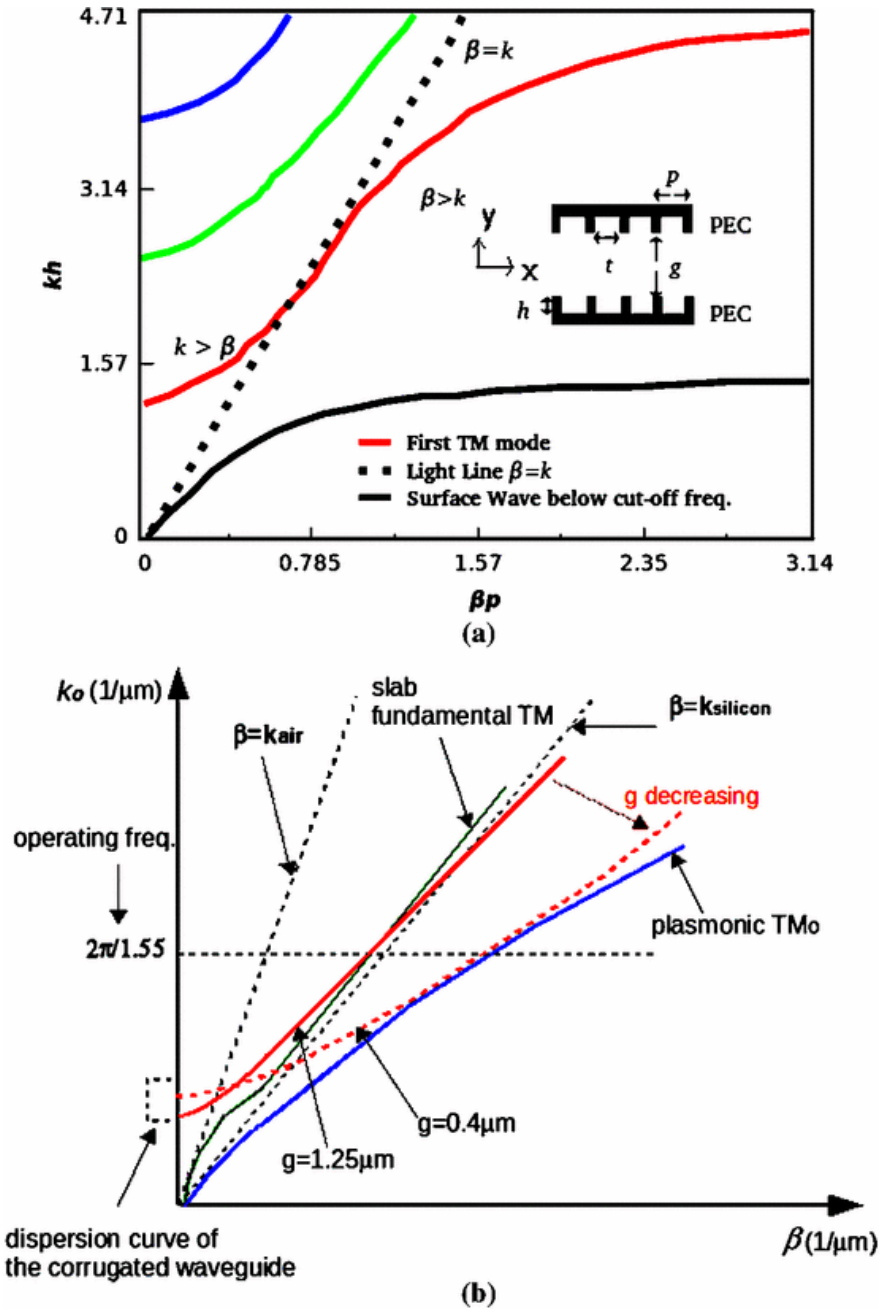

Figure 5-10. (a) Dispersion diagram of a corrugated parallel-plate waveguide. As shown in the red line, the waveguide can have modes with both β>k and β<k. Blue and green lines represent higher order TM modes. (b) Schematic diagram for the design idea.

Although the dispersion curves in Figure 5-10(a) is based on PEC corrugation as a periodic system ($p \sim \lambda_g$) and its dispersion relation is different from PEC corrugation as a uniform systems ($p << \lambda_g$) [44], the relation between waveguide dispersion and the structure parameters (*p*, *h*, *t* and *g*) for these two cases still share the same features.

Figure 5-11 shows the partially corrugated taper for the silicon filled plasmonic gap waveguide coupling. The width of the silicon slab w_1 is set to be 1.25 μm and the gap of the plasmonic metal-silicon-metal waveguide w_2 is set to be 20 nm in Figure 5-11(a), 50 nm in Figure 5-11(b) and 300 nm in Figure 5-11(c) respectively. In the design simulation, the relative permittivity for silicon is ε_{si}=12.25 while the complex relative permittivity of the metal (gold) is ε_{Au}=-93+11*i* determined by the Lorenz-Drude model [56]. The simulation work is done by the commercial 2D Finite Element software, which is also the approach used in [54], [55]. The accuracy of the 2D FEM is compared with the coupling efficiency calculated by 2D FDTD published in [38], which is a silica-based case with 6 μm taper and 50 nm gap. In [38], the calculated coupling efficiency is reported to be ~70% and our result based on 2D FEM simulation is 69.3%. The error is quite small in this case. However, for the silicon-based case, the numerical results generated by the open source FDTD code (MEEP) cannot converge well due to the staircasing approximation [57] introduced at the material interfaces with a large index contrast between the positive real part of the silicon and the negative real part of the metal. In contrast, for FEM, no staircasing approximation is required at the silicon-metal interfaces. Thus the field boundary conditions at the material interfaces can be treated precisely and the meshes in the nano gap can be extremely refined to achieve high

accuracy. Based on the above facts, previous literature [58] and our study [59], FEM should be more suitable than FDTD for plasmonic related problems especially when high material index contrast is involved.

In the design, the corrugation period (p~0.14μm) is comparable to the effective wavelength (λ_g~0.44 μm) of the slab fundamental mode and thus the formulation for the uniform system is not applicable here. In addition, since finite corrugation periods are incorporated in the design, strictly speaking the corrugated taper cannot be considered as a periodic structure. Nevertheless, the dispersion relation for periodic systems still can provide a basic idea to decide the size of *p*, *h* and *t* for the effective mode index of the corrugated waveguide that matches the effective index of the fundamental slab TM mode at the input end with g=1.25 μm and matches the effective index of the plasmonic TM_0 mode with g~= 0.4μm around which the plasmonic TM_2 mode is cut off, as shown in Figure 5-9(a). In the design, *p*, *t* and the taper length are set to be around 0.14 μm, 0.1 μm and 1.5 μm respectively. With given *h* and *g*, β is then estimated by Equation (5-26) [7].

$$\frac{p}{t}\frac{\sqrt{\beta^2-k^2}}{k}\frac{tanh\left(\frac{g}{2}\sqrt{\beta^2-k^2}\right)}{sinc^2\left(\beta\frac{t}{2}\right)}=tan(kh) \tag{5-26}$$

Here, *k* is the wave number for the dielectric sandwiched by the grooved metal plates and the value of h can be slightly optimized for better performance. According to Equation (5-30), for a specific operating frequency (that is, for a specific k_0), β increases as *g* decreases, as shown in Figure 5-10(b). Therefore, as the slab TM mode passes through the corrugated region of the taper, it is transformed gradually into the mode with

$\beta > k$ that can match the plasmonic TM_0 mode ($\beta > k$) at the input of the non-corrugated taper. The reason why the taper is made partially corrugated is that only plasmonic TM_0 mode exists when the metallic gap size drops below ~0.4μm, as illustrated in Figure 5-9(a). Under this situation, the loss will increase when the plasmonic TM_0 mode keeps propagating on corrugated surfaces since the fields of the mode now concentrate more on the metal surfaces.

Based on the FEM simulation, the coupling efficiencies for 20 nm to 300 nm metal-silicon-metal gaps, as shown in Figure 5-11(d), range from ~87% to ~98%, which proves that the corrugated waveguide structure can serve as the waveguide mode converter at the optical frequency with low attenuation as described in [51]. This is because most of the fields in the corrugated part of the taper are still confined at the waveguide center, as shown in Figure 5-11 (a)-(c). This fact directly proves that the coupling mechanism of the corrugated waveguide discussed here is not based on the excitation of SPPs on grooved metal surfaces shown in [54], [55]. Actually, according to [44], as a closed structure, the mode field pattern of the corrugated waveguide shown in Figure 5-10(a) is of the form of hyperbolic sinusoidal functions for both $\beta > k$ and $\beta < k$. This is also true for the structure (closed structure as well) of our design, which supports that the field confined in the corrugated taper is not evanescent wave. This is why the propagation loss is low in the corrugated region of our design.

For the purpose of mechanism and performance comparison, the coupling efficiencies for silver based plasmonic gap waveguides with different gap sizes are provided in Figure 5-12(b). The relative permittivity used here is ε_{Ag} =-143.49+9.52*i* [56], of which the imaginary part is larger than that used in [54]. According to Figure 5-12(b), the overall coupling efficiency is obviously higher than the previous results (Figure 8(a) in [54]). For the 50 nm silver plasmonic gap waveguide shown in Figure 5-12(a), the coupling efficiency is ~93% with 8 grooves, which is also much higher than the result reported in [54] (~50% with 4 grooves). Also note that the groove distance shown in Figure 5-12(a) is 0.15 μm (much smaller than $2\lambda_{spp}$=0.84μm proposed in [54], [55]) and the taper angle here is ~22^o (not 58^o reported in [54], [55]). All facts point out again that the coupling mechanism of the corrugated waveguide reported in this work is different from those by exciting SPPs on metal surfaces depicted in [54], [55].

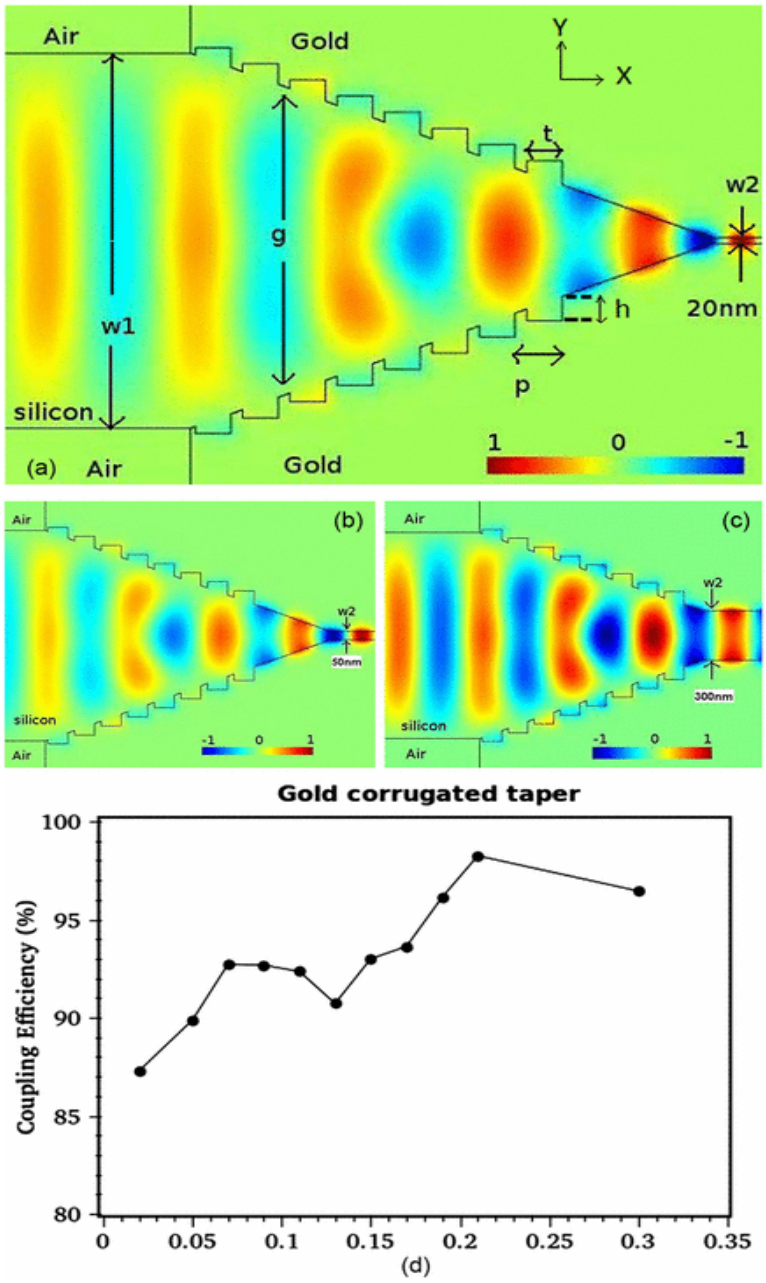

Figure 5-11. 1.25 μm silicon slab to gold plasmonic gap waveguide coupling with the plasmonic waveguide width w_2 = (a) 20 nm, (b) 50 nm and (c) 300nm; the Hz fields are plotted. The coupling efficiencies are ~87%, ~89% and ~96% respectively. (d) Plot of the coupling efficiency versus the plasmonic waveguide gap size.

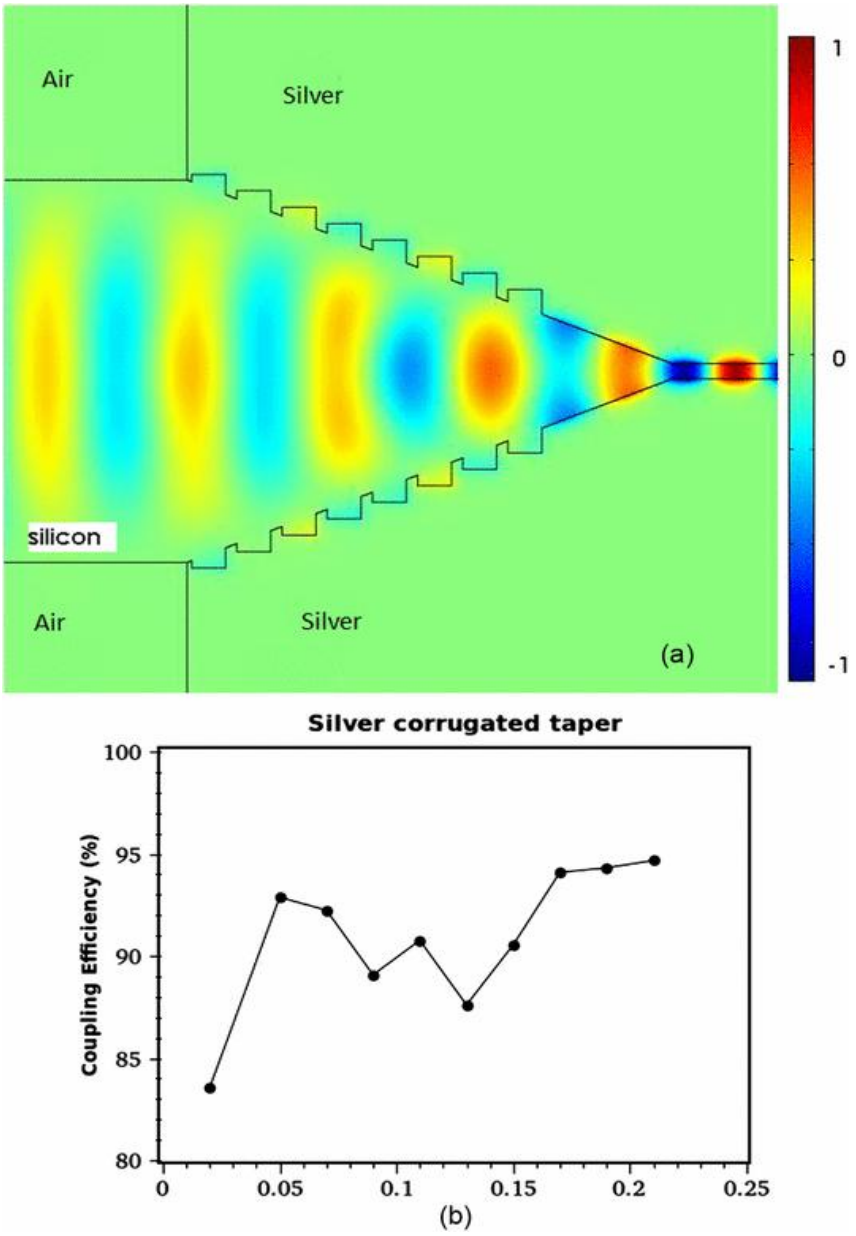

Figure 5-12. (a) 1.25 μm silicon slab to 50 nm silver plasmonic gap waveguide coupling with the same structure configuration shown in Figure 5-11(b). The coupling efficiency is ~93%; the Hz field is plotted. (b) Plot of the coupling efficiency versus the plasmonic waveguide gap size.

Conclusion

In summary, contrasted to [54], [55], the proposed corrugation (with period < λ_{spp}) in the present work is more efficient in coupling light (slab guided mode) into the plasmonic TM_o mode for the silicon-based plasmonic metal-dielectric-metal structures. The high coupling efficiency is achieved through two main key points: (1) excellent mode matching to the plasmonic TM_o mode with $\beta>k$ is made possible by the use of corrugation and (2) the corrugation only introduces very small loss since most of the fields in the corrugated part of the taper are still confined at the waveguide center. Instead, the corrugation (with period $2\lambda_{spp}$) in [54], [55] is used for the excitation of SPPs with TM polarized light (not slab guided mode), which will introduce a larger amount of loss when the SPPs propagate on the grooved metal side walls.

CHAPTER VI

SUMMARY

This dissertation reports the study and design of microwave reconfigurable antenna, ultra wideband band pass filter and optical plasmonic waveguide coupler.
The following achievements are reached:

For the reconfigurable antenna, the idea of a simple frequency reconfigurable patch antenna that operates at multiband from 2 GHz to 4.5 GHz is designed. By changing the position of the microstrip connecting elements on the antenna patches, the operating frequency will shift with fixed radiation patterns.

For the ultra-wideband band pass filter, a compact ultra-wideband (UWB) single-ring band pass filter of 8GHz bandwidth with suppressed sideband and harmonics achieved by forced boundary condition and step impedance filter is proposed. Both measurement and simulated results are shown in good agreement. The group delay variation in the pass-band is measured less than 0.3 ns.

For the plasmonic waveguide coupler, corrugated tapered waveguide for silicon-based micro-slab waveguide to plasmonic nano-gap waveguide mode conversion at the optical communication frequency is devised. High coupling efficiency is demonstrated numerically.

REFERENCES

[1] C. A. Balanis, *Antenna theory: analysis and design*, 3rd ed., New York, NY: J. Wiley, 2005.

[2] J. L. T. Bernhard, *Reconfigurable antennas*, San Rafael, CA: Morgan & Claypool, 2007.

[3] K. Chang, *RF and Microwave Wireless Systems*, 1st ed., New York, NY: J. Wiley, 2000.

[4] D. M. Pozar, *Microwave engineering*, 3rd ed., New York, NY:: J. Wiley, 2005.

[5] D. M. Pozar, "Microstrip Antennas," Proceedings of the IEEE, vol. 80, p. 79, Jan 1992.

[6] J. Zhang, A. Wang and P. Wang, "A survey on reconfigurable antennas," ICMMT, vol. 3, p. 1156, 2008.

[7] S. Nikolaou, R. Bairavasubramanian, C. Lugo, I. Carrasquillo, D. Thompson, G.E. Ponchak, J. Papapolymerou and M.M. Tentzeris, "Pattern and frequency reconfigurable annular slot antenna using PIN diodes," IEEE Trans. Antennas Propag., vol. 54, p. 439, 2006.

[8] G. H. Huff, J. Feng, S. Zhang, and J. T. Bernhard, "A novel radiation pattern and frequency reconfigurable single turn square spiral microstrip antenna," IEEE Microwave and Wireless Components Letters, vol. 13, p. 57, 2000.

[9] C. H. Ho, F. Lu and K. Chang, "Slotline annular ring elements and their applications to resonator, filter and coupler design," Microwave Theory and Techniques, IEEE Transactions on , vol. 41, p. 1648, 1993.

[10] K. Chang and L. H. Hsieh, *Microwave ring circuits and related structures*, 2nd ed., New York, NY: J. Wiley, 2004.

[11] G. Kumar and K. C. Gupta, "Broad-band microstrip antenna using additional resonators gap-coupled to the radiating edges," IEEE Trans Antenna Propag., vol. 32, p. 1375, 1984.

[12] L. H. Hsieh and K. Chang, "Dual-mode quasi-elliptic-function band-pass filters using ring resonators with enhanced-coupling tuning stubs," IEEE Trans Microwave Theory Tech., vol. 50, p. 1340, 2002.

[13] J. S. Hong and M. J. Lancaster, "Bandpass characteristics of new dual-mode microstrip square loop resontors," Electronic Lett., vol. 31, p. 371, 1995.

[14] I. Wolff, "Microstrip bandpass filter using degenerate modes of a microstrip ring resonator," Electronic Lett., vol. 8, p. 302, 1972.

[15] J. S. Hong and M. J. Lancaster, "Microstrip bandpass filter using degenerate mode of a novel meander loop resonator," IEEE Micro-wave Guided Wave Lett., vol. 5, p. 891, 1995.

[16] X. D. Huang and C. H. Cheng, "A novel microstrip dual-dode band-pass filter with harmonic suppression," IEEE Microwave Wireless Comp. Lett., vol. 16, p. 40406, 2006.

[17] C. S. Cho, J. W. Lee, and J. Kim, "Dual- and triple-mode branch-line ring resonators and harmonic suppressed half-ring resonators," IEEE Trans. Microwave Theory Tech., vol. 54, p. 3968, 2006.

[18] L. H. Hsieh and K. Chang, "Slow-wave bandpass filters using ring or stepped-impedance hairpin resonators," IEEE Trans. Microwave Theory Tech., vol. 50, p. 1795, 2002.

[19] L. H. Hsieh and K. Chang, "Tunable microstrip bandpass filters with two transmission zeros," IEEE Trans. Microwave Theory Tech., vol. 51, p. 520, 2003.

[20] L. H. Hsieh and K. Chang, "Compact, low insertion loss, sharp rejection and wideband microstrip bandpass filters," IEEE Trans. Microwave Theory Tech. vol. 51, p. 1241, 2003.

[21] G. K. Gopalakrishnan and K. Chang, "Bandpass characteristics of split-modes in asymmetric ring resonators," Electronic Lett., vol. 26, p. 77475, 1990.

[22] J. Marti and A. Griol, "Harmonic suppressed microstrip multistage coupled ring bandpass filters," Electronic Lett., vol. 34, p. 2140142, 1998.

[23] C. C. Yu and K. Chang, "Novel compact elliptic-function narrow-band bandpass filters using microstrip open-loop resonators with coupled and crossing lines," IEEE Trans. Microwave Theory Tech., vol. 46, p. 952, 1998.

[24] R. S. Kwok and J. F. Liang, "Characterization of high-Q resonators for microwave filter applications," IEEE Trans. Microwave Theory Tech., vol. 51, p. 520, 1999.

[25] K. Chang, *Microwave ring circuits and antennas*, 2nd ed., New York, NY: J. Wiley, 1996.

[26] Zeland Software Inc., IE3D Version 14.0, Zeland Software Inc., Fremont, CA, 2010.

[27] Y. C. Liu, and K. Chang, “Simple wideband microstrip ring band pass filter by utilizing forced harmonic suppression and direct feed-line coupling,” Microw. Opt. Technol. Lett., vol. 54, p. 1968, 2012.

[28] Y. C. Liu and K. Chang, "Compact ultra-wideband single-ring bandpass filter with sideband and harmonic suppression," IEEE Antennas and Propagation Society International Symposium (APSURSI), 2012.

[29] I. Wolff and N. Knoppik, "Microstrip ring resonator and dispersion measurement on microstrip lines," Electronics Lett., vol. 7, p. 779, 1971.

[30] K. Chang, S. Martin, F. Wang and J. L. Klein, "On the Study of Microstrip Ring and Varactor-Tuned Ring Circuits," IEEE Trans. Microwave Theory Tech., vol. 35, p. 1288, 1987.

[31] T. S. Martin, “A study of the microstrip ring resonator and its application,” M.S. thesis, Texas A&M University, College Station, December 1987.

[32] K. S. Yee, “Numerical solution of intitial boundary value problems involving maxwell’s equations in isotropic media," IEEE Transactions on Antennas and Propagation, vol. 14, p. 302, 1966.

[33] Wikipedia, “Finite-difference time-domain method,” 28th December 2013. http://en.wikipedia.org/wiki/Finite-difference_time-domain_method

[34] A. Taflove and S. C. Hagness, *Computational Electrodynamics: The Finite Difference Time Domain Method*, 3rd ed., Norwood, MA: Artech House, 2005.

[35] R. J. Luebbers, F. Hunsberger, K. S. Kunz, R. B. Standler and M. Schneider, “A frequency dependent finite difference time-domain formulation for dispersive materials,” IEEE Transactions on Electromagnetic Compatibility, vol. 32, p. 222, 1990.

[36] O. P. Gandhi, B. Q. Gao and J. Y. Chen, “A frequency-dependent finite difference time domain formulation for general dispersive media,” IEEE Trans. Microwave Theory Tech., vol. 41, p. 658, 1993.

[37] D. M. Sullivan, “Frequency-dependent FDTD methods using z transforms,” IEEE Transactions on Antennas and Propagation, vol. 40, p. 1223, 1992.

[38] P. Ginzburg, D. Arbel and M. Orenstein, "Gap plasmon polariton structure for very efficient microscale to nanoscale interfacing," Opt. Lett., vol. 31, p. 3228, 2006.

[39] J. Wen, S. Romanov and U. Peschel, "Excitation of plasmonic gap waveguides by nanoantennas," Opt. Exp., vol. 17, p. 5925, 2009.

[40] G. Veronis and S. Fan, "Theoretical investigation of compact couplers between dielectric slab waveguides and two-dimensional metal-dielectric-metal plasmonic waveguides," Opt. Exp., vol. 15, p. 1211, 2007.

[41] R. Yang, R. A. Wahsheh , Z. Lu and M. A. G. Abushagur, "Efficient light coupling between dielectric slot waveguide and plasmonic slot waveguide," Opt. Lett., vol. 35, p. 649, 2010.

[42] G. L. James, "Analysis and design of TE-to-HE corrugated cylindrical waveguide mode converters," IEEE Trans. Microwave. Theory Tech., vol. 29, p. 1059, 1981.

[43] R. E. Collin and IEEE Antennas and Propagation Society., *Field theory of guided waves*, 2nd ed., New York, NY: IEEE Press, 1991.

[44] K. Zhang and D. Li, *Electromagnetic theory for microwaves and optoelectronics*, 2nd ed., New York, NY: Springer, 1998.

[45] R. Levy, "Tapered corrugated waveguide low-pass filters," IEEE Trans. Microwave Theory Tech., vol. 21, p. 526, 1973.

[46] Q. Gan , Z. Fu, Y. J. Ding and F. J. Bartoli , "Ultrawide-bandwidth slow-light system based on THz plasmonic graded metallic grating structures," Phys. Rev. Lett., vol. 100, p. 256803, 2008.

[47] A. Brimont, J. Vicente Galán, J. Maria Escalante, J. Mart&iacute and P. Sanchis, "Group-index engineering in silicon corrugated waveguides," Opt. Lett., vol. 35, p. 2708, 2010.

[48] A. I. Fernandez-Dominguez, L. Martin-Moreno, F. J. Garcia-Vidal , S. R. Andrews and S. A. Maier, "Spoof surface plasmon polariton modes propagating along periodically corrugated wires," IEEE J. Sel. Topic Quantum Electron., vol. 14, p. 1515, 2008.

[49] D. Martin-Cano, O. Quevedo-Teruel, E. Moreno, L. Martin-Moreno and F. Garcia-Vidal, "Waveguided spoof surface plasmons with deep-subwavelength lateral confinement," Opt. Lett., vol. 36, p. 4635, 2011.

[50] N. F. Yu, Q. J. Wang, M. A. Kats, J. A. Fan, P. Khanna Suraj, L. Li, A. G. Davies, E. H. Linfield and F. Capasso, "Designer spoof surface plasmon structures collimate terahertz laser beams," Nature Materials, vol. 9, p. 730, 2010.

[51] A. M. B. Al-Hariri, A. D. Olver and P. J. B. Clarricoats, "Low-attenuation properties of corrugated rectangular waveguide," Electron. Lett., vol. 10, p. 304, 1974.

[52] M. Y. Chen and H. C. Chang, "Determination of surface plasmon modes and guided modes supported by periodic subwavelength slits on metals using a finite-difference frequency-domain method based eigenvalue algorithm," J. Lightw. Technol., vol. 30, p. 76, 2012.

[53] G. H. Bryant, "Propagation in corrugated waveguides," Proc. Inst. Elect. Eng., vol. 116, p. 203, 1969.

[54] R. Thomas, Z. Ikonic and R. Kelsall, "Silicon based plasmonic coupler," Opt. Exp., vol. 20, p. 21520, 2012.

[55] G. Y. Li, C. Lin, X. Feng and A. S. Xu, "Plasmonic corrugated horn structure for optical transmission enhancement," Chin. Phys. Lett., vol. 26, p. 124205, 2009.

[56] A. D. Rakic, A. B. Djurisic, J. M. Elazar and M. L. Majewski, "Optical properties of metallic films for vertical-cavity optoelectronic devices," Appl. Opt., vol. 37, p. 5271, 1998.

[57] A. Mohammadi and M. Agio, "Dispersive contour-path finite-difference time-domain algorithm for modeling surface plasmon polaritons at flat interfaces," Opt. Express, vol. 14, p. 11330, 2006.

[58] G. Kewes, A. W. Schell, R. Henze, R. S. Schonfeld, S. Burger, K. Busch and O. Benson, "Design and numerical optimization of an easy-to-fabricate photon-to-plasmon coupler for quantum plasmonics," Appl. Phys. Lett., vol. 102, p. 051104, 2013.

[59] Y. Liu and K. Chang, "Nano-Optical Device Design With the Use of Open-Source Parallel Version FDTD and Commercial Finite Element Package," IEEE International Conference on eScience, Chicago, 2012.

[60] I. V. Novikov and A. A. Maradudin, "Channel polaritons," Phys. Rev. B, vol. 66, p. 035403, 2002.

[61] S. I. Bozhevolnyi, V. S. Volkovel, E. Devaux, J. Y. Laluet and T. W. Ebbesen, "Channel plasmon subwavelength waveguide components including interferometers and ring resonators," Nature, vol. 440, p. 508, 2006.

[62] E. Moreno, F. J. Garica-Vidal, S. G. Rodrigo, L. Martin-Moreno and S. I. Bozhevolnyi, "Channel plasmon-polaritons: modal shape, dispersion, and losses," Opitcs Letter., vol. 31, p. 3447, 2006.

[63] J. R. Krenn, M. Salerno, N. Felidj, B. Lamprecht, G. Schider, A. Leitner, F. R. Aussenegg, J. C. Weeber, A. Dereux and J. P. Goudonnet , "Light field propagation by metal micro- and nanostructures," J. Microsc vol. 202, p. 122, 2001.

[64] J. C. Weeber, Y. Lacroute and A. Dereux, "Optical near-field distributions of surface plasmon waveguide modes," Phys. Rev. B, vol. 68, p. 115401, 2003.

[65] P. Berini, "Plasmon-polariton waves guided by thin lossy metal films of finite width: Bound modes of symmetric structures," Phys. Rev. B, vol. 61, p. 10484, 2000.

[66] T. Yatsui, M Kourogi and M. Ohtsu, "Plasmon Waveguide for Optical Far/Near-Field Conversion," Appl. Phys. Lett., vol. 79, p. 4583, 2001.

[67] J. C. Weeber, J. R. Krenn, A. Dereux, B. Lamprecht, Y. Lacroute and J. P. Goudonet, "Near-field observation of surface plasmon polariton propagation on thin metal stripes," Phys. Rev. B, vol. 64, p. 045411, 2001.

[68] T. Nikolajsen, K. Leosson, I. Salakhutdinov and S. I. Bozhevolnyi, "Polymer-based surface-plasmon-polariton stripe waveguides at telecommunication wavelengths," Appl. Phys. Lett., vol. 82, p. 668, 2003.

[69] H. Raether, *Surface Plasmons on Smooth and Rough Surfaces and on Gratings*, Berlin, Germany: Springer-Verlag, 1988.

[70] V. M. Agranovich and D. L. Mills, *Surface Polaritions*, Amsterdam, Netherland: Elsevier Science, 1982.

[71] A. D. Boardman, *Electromagnetic surface modes*, New York, NY: J. Wiley, 1982.

[72] N. Engheta and R. W. Ziolkowski, *Electromagnetic Metamaterials: Physics and Engineering Explorations*, New York, NY: J. Wiley, 2006.

[73] A. V. Zayats, I. I. Smolyanivov and A. A. Maradudin, “Nano-Optics of Surface Plasmon Polaritons,” Phys. Rep., vol. 408, p. 131, 2005.

[74] B. Prade, J. Y. Vinet and A. Mysyrowicz, “Guided optical waves in planar heterostructures with negative dielectric constant,” Phys. Rev. B, vol. 44, p. 13556, 1991.

[75] L. Solymar and E. Shamonina, *Waves in metamaterials*, New York, NY: Oxford University Press, 2009.